LEABHARLANN CHOLÁISTE NA TRÍONÓIDE, BAILE ÁTHA CLIATH | TRINITY COLLEGE LIBRARY DUBLIN
Ollscoil Átha Cliath | The University of Dublin

Terms and Conditions of Use of Digitised Theses from Trinity College Library Dublin

Copyright statement

All material supplied by Trinity College Library is protected by copyright (under the Copyright and Related Rights Act, 2000 as amended) and other relevant Intellectual Property Rights. By accessing and using a Digitised Thesis from Trinity College Library you acknowledge that all Intellectual Property Rights in any Works supplied are the sole and exclusive property of the copyright and/or other IPR holder. Specific copyright holders may not be explicitly identified. Use of materials from other sources within a thesis should not be construed as a claim over them.

A non-exclusive, non-transferable licence is hereby granted to those using or reproducing, in whole or in part, the material for valid purposes, providing the copyright owners are acknowledged using the normal conventions. Where specific permission to use material is required, this is identified and such permission must be sought from the copyright holder or agency cited.

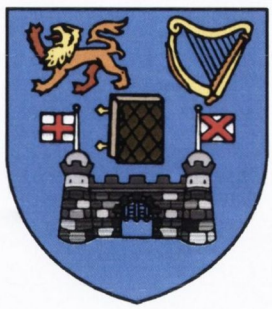
Liability statement

By using a Digitised Thesis, I accept that Trinity College Dublin bears no legal responsibility for the accuracy, legality or comprehensiveness of materials contained within the thesis, and that Trinity College Dublin accepts no liability for indirect, consequential, or incidental, damages or losses arising from use of the thesis for whatever reason. Information located in a thesis may be subject to specific use constraints, details of which may not be explicitly described. It is the responsibility of potential and actual users to be aware of such constraints and to abide by them. By making use of material from a digitised thesis, you accept these copyright and disclaimer provisions. Where it is brought to the attention of Trinity College Library that there may be a breach of copyright or other restraint, it is the policy to withdraw or take down access to a thesis while the issue is being resolved.

Access Agreement

By using a Digitised Thesis from Trinity College Library you are bound by the following Terms & Conditions. Please read them carefully.

I have read and I understand the following statement: All material supplied via a Digitised Thesis from Trinity College Library is protected by copyright and other intellectual property rights, and duplication or sale of all or part of any of a thesis is not permitted, except that material may be duplicated by you for your research use or for educational purposes in electronic or print form providing the copyright owners are acknowledged using the normal conventions. You must obtain permission for any other use. Electronic or print copies may not be offered, whether for sale or otherwise to anyone. This copy has been supplied on the understanding that it is copyright material and that no quotation from the thesis may be published without proper acknowledgement.



Understanding DNA Dispersed Single-Walled Carbon Nanotube Systems

by

Helen M. Cathcart

A thesis submitted for the degree of
Doctor of Philosophy
in the
University of Dublin

School of Physics
Trinity College Dublin

2008

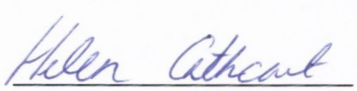
TRINITY COLLEGE
2 7 MAY 2008
LIBRARY DUBLIN
THESIS
8406

Declaration

I declare that the work in this thesis has not been previously submitted as an exercise for a degree to this or any other university.

The work described herein is entirely my own, except for the assistance mentioned in the acknowledgements and the collaborative work mentioned in the list of publications.

I agree that Trinity College Library may lend or copy this thesis on request.



Helen M. Cathcart

October 2007

For my parents: George and Mary

Acknowledgements

The past four years have been an informative and enjoyable time, during which I have learned plenty of physics and so much more. For these experiences, I am indebted to many people. Firstly, I wish to thank **Prof. Werner Blau** for giving me the opportunity to work in Group BU and to attend various trips, courses and summer schools over the last few years. It has been a wonderful experience. Special thanks must go to **Prof. Jonathan Coleman** for all his help and supervision. I am extremely grateful to you for your support and expertise over the years, without which this thesis would not have been possible.

I would like to thank **Dr. Susan Quinn** for her continued help, particularly in the early days, and for sharing her knowledge of DNA. Equal thanks must go to **Prof. John Kelly** for allowing me to work in his lab and for all the useful advice and discussions. Thanks must also go to **Dr. Valeria Nicolosi** for her friendship and expertise, particularly in the areas of TEM and AFM. In addition, I would like to thank **Dr. Sara Callagy, Johnny Amiran** and **Marguerite Hughes** for their contribution to this work.

Special thanks go to **David Blond, Karen Young, Evelyn Doherty** and **Martin Djiango** for sharing 'my' office and making the last few months far more entertaining than initially anticipated. A big thank-you must also go to **Fiona Blighe** and **Shane Bergin** who started with me and supported me the whole way through this thesis. Your friendship has helped me through the tougher moments and made the good times even better. I will leave with many happy memories of the times we spent together.

A huge thank-you goes to all other group members, both past and present, for making this such a great place to work. In no particular order, thanks goes to **Anna, Chris, Yenny, Trevor, David R, Ian, Ronan, Umar, Paula, Denise, Mustafa, Take, Javier, Zhenyu, Sukanta, Darren, Niall, Phil and Marguerite. Also thanks to Denis, Grace, Kev, Rory, Emer, Rob, Adam, Margaret & Patrick, Gordon, Keith,**

Schweta, Eimhin, Eleni, Evan, Nacho, Sandy, Cathal, Stephen, Colin, James, Rebekah, Les and **Sharon.**

I want to dedicate a huge thank-you to my family — **George, Mary, Richie**, and now, **Kate** — whose endless love, patience, encouragement and support has helped me become the person I am today. I couldn't have done it without you. And finally, to **Garry,** who has supported me through good times and bad over the past 3 years and always made me smile again when things got tough, thank you.

Abstract

HiPCO Single-walled carbon nanotubes (SWNTs) have been dispersed in water using a variety of different nucleic acids. An extensive study of the factors controlling the quality of the DNA-SWNT dispersions was carried out, allowing one to optimise the sample preparation technique. Numerous different factors, such as improving the sonication process; comparing different DNA types; comparing different DNA:SWNT ratios and the use of centrifugation to remove aggregates and insoluble material were investigated. It was found that the best dispersions were achieved when the samples were sonicated for 2hrs in a small round-bottom flask, suspended centrally in an ice-water sonic bath. It was found that a ratio of 2:1 (DNA:SWNT) gave the most reproducible samples. In addition, it was found that the samples were improved by centrifuging at 3,300g for 1 hr after sonication to remove any large aggregates that were not broken up during sonication.

Once the sample preparation technique had been optimised, a full concentration study was carried out using natural salmon testes DNA as the dispersant. It was found that the primary factor controlling the nanotube bundle size distribution in the dispersion is the nanotube concentration. AFM measurements showed that the mean bundle diameter tends to decrease with decreasing concentration, while the number fraction of individual nanotubes increases with decreasing concentration. At low nanotube concentrations, number fractions of up to 0.83 individual SWNTs, equating to a mass fraction of 6.2% have been obtained. Both the absolute number density and mass per volume of individual nanotubes initially increased with decreasing concentration, displaying a peak at 0.027 mg/mL. This concentration therefore yields the largest quantities of individually dispersed SWNTs. The AFM data for populations of individual nanotubes was confirmed by infrared photoluminescence spectroscopy. The photoluminescence (PL) intensity increased with decreasing concentration, indicating extensive debundling. The concentration dependence of the luminescence intensity matched well to the AFM data on the number density of individual nanotubes. More importantly, it was found that once initially dispersed, spontaneous

debundling occurs upon dilution without the need for sonication. This implies that DNA-SWNT hybrids exist in water as a solution rather than a dispersion. The effects of dilution have been compared to the results obtained by ultracentrifuging the samples, showing dilution methods to be a viable and cost-effective alternative to ultracentrifugation. It was found that even after 4 hrs of ultracentrifugation at 122,000*g*, bundles with diameters of up to 4 nm remained in solution. The bundle diameter distribution after ultracentrifugation was very similar to the equilibrium distribution for the appropriate concentration after dilution, showing ultracentrifugation to be equivalent to dilution.

Further studies on the time dependent evolution of DNA wrapping of SWNTs were undertaken, allowing one to develop a deeper understanding of the nature of the interaction between DNA and SWNTs. SWNTs were dispersed with salmon testes DNA in water and monitored over a three month period. The DNA-SWNT complex was monitored with high resolution transmission electron microscopy (HRTEM), showing the progressive formation of a DNA coating on the walls of the nanotube. It was found that a full monolayer coating of DNA took approximately 35 days to form when the samples were stored at room temperature. Improvements in the NIR PL and absorption spectra were correlated with the completion of a full layer of DNA on the walls of the nanotube. The magnitude of circular dichroism spectrum was found to decrease continuously over the duration of the experiment and was linked to a progressive reduction in the quantity of free DNA in solution. Close up HRTEM images of the DNA-SWNT complex showed helical wrapping of the DNA around the SWNTs. These images suggest that the binding mechanism is one in which the DNA unzips onto the nanotube, allowing the two separate strands to interact with the nanotube. The strands were observed to phase shift by 180° with respect to each other, thus maximising both the nanotube coverage and the distance between the negatively-charged phosphate groups on the backbone of each strand. The temperature dependence of the DNA wrapping process was investigated. The rate of DNA wrapping was plotted with respect to sample temperature on an Arrhenius plot, allowing one to calculate the activation energy for DNA wrapping. It was found that the time taken for the monolayer to form is controlled by a rate limiting process with

an activation energy of 0.43 eV. The value is in keeping with the suggested wrapping mechanism. It is suggested that the underlying mechanism for the improvement in the PL and absorption spectra upon the completion of DNA wrapping is based on the removal of surface oxides from the nanotube sidewalls.

Finally, SWNTs were dispersed in water using short oligonucleotides and medium length, single-stranded RNA. It was found that pyrimidine bases are more efficient at the dispersion of SWNTs than purine bases. The nanotube bundle sizes were investigated with respect to nanotube concentration for all dispersants. In all cases the nanotube bundle sizes were found to decrease with decreasing concentration. AFM measurements showed that for the dilution series prepared with poly(rA) and dG_{15}, the bundle diameters decreased almost linearly with concentration, before stabilising at mean diameters of 1.5 nm and 2.3 nm respectively. The number fractions were calculated to be 0.63 and 0.76 at low concentrations for the poly(rA) and the dG_{15} dilution series respectively.

All samples were analysed with NIR-PL and absorption spectroscopy. It was found that both the extinction coefficient and the quantum efficiency of the system increased as the nanotube concentration decreased, indicating extensive debundling in all dilution series.

Table of Contents

Declaration 1

Abstract 5

Table of Contents 8

Introduction 10

1.1 Background and Motivation 10

1.2 Thesis outline 12

1.3 References 13

Introduction and Literature Review 15

2-1 Carbon Nanotubes — Introduction 15

2-1-1 Electronic Properties 18

2-1-2 Optical Properties 23

2-1-3 SWNT Synthesis — Carbon Vapour Deposition 26

2-2 DNA — Introduction 27

2-2-1 Physical Structure of DNA 27

2-2-2 Optical Properties of DNA 31

2-3 Literature Survey 32

Materials and Methods 41

3-1 Materials 41

3-2 Methods of Analysis 42

3-2-1 Absorption Spectroscopy 42

3-2-2 Circular Dichroism Spectroscopy 43

3-2-3 Photoluminescence Spectroscopy 45

3-2-4 Atomic Force Microscopy 47

3-2-5 Transmission Electron Microscopy 50

3-3 References 52

Optimising Sample Preparation 53

4-1 Introduction 53

4-2 Results 53

4-2-1 Sonication — Temperature, Vessel Shape & Position 53

4-2-2 High Powered Sonic Tip 55

4-2-3 Sonication Time 58

4-2-4 Ratio of DNA to SWNTs 59

4-2-5 Different Types of DNA 62

4-2-6 Reproducibility 65

4-2-7 Optical Microscopy and Light Centrifugation 67

4-4 References 70

Full Concentration Study 71
5-1 Introduction 71
5-1-1 Effects of Sonication on the Nanotube Bundles *72*
5-1-2 Beneficial Results of the Concentration Study *72*
5-2 Experimental Procedure 73
5-3 Results 75
5-3-1 Dispersion Stability *75*
5-3-2 The effect of concentration on the bundle diameter distribution *77*
5-3-3 Dispersion or Solution? *80*
5-3-4 Number density and absolute number of individual SWNTs *81*
5-3-5 Mass Fraction & Partial Concentration of Individual Nanotubes *84*
5-3-6 IR Photoluminescence *86*
5-3-7 Comparing Dilution to Ultra-Centrifugation *89*
5-4 References 96
The Evolution of DNA wrapping of Nanotubes 98
6-1 Introduction 98
6-2 Results 99
6-2-1 Absorption and Photoluminescence Spectroscopy *99*
6-2-2 Atomic Force Microscopy *104*
6-2-3 Circular Dichroism Spectroscopy *106*
6-2-4 High Resolution Transmission Electron Microscopy *111*
6-2-5 Temperature Studies *117*
6-2-6 Role of O_2 and pH in PL quenching *121*
6-3 Conclusion 126
6-4 References 127
The dispersion efficiency of oligonucleotides 129
7-1 Introduction 129
7-2 Experimental Procedure 130
7-3 Results 130
7-2-1 AFM *131*
7-2-2 Absorption and NIR-PL Spectroscopy *136*
7-2-3 Time dependent changes in the photoluminescence *146*
7-3 Conclusion 147
7-4 References 148
Conclusions and Further Work 149
8-1 Conclusions 149
8-2 Future Work 152
8-3 References 155
Appendix: Publication List 156

Chapter 1

Introduction

1.1 Background and Motivation

In the contemporary era, much scientific research is motivated by the world's demands for smaller, lighter, stronger and cheaper materials. These novel materials are increasingly used as substitutes for naturally occurring materials such as wood, stone, metals and natural fibres. Over the past decade, the development of polymers has revolutionised the manufacturing industry. Polymers are straightforward and inexpensive to fabricate, with low weights and high strengths. They are routinely incorporated into a vast array of different items, ranging from commonplace items such packaging, clothing and general household items, to highly complex devices such as computers, aeroplanes and automobiles. In fact, in the developed world, plastics are now used so extensively, that they permeate every facet of human life. However, in today's every-changing world, the consumers' constant requirement for the latest gadget and the new and improved model drives demand for new and improved materials.

Industry has benefited considerably from the development of high-strength polymer composites. In these composites, fillers, such as glass fibre[1], carbon black[2], graphene[3] and boron fibre[4], are added to reinforce the polymer, producing a set of extremely high strength, low weight materials. Clearly, these innovative materials are of huge benefit to a variety of different industries, such as the aeronautical industry which strives to build stronger, lighter aircraft and the sporting industries, where improved equipment gives athletes a performance edge when it matters most.

In 1991, an exciting new material, the carbon nanotube, was discovered by Sumio Iijima in Japan[5, 6]. Carbon nanotubes are an exceptional material with many attractive qualities. They are extremely light with a density of ~1500 $kg.m^{-3}$ [7]. In

addition, they have an extremely high strength to weight ratio and high aspect ratios, with diameters on the order of nanometres and lengths on the order of microns. These properties make nanotubes excellent fillers[8-11]. Nanotubes have excellent heat conducting properties, with reported thermal conductivities of 6600W/m.K at room temperature[12]. They are extremely stiff and exceptionally strong, with strengths of ~37 GPa and a Young's modulus of up to 0.64 TPa[13]. Nanotubes can be either metallic or semiconducting depending on their chiral vector. In metallic nanotubes, electronic transport occurs ballistically along the length of the nanotube, enabling them to carry extremely high currents with effectively no heating[13].

Based on the above mentioned properties, many different applications for nanotubes have been explored. Examples include, tiny transistors fabricated from semiconducting nanotubes[14]; nanotube-filled conductive polymers for electrostatic spray painting[15] and for discharging the static build-up on fuel lines[16]; efficient electrodes in lithium-ion batteries[17]; chemical sensors[18] and petroleum filters[19]. However, despite the plethora of other exciting applications, nanotubes have so-far failed to reach their full potential, owing to a lack of available solvents, plus their tendency to aggregate and form large bundles once in solution. Bundles reduce the nanotubes' effectiveness as mechanical reinforcement fillers[20] and make it impossible to utilise the unique electronic structure of individual nanotubes. Thus, if nanotubes are to fulfil current expectations, it is essential to develop the technology both to efficiently disperse nanotubes in solution, and to be separate them on the basis of electronic properties.

Deoxyribonucleic acid (DNA) is an organic polymer, which has been shown to be effective at dispersing nanotubes in aqueous solutions[21, 22]. In addition, it has been demonstrated that DNA-nanotube solutions can be separated into fractions with different electronic structure using ion-exchange chromatography[22-24]. Thus, DNA-nanotubes dispersions show exceptional promise as a method of processing nanotubes. Presently, many questions remain regarding the nature of the interaction between DNA and nanotubes and the factors controlling the dispersion efficiency of DNA. Gaining a comprehensive understanding these issues is essential if the dispersion properties of DNA are to be fully utilised. Thus, the aim of this thesis is to further the understanding of the nature of DNA-nanotube dispersions.

1.2 Thesis outline

The thesis is outlined as follow:

Chapter Two introduces the main materials studied throughout this thesis, with a detailed description of the physical, electronic and optical properties of single-walled carbon nanotubes and an overview of the properties of DNA. In addition, a summary of the relevant literature is presented here.

Chapter Three identifies the specific materials used throughout this work and describes the various measurement techniques employed to characterise the DNA-nanotube dispersions.

Chapter Four focuses on optimising the sample preparation techniques. A systematic study of all the factors controlling the quality of the DNA-nanotube dispersions was carried out in order to find the best procedure for sample preparation.

In Chapter Five, the relationship between nanotube bundle size and nanotube concentration is investigated for samples prepared with natural salmon testes DNA. Both the mean bundle diameters and the partial concentrations of individual nanotubes are investigated for a range of concentrations. In addition the effect of sonication on the bundle diameter distribution is explored.

In Chapter Six, the time-dependent evolution of DNA wrapping of nanotubes is explored. Changes in the optical properties of the nanotube are observed which will be shown to be correlated to progressive changes in the interaction between the DNA and nanotube. The kinetics controlling the DNA wrapping are investigated further with respect to the sample temperature and pH. In addition, a mechanism for PL quenching in these systems is considered.

In Chapter Seven, the dispersion efficiency of oligonucleotides and a medium length ribonucleic acid (RNA) homopolymer is considered. The relationship between bundle size and nanotube concentration is investigated for five different DNA types.

Finally, Chapter Eight concludes with a review of the main results and a discussion of future work.

1.3 References

1. Barre, S., Chotard, T. & Benzeggagh, M. L. Comparative study of strain rate effects on mechanical properties of glass fibre-reinforced thermoset matrix composite. Composites Part A: Applied Science and Manufacturing 27, 1169-1181 (1996).
2. Grunlan, J. C., Gerberich, W. W. & Francis, L. F. Electrical and mechanical behavior of carbon black-filled poly(vinyl acetate) latex-based composites. Polymer Engineering and Science 41, 1947-62 (2001).
3. Stankovich, S. et al. Graphene-based composite materials. Nature 442, 282-286 (2006).
4. Brack, N., Rider, A. N., Halstead, B. & Pigram, P. J. Surface modification of boron fibres for improved strength in composite materials. Journal of Adhesion Science and Technology 19, 857-77 (2005).
5. Iijima, S. Helical microtubules of graphitic carbon Nature 354, 56 (1991).
6. Iijima, S. & Ichihashi, T. Single-shell carbon nanotubes of 1-nm diameter Nature 363, 603-15 (1993).
7. Coleman, J. N. et al. Improving the mechanical properties of single-walled carbon nanotube sheets by intercalation of polymeric adhesives. Applied Physics Letters 82, 1682-4 (2003).
8. Coleman, J. N. et al. High-performance nanotube-reinforced plastics: Understanding the mechanism of strength increase. Advanced Functional Materials 14, 791-798 (2004).
9. Ryan, K. P. et al. Carbon nanotube nucleated polymer crystallization. Fullerenes Nanotubes and Carbon Nanostructures 13, 431-434 (2005).
10. Coleman, J. N. et al. Reinforcement of polymers with carbon nanotubes. The role of an ordered polymer interfacial region. Experiment and modeling. Polymer 47, 8556-8561 (2006).
11. Dufresne, A. et al. Processing and characterization of carbon nanotube/poly(styrene-co-butyl acrylate) nanocomposites. Journal of Materials Science 37, 3915-23 (2002).
12. Berber, S., Young-Kyun, K. & Tomanek, D. Unusually high thermal conductivity of carbon nanotubes. Physical Review Letters 84, 4613-16 (2000).
13. Baughman, R. H., Zakhidov, A. A. & De Heer, W. A. Carbon nanotubes - The route toward applications. Science 297, 787-792 (2002).
14. Keren, K., Berman, R. S., Buchstab, E., Sivan, U. & Braun, E. DNA-templated carbon nanotube field-effect transistor Science 302, 1380-2 (2003).
15. Baughman, R. H., Zakhidov, A. A. & De Heer, W. A. Carbon nanotubes - The route toward applications Science 297, 787-792 (2002).
16. Mapleston, P. Carbon nanotubes: Today's future technology? Plastics Engineering 63, 20-24 (2007).
17. Ng, S. H. et al. Single wall carbon nanotube paper as anode for lithium-ion battery. Electrochimica Acta 51, 23-28 (2005).
18. Staii, C., Johnson, A. T., Chen, M. & Gelperin, A. DNA-Decorated Carbon Nanotubes for Chemical Sensing. Nano Lett. 5, 1774-1778 (2005).
19. Srivastava, A., Srivastava, O. N., Talapatra, S., Vajtai, R. & Ajayan, P. M. Carbon nanotube filters. Nature Materials 3, 610-14 (2004).

20. Cadek, M. et al. Reinforcement of polymers with carbon nanotubes: the role of nanotube surface area. Nano Letters 4, 353-6 (2004).
21. Nakashima, N., Okuzono, S., Murakami, H., Nakai, T. & Yoshikawa, K. DNA Dissolves Single-walled Carbon Nanotubes in Water Chemistry Letters 32, 456 - 457 (2003).
22. Zheng, M. et al. DNA-assisted dispersion and separation of carbon nanotubes Nature Materials 2, 338-342 (2003).
23. Strano, M. S. et al. Understanding the nature of the DNA-assisted separation of single-walled carbon nanotubes using fluorescence and Raman spectroscopy Nano Letters 4, 543-50 (2004).
24. Zheng, M. et al. Structure-based carbon nanotube sorting by sequence-dependent DNA assembly Science 302, 1545-8 (2003).

Chapter 2

Introduction and Literature Review

2-1 Carbon Nanotubes — Introduction

Graphite and diamond are two well-known allotropes of the extremely versatile element carbon. Although both are made from the same element, they have very different structures and, consequently, different properties[1].

Graphite consists of planar sheets of sp^2-hybridised carbon atoms (Figure 2-1 (A)) arranged in a hexagonal lattice. Electrons are free to move between different carbon atoms through delocalised π-bonds from the unhybridised p_z orbital on each atom. Consequently, graphite is electrically conductive within the planes (and to a lesser extent perpendicular to the planes). Weak bonding exists between the different sheets of graphene (a single graphite plane), allowing them to slide easily over each other when impurities are present. This allows graphite to be used as a lubricant in industry[2].

Diamond consists of sp^3-hybridised carbon atoms (Figure 2-1 (B)), each carbon being bonded via σ-bonds to four other atoms in a three-dimensional network. Diamond is an excellent conductor of heat, electrically insulating and the hardest substance known to man[2].

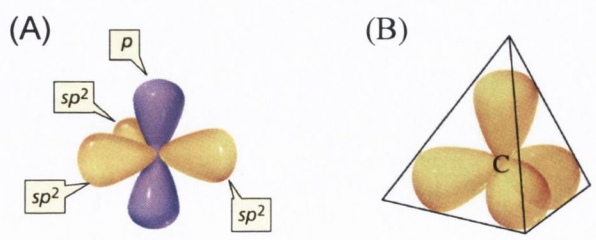


Figure 2-1 (A) SP^2 hybridized carbon (B) SP^3 hybridized carbon.

A new allotrope of carbon, the multi-walled nanotube (MWNT), was discovered in 1991 by Sumio Iijima in the NEC laboratory in Tsukuba, Japan[3]. About two years later, he observed the single-walled carbon nanotube (SWNT)[4]. A SWNT can be thought of as a graphene sheet rolled into a seamless cylinder[5]. SWNTs have diameters in the order of 0.7–2 nm, depending on the method of synthesis, and can be up to microns in length, giving them very high aspect ratios. Depending on the way the graphene sheet is "rolled up", the nanotube can have different helicity and consequently different characteristics.

A MWNT has an outer diameter of approximately 2–25 nm. It consists of a number of nanotubes with various degrees of helicity, arranged in coaxial cylinders with an interlayer spacing of ~3.4 Å[6], which is very close to the basal plane spacing in graphite. The varying helicity between the different shells is necessary to obtain the best fit between the successive tubes, thus minimising the interlayer spacing.

All single-walled nanotube can be characterised using a chiral vector[7]:

$$\mathbf{C_h} = n\hat{a}_1 + m\hat{a}_2 \equiv (n,m)$$

where n and m are integers and $\hat{a}_1$ and $\hat{a}_2$ are the unit vectors in a sheet of graphene as shown in Figure 2-2 (A).

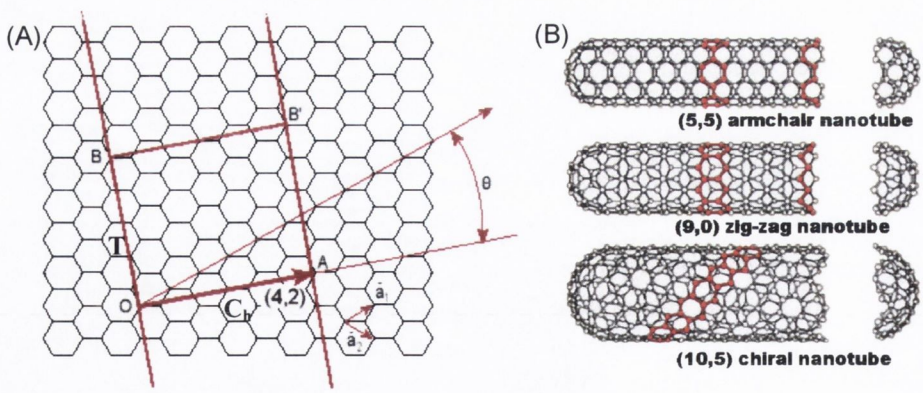


Figure 2-2[7,8] (A) The Chiral Vector ($\mathbf{C_h}$) and the perpendicular translational vector (**T**) for a SWNT (B) The three types of SWNTs

The chiral angle (θ) describes the angle between $\mathbf{C_h}$ and $\hat{a}_1$. When the nanotube is rolled up to form a cylinder, one end (O) of the chiral vector meets the other end (A) to form the circumference of the nanotube. The tube axis is perpendicular to this vector. Each nanotube will have different electronic properties depending on its chirality and diameter.

Generally nanotubes can be split into three main classes (Figure 2-2 (B)); armchair nanotubes have a chiral vector of (n,n) and a chiral angle of 30°; zigzag nanotubes have a chiral vector of (n,0) or (0,m) and a chiral angle of 0°; and chiral nanotubes have general (n,m) values and a chiral angle of between 0° and 30° [4,9]. The nanotube diameter (d_t) can be calculated from the chiral vector as[10]

$$d_t = C_h/\pi = (\sqrt{3}\, a_{cc}/\pi)\,(m^2 + mn + n^2)^{1/2}$$

where a_{cc} is the nearest neighbour C-C distance (1.421Å in graphene) and C_h is the length of the chiral vector $\mathbf{C_h}$.

The chiral vector $\mathbf{C_h}$ and the translational vector $\mathbf{T}$ are used to define the unit cell of the nanotube (Figure 2-2 (A)). $\mathbf{T}$ is defined as the vector that runs perpendicular to the chiral vector, connecting points O and B of the graphene lattice where B is the first lattice point that the vector passes through. The unit cell of the nanotube is the rectangle OABB'. The number of hexagons per nanotube unit cell (N) can be calculated by dividing the area of the nanotube unit cell by the area of a hexagon

$$N = \frac{|\mathbf{C_h} \times \mathbf{T}|}{|\hat{a}_1 \times \hat{a}_2|}$$

Each hexagon contains two carbon atoms and hence there are 2N carbon atoms in the nanotube unit cell.

2-1-1 Electronic Properties

The electronic properties of a nanotube depend on its diameter and helicity. Armchair nanotubes are always metallic. Chiral and zigzag nanotubes are either semi-metallic, or semiconducting with a diameter dependent bandgap. To understand these differences, a basic understanding of the electronic structure of graphene is needed.

Figures 2-3 (A) & (B) show the unit cell and the brillouin zone (shaded hexagon) in reciprocal space of graphene respectively. The reciprocal lattice vectors of graphene, ($\mathbf{b_1}$ & $\mathbf{b_2}$) are related to the real space unit vector ($\hat{a}_1$ & $\hat{a}_2$) according to the equation:

$$\hat{a}_i.\mathbf{b_j} = 2\pi\delta_{ij}; \qquad \delta_{ij} = \begin{cases} 1, & i = j \\ 0, & i \neq j \end{cases}$$

The three high symmetry points of the Brillouin zone Γ, K and M are shown, situated at the centre, the corner and the centre of the edge of the hexagon respectively.

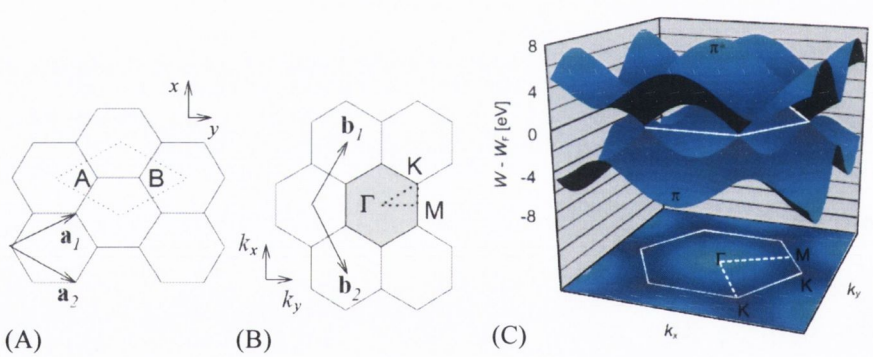


Figure 2-3[10,11] (A) The unit cell (dotted rhombus) of graphene containing two carbon atoms at points A and B. (B) The brillouin zone (shaded hexagon) for graphene showing the high symmetry points (Γ, K, M) and the reciprocal lattice vectors of 2D graphene ($\mathbf{b_1}$ and $\mathbf{b_2}$). (C) 2D energy dispersion relations of graphene. The π and the π* bands are degenerate at the corners of the 2D hexagonal Brillouin zone, known as the K-points

In graphene, the unhybridised p_z orbitals on adjacent carbon atoms overlap to form a bonding π band and an anti-bonding π* band. These bands are close to the Fermi energy, allowing electrons to be excited optically from the π band into the π*

band[10]. In 1947, P.R. Wallace et. al. derived an equation that describes the 2D energy dispersion relations of these bands in terms of the wave vectors k_x and k_y[12]. Using this equation it can be shown that the π and π^* energy bands are equal at the K-points as shown in Figure 2-3 (C). Because of this, graphene is considered a zero-gap semiconductor. (In graphite, interactions between the graphene planes cause the energy bands to overlap by approximately 40 meV, making it metallic).

Carbon nanotubes differ from graphene in one main respect. Whereas a sheet of graphene is considered to be infinite in two dimensions, carbon nanotubes have lengths on the micrometer scale and diameters on the nanometre scale. Consequently, there will be a large number of allowed states in the axial direction, but very few in the circumferential direction.

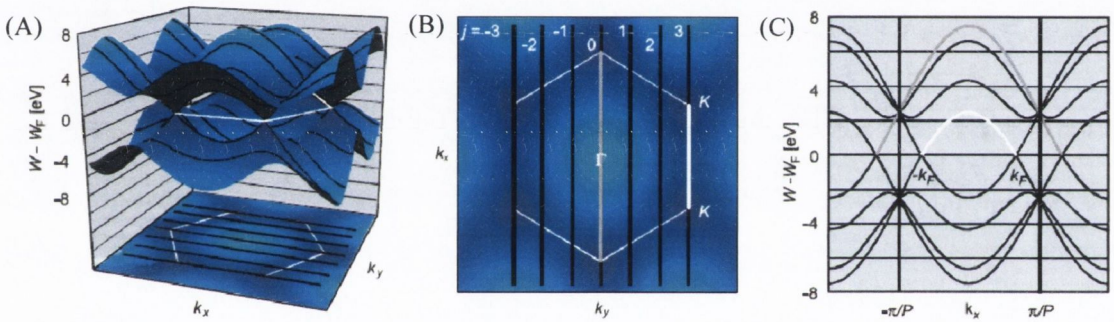


Figure 2-4[11] (A) The dispersion relation of graphene overlaid with the cutting lines for a (3,3) nanotube. (B) The allowed *k*-states for a (3,3) nanotube projected onto the brillouin zone for graphene with (C) the associated electronic energy band structure.

Figure 2-4 (A) & (B) show the allowed states for a (3,3) armchair carbon nanotube superimposed on the first brillouin zone for carbon. In armchair nanotubes, the tube axis lies along the x-axis of the Brillouin Zone, as shown above. The macroscopic length of the nanotube therefore gives a quasi-continuous set of allowed k_x values along the tube axis. In the radial direction electrons are confined by the monolayer thickness of the graphene sheet, leading to the quantum confinement of electrons normal to the tube axis. Only certain wave vectors which give rise to standing waves can exist in the circumferential direction of the tube. This leads to

periodic boundary conditions in the circumferential direction, and a discrete set of k_y values.

The periodic boundary conditions are known as Born-Von Karman conditions and are defined as

$$\mathbf{k} \cdot \mathbf{C_h} = 2\pi j$$

where j is an integer such that $\{(1\text{-}N/2) \leq j \leq N/2\}$ giving rise to N discrete circumferential **k** vectors[13].

Consequently, the allowed states in the nanotube condense into a set of straight 'cutting lines' in the axial direction of the tube as shown in Figures 2-4 (A) & (B). In armchair nanotubes the allowed wave vectors always include the K-point, and thus the bonding and the antibonding π energy bands overlap, making the nanotubes metallic.

Once the set of allowed circumferential **k** values has been calculated for a given nanotube, they can be inserted into the energy dispersion relations for graphene, allowing one to calculate the 1D electronic band structure of the nanotube[14]. Since there are 2N carbon atoms in the nanotube unit cell, there are N pairs of bonding π and anti-bonding π* energy bands. The metallic nature of the (3,3) armchair nanotube mentioned previously can be clearly seen by the lack of bandgap in the band structure diagram (Figure 2-4 (C)).

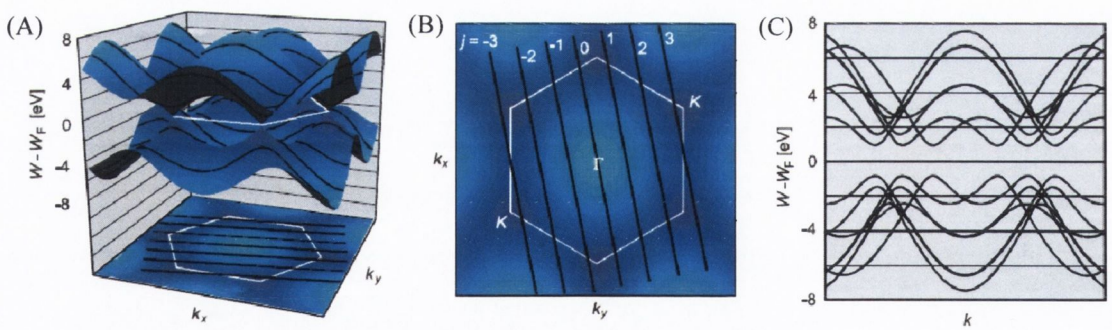


Figure 2-5[11] (A) The dispersion relation of graphene overlaid with the cutting lines for a (4,2) nanotube. (B) The allowed *k*-states for a (4,2) nanotube projected onto the brillouin zone for graphene with, (C), its associated electronic energy band structure.

Figure 2-5 shows the allowed k-states and the dispersion relations for a chiral (4,2) carbon nanotube. This nanotube has a diameter which is very similar to that of the (3,3) nanotube, but has very different electronic properties. In chiral nanotubes, the nanotube axis is not parallel to the x-axis of the graphene brillouin zone and the lines showing the allowed wave vectors lie at an angle to k_x. Because of this, the set of allowed states does not always include the K-point. When this is the case, there will be a bandgap between the valence and conduction bands and the nanotube will be semiconducting. This is the case for the (4,2) nanotube.

However, in certain chiral tubes, the cutting lines pass through the K-point showing it to be an allowed state and the nanotube will be semi-metallic. To calculate the set of nanotubes with an allowed state at the K-point, we insert **K** (the vector connecting Γ and K) into the periodic boundary conditions.

It is known that

$$\mathbf{K} = (\mathbf{b}_1 - \mathbf{b}_2)/3 \quad \text{and} \quad \mathbf{C}_h = n\hat{a}_1 + m\hat{a}_2$$

Thus,
$$\mathbf{K} \cdot \mathbf{C}_h = (\mathbf{b}_1 - \mathbf{b}_2)/3 \cdot (n\hat{a}_1 + m\hat{a}_2)$$
$$= [(n/3)\,\mathbf{b}_1 \cdot \hat{a}_1] - [(m/3)\,\mathbf{b}_2 \cdot \hat{a}_2]$$
$$= 2\pi/3\,(n-m)$$

But $\mathbf{K} \cdot \mathbf{C}_h = 2\pi j$ Born-Von Karman boundary conditions

$\therefore$ $n - m = 3j$ where j is an integer,

Thus, a third of all possible nanotubes are either metallic or semi-metallic, while the rest will be semiconducting as shown in Figure 2-6.

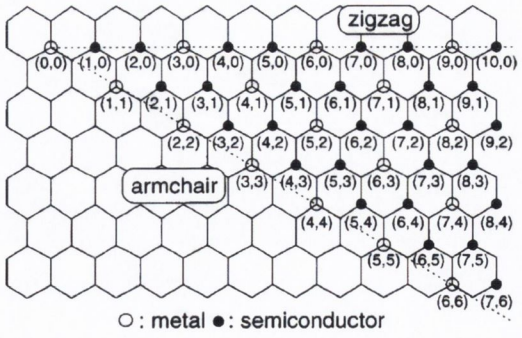


Figure 2-6[8] The (n,m) chiral indices for nanotubes are shown. Metallic nanotubes are shown as open circles, while semi-conducting nanotubes are shown as closed circles.

The size of the bandgap in a semiconducting nanotube is dependent on the nanotube diameter. As the diameter increases, the number of carbon atoms in the nanotube unit cell (2N) increases. This in turn increases the number of allowed wave vectors in the circumferential direction, leading to a smaller bandgap[11]. The bandgap energy (E_{gap}) is dependent solely on the nanotube diameter and can be calculated using the equation[15]:

$$E_{gap} = 2\,\gamma_0\,a_{cc} / d_t$$

where γ_0 is the C-C tight binding overlap energy (2.7 eV), a_{cc} is the next nearest neighbour carbon-carbon distance and d_t is the nanotube diameter.

The above calculations are accurate for larger nanotubes, however in very narrow nanotubes, the large curvature changes the carbon-carbon bond distances in the graphene sheet and introduces a mixing of the σ and π orbitals. For this reason, the calculations for the (3,3) and the (4,2) nanotubes mentioned above are given for illustrative purposes only. In reality, calculating the electronic structure for these small nanotubes is less straightforward[16]. However, this is beyond the scope of this thesis.

The density of electronic states (DOS) of a nanotube can be calculated from the electronic dispersion relations according to the equation[17]

$$g(E)dE = 2\,g(k)\,dk$$

$$\rightarrow \qquad g(E) = \frac{2g(k)}{dE/dk}$$

where *g(E)* is the density of electronic states per unit energy range, *g(k)* is the density of states in reciprocal space and *dE/dk* is the slope of the *E-k* dispersion curve in the electronic band diagram. The factor of two is due to the fact that there are two electron spin states for every allowed *k*-state. All bands in the *E-k* dispersion diagrams have a slope of zero at $k = 0$, resulting in strong van Hove singularities in the DOS at energies corresponding to each band minimum[18]. Figure 2-7 (A) shows the DOS for both a metallic SWNT and a semiconducting SWNT. The van Hove singularities are present in both nanotubes. However, the DOS for two nanotube types differ at the Fermi energy level. In a metallic nanotube there is a finite density of states at the

Fermi energy whereas in a semiconducting nanotube there is a diameter dependent bandgap.

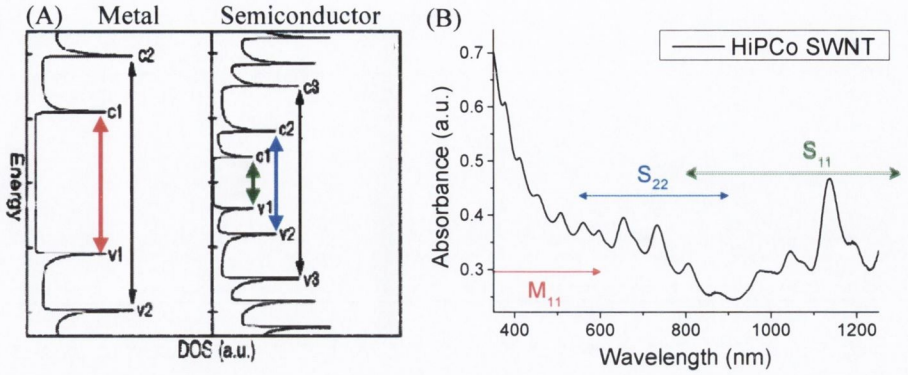


Figure 2-7 (A) Density of electronic states for a metallic and a semiconducting SWNT, showing the allowed optical transitions. (B) Absorption Spectrum for HiPCO SWNTS showing the corresponding positions of the optical transitions shown in (A).

2-1-2 Optical Properties

When a time-dependent electric field (such as a light wave) acts on a molecule (such as a nanotube), the electrons in the molecule experience a time-dependent varying potential which can cause their energy states to change with time. Thus photons can be absorbed, causing electronic transitions between different energy states, if they are allowed by selection rules. The magnitude of absorption at any wavelength is determined by the transition rate ($W_{i\text{-}f}$) for the optical transition of electrons from an initial state (ψ_i) to a final state (ψ_f), due to the absorption of photons as given by Fermi's golden rule[19,20]:

$$W_{i-f} = \frac{2\pi}{\hbar}|\mathbf{M}|^2 g(E)$$

where **M** is a matrix describing the transition dipole moment and $g(E)$ is the joint density of states evaluated at the photon energy. The transition rate is proportional to the square of the transition dipole moment and an optical transition will only occur if the transition dipole moment is non-zero. The transition dipole moment is defined as[21]

$$\mathbf{M} = \int \psi_f^* H' \psi_i \, d\tau$$

where H' is the perturbation associated with the light wave.

H' can be evaluated further by adopting a semi-classical approach in which the electrons are treated quantum mechanically, while the light is treated as an electromagnetic wave. Thus, the interaction between the light and the photon can be described by the electric dipole interaction between the light and the electron as[17]:

$$H' = -\mathbf{p}_e \cdot \mathcal{E}$$

where $\mathcal{E}$ is the electric field of the light and $\mathbf{p}_e$ is the electron dipole moment.

$$\mathbf{p}_e = -e\mathbf{r}$$

where e is the charge of the electron and $\mathbf{r}$ is the position vector of the electron. The electric field of the light, $\mathcal{E}$, can be described by a plane wave as:

$$\mathcal{E}(\mathbf{r}) = \mathcal{E}_0 \, e^{\pm i.\mathbf{k}.\mathbf{r}}$$

where $\mathcal{E}_0$ is the amplitude of the light, $\mathbf{k}$ is the wave vector and $\mathbf{r}$ is the position vector. Thus, the perturbation associated with the light is[17]:

$$H' = e\mathcal{E}_0 \cdot \mathbf{r} \, e^{\pm i.\mathbf{k}.\mathbf{r}}$$

The electronic states in a periodic crystal lattice take on some of the characteristics of the crystal lattice and are described by Bloch functions as the product of a plane wave and an envelope function, $u(\mathbf{r})$, that has the periodicity of the crystal lattice:

$$\psi(\mathbf{r}) = u(\mathbf{r})e^{i\mathbf{k}\cdot\mathbf{r}}$$

Thus, the transition dipole moment can be written as[17,21]:

$$\mathbf{M} = \frac{e}{V}\int u_f^*(\mathbf{r})e^{-i\mathbf{k}_f\cdot\mathbf{r}}\left(\varepsilon_0 \cdot \mathbf{r}e^{\pm i\mathbf{k}\cdot\mathbf{r}}\right)u_i(\mathbf{r})e^{-i\mathbf{k}_i\cdot\mathbf{r}}d^3\mathbf{r}$$

where V is the normalisation volume and $\mathbf{k_i}$ and $\mathbf{k_f}$ are the wave vectors of the initial and final states respectively.

The transition dipole moment represents the movement of charge density for a given optical transition where an electron is promoted from the ground state to an excited state[22]. A larger movement of charge density results in a greater absorption. The maximum absorption occurs when the incident light is polarised in the direction of the transition dipole moment. The selection rules can be established by determining the conditions for which $\mathbf{M} \neq 0$.

The selection rules for nanotubes have been calculated by a number of different groups[18,23,24]. They are described in terms of two quantum numbers — the wave vector, *k*, and the quasi-angular momentum quantum number, *J*. Conservation of momentum demands the change in an electron's momentum must be equal to the momentum of the absorbed photon.

$$\hbar\mathbf{k}_f = \hbar\mathbf{k}_i \pm \hbar\mathbf{k}$$

where $\mathbf{k}_i$ and $\mathbf{k}_f$ are the wave vectors of the initial and final electron states and $\mathbf{k}$ is the wave vector of the incident photon. The wave vector of a photon is defined as $2\pi/\lambda$ where λ is the wavelength of the light. This value is extremely small in comparison to the electron wave vector and can effectively be neglected, giving the first selection rule:

$$\Delta\mathbf{k} \approx 0.$$

Thus, the wave vector of the electron is essentially unchanged by the absorption of a photon.

The van Hove singularities in the DOS of a nanotube are labelled according to the quasi-angular momentum quantum number (*J*) from their corresponding electronic bands. Electronic transitions are allowed between different van Hove singularities. However, because of symmetry restrictions, non-zero transition dipole moments only exist in two directions — parallel and perpendicular to the nanotube axis. Thus, the allowed transitions depend on the polarisation of the incident light. When the incident light is polarised parallel to the nanotube axis, transitions are allowed between bands of the same symmetry where:

$$\Delta J = 0.$$

For perpendicularly polarised light, the allowed transitions are those for which:

$$\Delta J = \pm 1.$$

The perpendicular transition dipole moment is very small in comparison to the parallel transition dipole moment and so the nanotube spectrum is dominated by transition between electronic bands of the same symmetry (eg. E_{11}, E_{22} etc.). The observed nanotube absorption spectrum is therefore defined by a series of van Hove

peaks, at energies corresponding to the interband transition energy, as shown in Figure 2-7 (B). The first van Hove transition for a semiconducting SWNT (S_{11}) falls between 800 nm – 1600 nm, while the second transition (S_{22}) falls in the region of 550 nm – 900 nm. The first transition for metallic tubes (M_{11}) overlaps slightly with the S_{22} transition region, spanning a region from <400 nm to 600 nm[25].

2-1-3 SWNT Synthesis — Carbon Vapour Deposition

Various different methods exist for the production of carbon nanotubes. Most of them are based on the sublimation of carbon under an inert atmosphere (eg. carbon-arc discharge method and laser ablation method) or on chemical methods (eg. chemical vapour deposition). High-pressure carbon monoxide (HiPCO) SWNTs produced using the Carbon Vapour Deposition (CVD) method were used throughout this project. A very brief description of this process is given below[1,26].

Nanotubes (along with amorphous carbon and graphite layers) can be produced by the pyrolisis of hydrocarbons (eg. acetylene, methane, benzene etc.) at high temperatures in the presence of a metal catalyst (eg. Co, Ni, Fe, etc.) The size, shape and degree of graphitisation depend critically on the size and type of catalytic particles used, on the type of hydrocarbon used, on the carrier gas and the temperature.

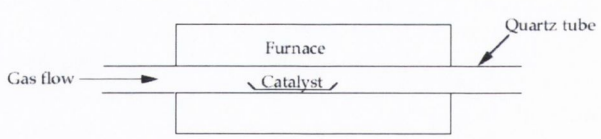


Figure 2-8 Schematic Diagram of CVD apparatus.

In the CVD method, a ceramic boat containing the catalyst is placed in a quartz tube in a flow furnace. A reaction mixture containing the hydrocarbons and a carrier gas flows over the catalyst for several hours at temperatures ranging from 600 °C to 1100 °C. At the end of the time the system is cooled to room temperature. CVD produces nanotubes of various different diameters and shapes (eg. straight, curved,

helical). This is the method used for the mass production of nanotubes by groups such as Rice University who produce HiPCO SWNTs.

2-2 DNA — Introduction

The double-helix structure of deoxyribonucleic acid (DNA), elucidated by Watson and Crick in 1953[27], is one of the world's best recognised biological structures. It is widely known that DNA is the source of all our genetic information.

In complex eukaryotic cells (such as animals, plants and fungi) most of the DNA is found in the cell nucleus. It usually exists as a double-helix of two interwoven strands, though the two strands split up when the cell is dividing or synthesising structural and enzymatic proteins.

2-2-1 Physical Structure of DNA

Each strand of DNA is dominated by a hydrophilic backbone, which consists of alternating sugar and phosphate groups. The sugar is a pentose (five-membered sugar ring) called deoxyribose. It is shown in Figure 2-9 (A) with the carbon atoms labeled from 1' to 5'. The hydrogen (H'') at the 2' position can be replaced by a hydroxyl group to form ribose (the sugar found in ribonucleic acid (RNA)). It is sterically and energetically unfavourable for the sugar to form a planar ring, instead a carbon atom (either 2' or 3') lifts out of the plane to reduce the strain and lower the energy, thus producing a stable conformation. Successive sugar residues are linked together by phosphate groups which form covalent bonds between the carbon 3' and 5' on each ring (Figure 2-9 (B)). The asymmetric bonds give the DNA strand a direction denoted 3'–5' or 5'–3'. When two strands of DNA form a double helix, the strands runs in the opposite directions to each other, and so, DNA is referred to as antiparallel.

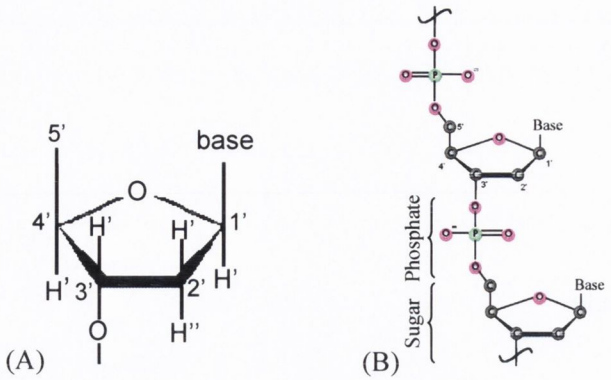


Figure 2-9 (A) The sugar deoxyribose with position of the carbon atoms marked from 1'–5'. The nucleotide base is bonded to C1'. (B) The backbone of DNA is formed from alternating sugar and phosphate groups. The phosphate group is covalently bonded between the 3' and 5' carbon atoms on adjacent sugars.

There are four different planar bases in DNA; two purines — adenine (A) and guanine (G) and two pyridines — thymine (T) and cytosine (C). In RNA, the thymine is replaced by uracil (U) (Figure 2-10). Thymine differs from uracil through the presence of a methyl group attached to a carbon atom on the hexagonal ring. The bases are responsible for the genetic coding information contained within a strand of DNA. The bases attach to the sugar residues at the 1' position. The sugar and the base together are known as a nucleoside. When a phosphate group is also attached it is known as a nucleotide. In double stranded DNA, each base is bonded to another base on the opposite strand with hydrogen bonds. Because of their shape and structure, each base can only bond to its complementary base pair. Adenine bonds to thymine with two hydrogen bonds and guanine bonds to cytosine with three hydrogen bonds (Figure 2-10). The order of the bases on one strand defines the order on the other, providing a simple method for DNA replication. When the cell needs to divide, the DNA 'unzips' and each half is used as a template to create a new complementary strand, thus creating two exact copies of the original DNA.

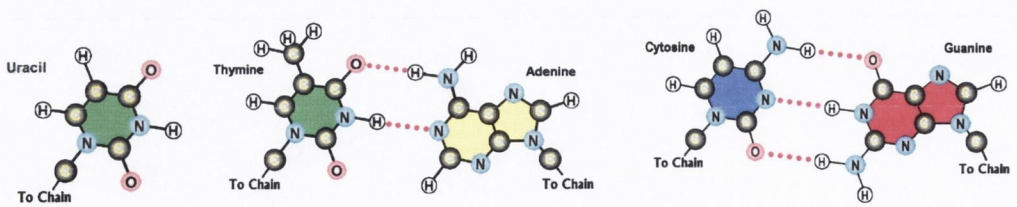


Figure 2-10 Complementary base pairs in DNA — Thymine (T) and Adenine (A), Cytosine (C) and Guanine (G). In RNA, Uracil (U) is found instead of thymine.

The secondary structure of DNA depends strongly on its surrounding environment. DNA will adopt different conformations depending on the temperature, humidity, pH and salt concentration of its surroundings or as a result of interaction with other molecules.

In aqueous solutions, double-stranded DNA usually exists in the so-called B-form[28]. The two polynucleotide chains wind in opposite directions around a common axis with a right-handed twist to form the well-known double helix. The hydrophilic backbones run along the outside of the structure, thus maximising the distance between charged phosphate groups. The hydrophobic bases on each strand stack on each other with their planes almost perpendicular to the helix axis and project into the centre of the structure, bonding to their complementary base pair on the opposite strand via hydrogen bonding. The deoxyribose sugar assumes a C2' endo conformation, where the carbon in position 2' lifts up out of the plane in the C5' direction. The structure has a diameter of ~2.0 nm and ~10 base pairs in a full turn. The vertical base spacing is ~0.34 nm, giving a helical pitch (the rise for 1 full turn) of 3.4 nm.

The double helix has two deep grooves that run along the helix between the two sugar-phosphate backbones. The grooves are unequal in size and are named the minor and major grooves as shown in Figure 2-11. In B-form DNA, the major groove has a width of ~1.2 nm while the minor groove has a width of 0.6 nm. B-form DNA has a persistence length of ~50 nm (in contrast, single-stranded DNA can abruptly change direction over lengths of ~1 nm).

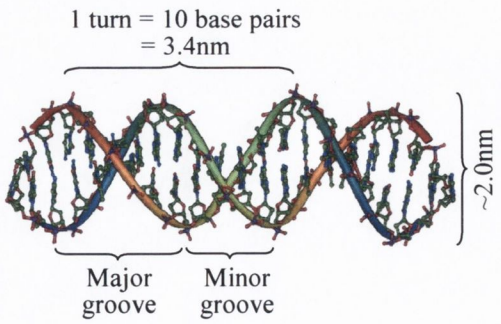


Figure 2-11 B-form DNA with the minor and major grooves shown

DNA can naturally adopt other forms when subjected to different environments. Two common forms are the more compact, right-handed A-form and the left-handed Z-form[29]. The A-form occurs when the relative humidity reduces to 75% or less and is characterised by an increased diameter, a base tilt of 20° with respect to the helix axis and a reduced vertical base spacing. It has a shallow and wide minor groove and a narrower and deeper major groove. Alternatively, B-form DNA can occasionally undergo a transition, switching to the left-handed double helix form known as Z-form DNA. Z-form DNA has 12 base pairs per turn, a helical pitch of 4.4 nm and a deep minor groove, but no major groove. A high-salt concentration is needed to reduce electrostatic repulsion between adjacent phosphate groups in order to stabilise Z-DNA. A-, B-, and Z-DNA are shown in Figure 2-12 while their physical features are compared in Table 2-1[28].

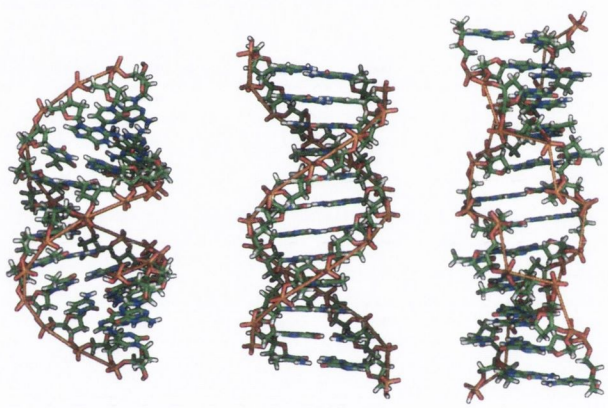


Figure 2-12 From left to right: A-, B- and Z-form DNA

	A	B	Z
Helical Sense	Right handed	Right handed	Left handed
Diameter	~2.6 nm	~2.0 nm	~1.8 nm
Base Pairs per helical turn	11	10	12 (6 dimers)
Helical Twist per base pair	33°	36°	60° (per dimer)
Helix Rise per base pair	0.26 nm	0.34 nm	0.37 nm
Base Tilt normal to helix axis	20°	6°	7°
Major Groove	Narrow & Deep	Wide & Deep	Flat
Minor Groove	Wide & Shallow	Narrow & Deep	Narrow & Deep
Sugar Pucker	C3' endo	C2' endo	C2' endo (pyrimidines) C3' endo (purines)

Table 2-1[28] Comparison of ideal A-, B-, and Z-form DNA.

2-2-2 Optical Properties of DNA

The majority of the optical transitions that are observed in the DNA's absorption spectrum are associated with the bases[22]. The optical transitions in the sugar and the phosphate groups mainly occur at wavelengths below 190 nm making them difficult to study as both oxygen and water are extremely absorbing in this region. The optical transitions occurring within the nucleotide base are generally classified as being either in-the-plane or perpendicular-to-the-plane of the base. Transitions occurring at other angles are forbidden by symmetry restrictions. The in-plane transitions are π — π^* transitions, while the out-of-plane transitions are n — π^* transitions from nonbonding electrons in nitrogen and oxygen being excited into the anti-bonding π^* band. In general the π — π^* transition are much stronger than the n — π^* transitions and so they dominate the absorbance spectrum.

The absorption of a strand of DNA can be attributed to the sum of absorptions of the individual nucleotides minus the effects of the interactions between different nucleotides, which decrease the overall absorption. Consequently, the extinction coefficient of DNA depends on both the nucleotide sequence and the DNA conformation. The origin of this decrease is easily understood in terms of the transition dipole moments of the bases[22]. When a photon is absorbed by a base, there is a movement of charge density, as described by the transition dipole moment. However, when two nucleotide bases are close together they interact with each other. The transition dipole on one base induces a smaller dipole of opposite direction on its neighbouring nucleotide base and vice versa. Thus, for stacked bases, the sum of the original transition dipole plus the induced dipole in the adjacent base is less that the transition dipole of an isolated base. Absorption is proportional to the square of the magnitude of the transition dipole moment and so interaction between stacked bases leads to a reduction in the absorption intensity (hypochromicity). For paired bases, the induced dipole in the complementary base pair could lead to either a decrease or an increase (hyperchromicity) in the magnitude of absorption, depending on the direction of the transition dipole moment. However, for Watson-Crick base-paired DNA, hyperchromicity does not occur for the known transition directions and so a decrease in the absorption is always observed when bases interact with each other[22].

Individual nucleotide bases each have absorption peaks at slightly different wavelengths. The absorption maxima lie at wavelengths of 251 nm, 257 nm, 265 nm and 275 nm for guanine, adenine, thymine and cytosine respectively. In a strand of natural DNA, the absorption peaks from each nucleotide all contribute to create a strong absorption peak at ~260 nm. The purity of the DNA can be ascertained by the ratio of the absorbances at 260 nm and 280 nm. When the DNA is pure, the ratio (A_{260nm}/A_{280nm}) should be ~1.9. A lower value indicates that the DNA is contaminated with proteins.

When a solution containing double-stranded DNA is heated, the DNA can gain enough energy to overcome the hydrogen bonding between the complementary base pairs, allowing it to split into two individual strands. This is known as DNA melting. The shift from double-stranded to single stranded DNA can be monitored by recording the absorbance at 260 nm as a function of temperature. This is known as a melting curve. The temperature at which half the DNA in solution is melted is know as the melting temperature (T_m). Below the melting temperature, the absorbance of the double stranded DNA is constant. However, when the temperature is close to T_m the DNA starts to melt and a large increase in the absorbance in observed as a result of a reduction in the interaction between complementary bases. The melting temperature for a DNA solution is dependent on the length of the DNA and the G ≡ C content of the strands. Longer DNA has a greater number of hydrogen bonds and so needs a greater amount of energy for melting to occur. Guanine and cytosine are bonded with three hydrogen bonds as opposed to adenine and thymine which only have two. Consequently, the higher the G ≡ C content of the DNA, the more energy is needed to overcome the extra hydrogen bonds and melt the DNA.

2-3 Literature Survey

Single-walled carbon nanotubes (SWNTs) have excellent thermal[30], electrical[31] and mechanical properties[32], with many potential applications[33]. However, the realisation of these applications has been severely hindered by the tendency of SWNTs to form bundles. Bundles typically contain thousands of SWNTs[34], making it

impossible to utilise the unique electrical properties of individual nanotubes. In areas such as nanotube-polymer composite formation, the presence of bundles increases the electrical percolation threshold[35], and reduces the effectiveness of SWNTs as mechanical reinforcement agents[36]. Thus, an efficient method of debundling and solubilising nanotubes is required for SWNTs to achieve their full potential. Various different methods of dispersing nanotubes have been reported, including polymer-wrapping[37,38], amide solvents[39,40], surfactants[25,41,42], strong acids[43], surface functionalisation[44], synthetic peptides[45-47] and DNA[48,49]. Comparing the effectiveness of these dispersion techniques is not straightforward because currently there is no consensus on an absolute measure for dispersion efficiency[50]. In addition to this, there is no readily available, single method for the direct measurement of the bundle diameter distribution in solution. A number of different techniques have been utilised to infer the dispersion efficiency. Many of these are based on changes in the optical properties of nanotubes as a result of interactions with adjacent tubes in bundles — most notably NIR photoluminescence[25,41], optical absorption spectroscopy[25,42] and resonant raman spectroscopy[51,52] — while others, such as atomic force microscopy (AFM)[53,54] rely on drying the solutions before examining them. Cryo-TEM is well suited to imaging wet samples and has been utilised to image solutions of carbon nanotubes[42]. However, this technique is not widely available.

A number of separate reports have been published which use different methods to determine the effectiveness of different dispersing agents. Moore *et. al.* presented an extensive study on the effectiveness of different surfactant and polymers in SWNT dispersions[42]. The dispersion efficiency was determined by calculating the fraction of nanotubes (by mass) remaining in solution after ultra-centrifugation. This value should be close the mass of individually dispersed SWNTs in solution, assuming that ultracentrifugation removes the majority of bundles and insoluble material. The nanotube yields after centrifugation were found to be comparable between different ionic surfactants and polymers (~4–5%), while the non-ionic nanotube suspensions showed large variations (0–9.4%). It was concluded that, for non-ionic surfactants and polymers, the size of the hydrophilic group was the most significant factor in achieving high nanotube yields, with higher molecular weights giving better dispersions. A similar study was carried out by Maeda et. al. on the dispersion of SWNTs in non-aqueous solutions[55]. SWNTs were dispersed using a series of amines with different substituents in tetrahydrofuran (THF). The dispersion efficiency was calculated by

measuring the optical absorbance at 1310 nm after centrifugation at 20,000g. It was found that octylamine had the highest dispersion efficiency and that the interaction between amines and SWNTs was dependent on the basicity of the amines. AFM images showed that bundles with diameters of up to 4 nm had remained in solution after centrifugation.

A series of comprehensive studies on nanotube dispersion in different media have been carried out in Trinity College Dublin. In each case, a stock solution was prepared from which a series of serial dilutions were made. The nanotube bundle diameter distribution was then measured as a function of concentration using AFM in conjunction with a number of other techniques, including photoluminescence spectroscopy. It was found that nanotube bundles sizes were dependent on concentration[56] and that large scale debundling occurred upon dilution. Analysis of the bundle diameters allows one to calculate three parameters — the mean bundle diameter, the fraction of individual nanotubes by number and the fraction of individual SWNTs by mass. These values give an indication of the quality of the dispersion. For SWNTs dispersed in the solvent N-methyl-2-pyrrolidone (NMP) the mean diameter was found to decrease with concentration, stabilising at an average minimum value of ~1.9 nm. Yields of 70% individual SWNTs by number, equating to 10% – 20% by mass were achieved at nanotube concentrations of $\leq$0.008 mg/mL[54]. NMP is generally regarded as the best known solvent for nanotubes. By comparison, mean diameter values of 2.4 nm, with 38% individual SWNTs by number or 10% by mass were achieved for SWNTs dispersed in the solvent γ-Butyrolactone (also known as liquid ecstasy)[57]. DNA-SWNT dispersions were found to compare well with mean diameters of 1.7 nm at low concentrations, and yields of 82% individual tubes by number, equating to 6.2% individual SWNTs by mass[53].

The dispersion of SWNT in aqueous DNA solutions with the aid of sonication was first reported by Nakashima et. al. in April 2003[48]. Since then, research has shown DNA to be an excellent dispersant of SWNTs with many exciting possible applications. Much of this research has been carried out by Zheng and co-workers, who focused on producing DNA-SWNT dispersions using short single-stranded oligonucleotides[49]. The absorption spectra of these DNA-SWNT solutions were well resolved and showed a systematic dependence on pH. Strong NIR fluorescence was also observed, suggesting that there was a large population of individually dispersed SWNTs. Computer simulations on the interactions between DNA and the SWNT

suggested that the DNA wraps around the nanotube in such a way that allows the nucleotide bases to interact with the nanotube walls via π-stacking interactions, while the hydrophilic sugar-phosphate backbone creates an interface between the water and the nanotube. Further evidence for DNA wrapping of nanotubes was provided by Dovbeshko *et. al.* using surface enhanced infrared absorption spectroscopy (SEIRA)[58]. They found that there was strong interaction between the DNA and SWNTs and that DNA was present in conformations that were not usually seen under those environments. They concluded that the DNA was being stabilised in these conformations by wrapping around the SWNT. Subsequent literature has shown possible DNA wrapping for both short oligonucleotides[59] and long genomic single-stranded DNA[60] using AFM phase images. However, conclusive high-resolution transmission electron microscopy (HRTEM) images of DNA wrapping have yet to be produced.

One of the most exciting discoveries to date is the technology to obtain large quantities of nearly pure, single chirality nanotubes from DNA-SWNT dispersions[61]. The electrostatic field around a DNA-wrapped SWNT is dependent on the nanotube's electronic character and diameter which enables the dispersions to be separated into different fractions by anionic-exchange liquid chromatography[59]. Oligonucleotides with sequences of alternating guanine and thymine (poly d(GT)) and total lengths ranging from 20 to 90 bases were found to be best for separating semiconducting nanotubes, possibly due to a limited number of allowed wrapping angles resulting from its ability to form highly ordered structures on the SWNTs[62]. All fractions were shown to demonstrate strong photoluminescence, supporting the claim that the majority of nanotubes are dispersed individually[63]. The PL peak positions for DNA-wrapped nanotubes are shifted slightly in relation to that of SWNTs dispersed with sodium dodecyl sulphate (SDS) in water as a result of the differences in the nanotube's immediate environment[41,64]. Size-exclusion chromatography (SEC) was then used to separate the DNA-SWNTs dispersions into different lengths and remove the impurities[65].

The separation of semiconducting tubes by diameter has also been demonstrated by Arnold[66]. In this work, a DNA-SWNT dispersion was placed in a density gradient of iodixanol and centrifuged at 174,000g for 10 ½ hrs. At the end of this time the DNA-coated SWNTs had separated into sharp bands with different colours.

Two issues of concern for DNA-SWNT dispersions were the possible need to be able to remove the DNA from the SWNTs at some later stage in the process and the possibility that the DNA could be bonding covalently to the nanotube, thus changing the nanotube's electronic properties. This was addressed by Chen *et. al.* who showed that short homo-oligonucleotides, such as $d(T)_{30}$, can be removed from the SWNTs using either its complementary DNA strand or small extended aromatic molecules such as rhodamine 6G and methylene blue[67].

A variety of possible applications for DNA-SWNT dispersions have been investigated. These include fibre spinning from DNA-SWNT dispersions[68]; using the molecular recognition properties of DNA to self-assemble nanotube field-effect transistors[69]; using DNA-wrapped SWNTs to stabilize colloidal particles[70]; and the use of DNA-SWNT hybrids for chemical sensing[71]. DNA-SWNT dispersions show particular promise for use within medical diagnostic and biological fields. Firstly, the dispersions are water-based, which is necessary for biocompatibility and secondly, the DNA interacts with the SWNTs through non-covalent hydrogen bonding which preserves the electronic and optical properties of the nanotubes[61,64]. Semiconducting nanotubes emit in the NIR region, where human tissues and blood are optically transparent[72]. In addition, few biological systems naturally fluoresce in this region, removing the problem of background fluorescence that decreases the sensitivity of current techniques which rely on visible fluorescence[73]. It has been found that the nanotube fluorescence can be modified slightly by the nanotubes' environment[72,74,75], allowing their potential use as tiny biosensors. Consequently, sensors are now being developed which utilise the nanotube's NIR emission properties in conjunction with specific recognition biosystems, such as enzymes which recognise specific target biomolecules[72,76]. It has been found, that DNA can facilitate the immobilisation of the enzyme on the nanotube, while minimising the reduction in enzyme activity[72]. The advantage of such a biosensor is that the tiny device could potentially be implanted into living tissue[73,77], allowing for continuous monitoring of a target biomolecule, such a glucose[72] or dopamine[78]. Studies already show that DNA-wrapped nanotubes can be used as photo-bleaching resistant, non-quenching cell markers which remained functional in live mammalian cells for up to three months[73]. Thus, DNA-SWNTs biosensors have the potential to revolutionise the treatment of many diseases and illnesses in the future.

2-4 References

(1) Terrones, M. *International Materials Reviews* **2004**, *49*, 325.
(2) Atkins P, J. L. *4th ed. W.H. Freeman and Co. New York* **1999**.
(3) Iijima, S. *Nature* **1991**, *354*, 56.
(4) Iijima, S.; Ichihashi, T. *Nature* **1993**, *363*, 603.
(5) Hongjie, D. *Surface Science* **2002**, *500*, 218.
(6) Ajayan, P. M.; J-C, C.; G, R. A. *PNAS* **1999**.
(7) Dresselhaus, M. S. *Physics World* **1998**, 33.
(8) Dresselhaus, M. S. Future directions in carbon science Annual Reviews Inc, Palo Alto, CA, USA, 1997; Vol. 27; pp 1.
(9) Ajayan, P. M. *Handbook of Nanostructured Materials and Nanotechnology.* ; Academic Press, 2000; Vol. 5.
(10) Dresselhaus, M. S.; Dresselhaus, G.; Saito, R.; Jorio, A. *Physics Reports* **2005**, *409*, 47.
(11) Rainer, W. *Nanoelectronics and Information Technology*; Wiley VCH, : Germany, 2003.
(12) Wallace, P. R. *Physical Review* **1947**, *71*, 622.
(13) Ventra, M. D.; Evoy, S.; Jr., J. R. H. *Introduction to Nanoscale Science and Technology*; Kluwer Academic Publishers, 2004.
(14) Hamada, N.; Sawada, S.; Oshiyama, A. *Physical Review Letters* **1992**, *68*, 1579.
(15) Wildoer, J. W. G.; Venema, L. C.; Rinzler, A. G.; Smalley, R. E.; Dekker, C. *Nature* **1998**, *391*, 59.
(16) Samsonidze, G. G. *e. a. Applied Physics Letters* **2004**, *85*, 5703.
(17) Fox, M. *Optical Properties of Solids*; Oxford University Press: Oxford, 2001.
(18) Bozovic, I.; Bozovic, N.; Damnjanovic, M. *Physical Review B (Condensed Matter)* **2000**, *62*, 6971.
(19) Dirac, P. A. M. *Proceedings of the Royal Society of London. Series A* **1927**, *114*, 243.
(20) Fermi, E. *Nuclear Physics*; University of Chicago Press: Chicago, 1950.
(21) Atkins, P. W. *Physical Chemistry*, 3rd Edition ed.; Oxford University Press: Oxford, 1986.
(22) Bloomfield, V. A.; Crothers, D. M.; Tinoco, I. *Nucleic Acids: Structures, Properties and Functions*; University Science Books: California, 2000.
(23) Saito, R.; Gruneis, A.; Samsonidze, G. G.; Dresselhaus, G.; Dresselhaus, M. S.; Jorio, A.; Cancado, L. G.; Pimenta, M. A.; Souza Filho, A. G. *Applied Physics A (Materials Science Processing)* **2004**, *A78*, 1099.
(24) Barros, E. B.; Capaz, R. B.; Jorio, A.; Samsonidze, G. G.; Filho, A. G. S.; Ismail-Beigi, S.; Spataru, C. D.; Louie, S. G.; Dresselhaus, G.; Dresselhaus, M. S. *Physical Review B (Condensed Matter and Materials Physics)* **2006**, *73*, 241406.
(25) O'Connell, M. J.; Bachilo, S. H.; Huffman, C. B.; Moore, V. C.; Strano, M. S.; Haroz, E. H.; Rialon, K. L.; Boul, P. J.; Noon, W. H.; Kittrell, C.; Ma, J.; Hauge, R. H.; Weisman, R. B.; Smalley, R. E. *Science* **2002**, *297*, 593.
(26) Journet, C.; Bernier, P. *Applied Physics A: Materials Science & Processing* **1998**, *67*, 1

(27) Watson, J. D.; Crick, F. H. C. *Nature* **1953**, *171*, 737.
(28) Voet, D.; Voet, J. G. *Biochemistry*; John Wiley and Sons Inc: New York, 1995.
(29) Gao, H.; Kong, Y. *Annual Review of Materials Research* **2004**, *34*, 123.
(30) Berber, S.; Kwon, Y.; Tománek, D. *Physical Review Letters* **2000**, *84*, 4613.
(31) Wei, B. Q.; Vajtai, R.; Ajayan, P. M. *Applied Physics Letters* **2001**, *79*, 1172.
(32) Coleman, J. N.; Khan, U.; Gun'ko, Y. K. *Advanced Materials* **2006**, *18*, 689.
(33) Baughman, R. H.; Zakhidov, A. A.; De Heer, W. A. *Science* **2002**, *297*, 787.
(34) Zhao, J. *Literature Review, University of Cincinnati* **2001**.
(35) Munson-McGee, S. H. *Physical Review B (Condensed Matter)* **1991**, *43*, 3331.
(36) Cadek, M.; Coleman, J. N.; Ryan, K. P.; Nicolosi, V.; Bister, G.; Fonseca, A.; Nagy, J. B.; Szostak, K.; Beguin, F.; Blau, W. J. *Nano Letters* **2004**, *4*, 353.
(37) Manchado, M. A. L.; Valentini, L.; Biagiotti, J.; Kenny, J. M. *Carbon* **2005**, *43*, 1499.
(38) Steuerman, D. W. *Journal of Physical Chemistry B* **2002**, *106*, 3124.
(39) Furtado, C. A.; Kim, U. J.; Gutierrez, H. R.; Pan, L.; Dickey, E. C.; Eklund, P. C. *Journal of the American Chemical Society* **2004**, *126*, 6095.
(40) Landi, B. J.; Ruf, H. J.; Worman, J. J.; Raffaelle, R. P. *Journal of Physical Chemistry B* **2004**, *108*, 17089.
(41) Bachilo, S. M.; Strano, M. S.; Kittrell, C.; Hauge, R. H.; Smalley, R. E.; Weisman, R. B. *Science* **2002**, *298*, 2361.
(42) Moore, V. C.; Strano, M. S.; Haroz, E. H.; Hauge, R. H.; Smalley, R. E.; Schmidt, J.; Talmon, Y. *Nano Lett.* **2003**, *3*, 1379.
(43) Penicaud, A.; Poulin, P.; Derre, A. *Journal of the American Chemical Society* **2005**, *127*, 8.
(44) Koshio, A.; Yudasaka, M. *Nano Lett.* **2001**, *1*, 361.
(45) Ortiz-Acevedo, A.; Xie, H.; Zorbas, V.; Sampson, W. M.; Dalton, A. B.; Baughman, R. H.; Draper, R. K.; Musselman, I. H.; Dieckmann, G. R. *Journal of the American Chemical Society* **2005**, *127*, 9512.
(46) Dalton, A. B.; Ortiz-Acevedo, A.; Zorbas, V.; Brunner, E.; Sampson, W. M.; Collins, S.; Razal, J. M.; Yoshida, M. M.; Baughman, R. H.; Draper, R. K.; Musselman, I. H.; Jose-Yacaman, M.; Dieckmann, G. R. *Advanced Functional Materials* **2004**, *14*, 1147.
(47) Dieckmann, G. R.; Dalton, A. B.; Johnson, P. A.; Razal, J.; Chen, J.; Giordano, G. M.; Munoz, E.; Musselman, I. H.; Baughman, R. H.; Draper, R. K. *Journal of the American Chemical Society* **2003**, *125*, 1770.
(48) Nakashima, N.; Okuzono, S.; Murakami, H.; Nakai, T.; Yoshikawa, K. *Chemistry Letters* **2003**, *32*, 456
(49) Zheng, M.; Jagota, A.; Semke, E. D.; Diner, B. A.; McLean, R. S.; Lustig, S. R.; Richardson, R. E.; Tassi, N. G. *Nature Materials* **2003**, *2*, 338.
(50) Fagan, J. A.; Landi, B. J.; Mandelbaum, I.; Simpson, J. R.; Bajpai, V.; Bauer, B. J.; Migler, K.; Walker, A. R. H.; Raffaelle, R.; Hobbie, E. K. *Journal of Physical Chemistry B* **2006**, *110*, 23801.
(51) Heller, D. A.; Barone, P. W.; Swanson, J. P.; Mayrhofer, R. M.; Strano, M. S. *Journal of Physical Chemistry B* **2004**, *108*, 6905.
(52) Fantini, C.; Jorio, A.; Souza, M.; Strano, M. S.; Dresselhaus, M. S.; Pimenta, M. A. *Physical Review Letters* **2004**, *93*, 147406.

(53) Cathcart, H.; Quinn, S.; Nicolosi, V.; Kelly, J. M.; Blau, W. J.; Coleman, J. N. *J. Phys. Chem. C* **2007**, *111*, 66.
(54) Giordani, S.; Bergin, S. D.; Nicolosi, V.; Lebedkin, S.; Kappes, M. M.; Blau, W. J.; Coleman, J. N. *Journal of Physical Chemistry B* **2006**, *110*, 15708.
(55) Maeda, Y.; Kimura, S.; Hirashima, Y.; Kanda, M.; Lian, Y.; Wakahara, T.; Akasaka, T.; Hasegawa, T.; Tokumoto, H.; Shimizu, T.; Kataura, H.; Miyauchi, Y.; Maruyama, S.; Kobayashi, K.; Nagase, S. *Journal of Physical Chemistry B* **2004**, *108*, 18395.
(56) Coleman, J. N.; Fleming, A.; Maier, S.; O'Flaherty, S.; Minett, A. I.; Ferreira, M. S.; Hutzler, S.; Blau, W. J. *Journal of Physical Chemistry B* **2004**, *108*, 3446.
(57) Bergin, S. D.; Nicolosi, V.; Giordani, S.; Gromard, A. d.; Carpenter, L.; Blau, W. J.; Coleman, J. N. *Submitted* **2007**.
(58) Dovbeshko, G. I.; Repnytska, O. P.; Obraztsova, E. D.; Shtogun, Y. V. *Chemical Physics Letters* **2003**, *372*, 432.
(59) Zheng, M.; Jagota, A.; Strano, M. S.; Santos, A. P.; Barone, P.; Chou, S. G.; Diner, B. A.; Dresselhaus, M. S.; McLean, R. S.; Onoa, G. B.; Samsonidze, G. G.; Semke, E. D.; Usrey, M.; Walls, D. J. *Science* **2003**, *302*, 1545.
(60) Gigliotti, B.; Sakizzie, B.; Bethune, D. S.; Shelby, R. M.; Cha, J. N. *Nano Lett.* **2006**, *6*, 159.
(61) Onoa, B.; Zheng, M.; Dresselhaus, M. S.; Diner, B. A. *Physica Status Solidi (A) Applied Research* **2006**, *203*, 1124.
(62) Lustig, S. R.; Jagota, A.; Khripin, C.; Zheng, M. *Journal of Physical Chemistry B* **2005**, *109*, 2559.
(63) Strano, M. S.; Ming, Z.; Jagota, A.; Bibiana Onoa, G.; Heller, D. A.; Barone, P. W.; Usrey, M. L. *Nano Letters* **2004**, *4*, 543.
(64) Chou, S. G.; Ribeiro, H. B.; Barros, E. B.; Santos, A. P.; Nezich, D.; Samsonidze, G. G.; Fantini, C.; Pimenta, M. A.; Jorio, A.; Filho, F. P.; Dresselhaus, M. S.; Dresselhaus, G.; Saito, R.; Zheng, M.; Onoa, G. B.; Semke, E. D.; Swan, A. K.; Unlu, M. S.; Goldberg, B. B. *Chemical Physics Letters* **2004**, *397*, 296.
(65) Huang, X.; McLean, R. S.; Zheng, M. *Analytical Chemistry* **2005**, *77*, 6225.
(66) Arnold, M. S.; Stupp, S. I.; Hersam, M. C. *Nano Lett.* **2005**, *5*, 713.
(67) Chen, R. J.; Zhang, Y. *Journal of Physical Chemistry B* **2006**, *110*, 54.
(68) Barisci, J. N.; Tahhan, M.; Wallace, G. G.; Badaire, S.; Vaugien, T.; Maugey, M.; Poulin, P. *Advanced Functional Materials* **2004**, *14*, 133.
(69) Keren, K.; Berman, R. S.; Buchstab, E.; Sivan, U.; Braun, E. *Science* **2003**, *302*, 1380.
(70) Hobbie, E. K.; Bauer, B. J.; Stephens, J.; Becker, M. L.; McGuiggan, P.; Hudson, S. D.; Wang, H. *Langmuir* **2005**, *21*, 10284.
(71) Staii, C.; Johnson, A. T.; Chen, M.; Gelperin, A. *Nano Lett.* **2005**, *5*, 1774.
(72) Karachevtsev, V. A.; Glamazda, A. Y.; Leontiev, V. S.; Lytvyn, O. S.; Dettlaff-Weglikowska, U. *Chemical Physics Letters* **2007**, *435*, 104.
(73) Heller, D. A.; Baik, S.; Eurell, T. E.; Strano, M. S. *Advanced Materials* **2005**, *17*, 2793.
(74) Choi, J. H.; Strano, M. S. *Applied Physics Letters* **2007**, *90*, 223114.

(75) Strano, M. S.; Huffman, C. B.; Moore, V. C.; O'Connell, M. J.; Haroz, E. H.; Hubbard, J.; Miller, M.; Rialon, K.; Kittrell, C.; Ramesh, S.; Hauge, R. H.; Smalley, R. E. *Journal of Physical Chemistry B* **2003**, *107*, 6979.

(76) Rao, K. S.; Daniel, S.; Rao, T. P.; Rani, S. U.; Naidu, G. R. K.; Hea-Yeon, L.; Kawai, T. *Sensors and Actuators B (Chemical)* **2007**, *122*, 672.

(77) Heller, D. A.; Jeng, E. S.; Tsun-Kwan, Y.; Martinez, B. M.; Moll, A. E.; Gastala, J. B.; Strano, M. S. *Science* **2006**, *311*, 508.

(78) Hu, C.; Zhang, Y.; Bao, G.; Zhang, Y.; Liu, M.; Wang, Z. L. *Journal of Physical Chemistry B* **2005**, *109*, 20072.

Chapter 3

Materials and Methods

3-1 Materials

HiPCO single walled nanotubes[1] (SWNTs) with diameters of 0.7–1.4 nm, purchased from Carbon Nanotechnologies Inc[2], were used throughout all experiments. The SWNTs were produced in the form of small pellets with diameters of 1–2 mm and weights ranging between 0.03 mg and 2.5 mg.

Nanotube dispersions were prepared using a variety of natural and synthetic DNAs, plus custom synthesised oligonucleotides as the dispersants. The majority of samples were prepared with natural double-stranded DNA. In particular, three DNA types; herring sperm DNA[3]; salmon testes DNA[4] and calf thymus DNA[5] were used. For comparison, other dispersions were prepared using poly(rA), a synthetic, single-stranded RNA with average lengths of 465–660 bases[6]. Finally, dispersions were also prepared using four different custom-synthesised oligonucleotides — dA_{15}, dT_{15}, dC_{15} and dG_{15}[7]. All oligonucleotide were single-stranded, consisting of just 15 nucleotides and one type of base — adenine, thyme, cytosine and guanine respectively.

The DNA stock solutions were prepared by sonicating the DNA in either Millipore water or deuterium oxide (D_2O)[8] at a concentration of 1 mg/mL for 15 minutes in an ice sonic bath. The DNA lengths after sonication were ascertained by Dr. Sara Callagy by agarose gel electrophoresis. Sonication shears the DNA, slicing it into shorter lengths and thus, a wide range of DNA lengths were observed. Both salmon testes and calf thymus DNA were found to have lengths ranging from ~10,000 to ~100 base pairs, with the majority of the DNA falling at the upper end of this scale. Herring sperm DNA was found to be much shorter, with lengths ranging from 200 base pairs to just a few base pairs. It should be noted that in the following chapters, when concentration is mentioned, it refers to the concentration of nanotubes in solution unless otherwise stated. All ratios refer to the ratio of DNA to SWNTs (DNA:SWNT) as measured by mass.

3-2 Methods of Analysis

The DNA-SWNT solutions were analysed using a variety of spectroscopic and microscopic techniques. A brief summary of each of the main techniques is given below.

3-2-1 Absorption Spectroscopy

Absorption spectroscopy is a technique in which the attenuation of a beam of light is measured as it passes through a sample or reflects off a sample surface. Briefly, a beam of light is split into its component wavelengths by a monochrometer before passing through a sample[9]. As the beam passes through the sample, its intensity reduces as a result of absorption and scattering of the light[10]. The spectrometer scans through a range of wavelengths, showing the attenuation of the beam as a function of wavelength.

The absorption of a photon of light in UV-visible range by a molecule can result in both n – π* and π – π* transitions. Electronic transitions will only occur if the photon energy is equal to the energy gap, thus[11]:

$$\Delta E = E_2 - E_1 = h\upsilon = hc/\lambda$$

where E_1 and E_2 are the energies of initial and final states of the electron respectively, h is Planck's constant, c is the speed of light and υ and λ are the frequency and wavelength of the absorbed photon respectively. Consequently, the absorption spectrum of a molecule yields information about its excited states[9].

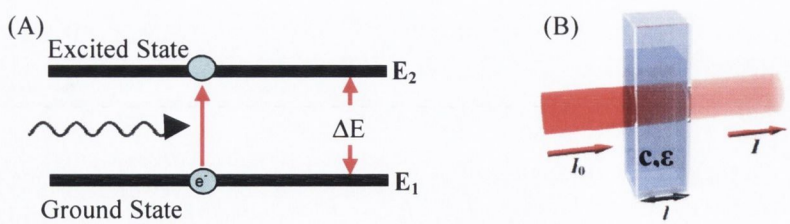


Figure 3-1 (A) Electronic transition due to the absorption of a photon. (B) Transmission of light through a cuvette

The reduction in intensity of light as it passes through a sample of concentration (C), and extinction coefficient (ε), is described by the Lambert-Beer Law as[12]:

$$I = I_0 e^{-\varepsilon C l}$$

where I_0 and I are the initial and final intensities of the beam respectively and l is the sample pathlength. The extinction coefficient for a molecule at a given wavelength is defined by the transition dipole moment as described in Section 2-1-2. The dimensionless product, $A = \varepsilon Cl$, is known as the absorbance of the sample, while I/I_0 is referred to as the transmittance of the sample. Generally absorbance spectrometers show absorbance as a function of wavelength. A knowledge of the absorbance of a sample allows one to calculate the sample concentration, if ε and l are known. For nanotubes, the absorption spectrum contains a strong background scattering component which is particularly large at shorter wavelength. The background scattering is due to both Rayleigh and Mie scattering, but is further complicated by a pi plasmon component. The scattering does not follow a simple λ^{-n} dependence, making it very difficult to remove this contribution from the absorbance spectrum. However, it was found that for DNA-SWNT dispersions, the absorbance (including the scattering contribution) scales linearly with concentration and intercepts the origin (Section 5-3-7). Thus, the calculated extinction coefficient (ε_{720nm} = 2700 $mL.mg^{-1}.m^{-1}$) takes account of the scattering component, allowing one to calculate the nanotube concentration of the sample. Where the contribution from absorption alone is of interest, we have subtracted a straight-line background scattering component from the absorption peak as shown in Figure 4-7. These measurements are then referred to as the absorption 'peak height' throughout this thesis. All UV-VIS-NIR absorption spectra were recorded with a Perkin-Elmer Lambda 900 spectrophotometer unless stated otherwise.

3-2-2 Circular Dichroism Spectroscopy

Circular dichroism spectroscopy is based on the differential absorption of right- and left-handed polarised light. Generally, it is used to gain additional information on the secondary structure of either DNA or proteins. The intensity of absorption depends

on the movement of charge density, as described by the transition dipole moment. When the charge density moves along a helical path, the molecular structure will have different magnitudes of absorption for left- and right-handed polarised light[13]. This helical electron motion occurs in chiral molecular structures, giving them a circular dichroism spectrum.

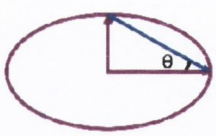
The differential absorbance (ΔA) is defined as:

$$\Delta A = A_L - A_R$$

where A_L and A_R are the absorbance of left- and right-hand circular polarised light respectively. The circular dichroism ($\Delta\varepsilon$) of the sample can be calculated from the differential absorbance via:

$$\Delta\varepsilon = \Delta A/Cl = \varepsilon_L - \varepsilon_R$$

where ε_L and ε_R are the extinction coefficient for left- and right-circularly polarised light respectively, C is the concentration and l is the sample pathlength. For historical reasons, circular dichroism is often measured in units of degrees of ellipticity. This is based on the fact that an absorbing chiral substance can change linearly polarised light (consisting of equal magnitudes of right- and left-circularly polarised light) into elliptically polarised light as a result of differential absorption. The ellipse is characterised by an angle θ, where $\tan\theta$ is equal to the ratio of the minor to the major axis of the ellipse. For small values of θ,



$$\tan\theta = \sin\theta / \cos\theta \approx \theta$$

The ellipticity is related to the circular dichroism of the sample according to the equation:

$$[\theta] = 3298\ \Delta\varepsilon$$

The CD of a polynucleotide is equal to the sum of the CD of its nucleotides, plus the effects of the interactions between nucleotides, which greatly increase the intensity of the signal, making it very sensitive to the conformation of the DNA. Thus CD is sensitive to both the stacking geometry of the bases within a single-strand of DNA and the interactions between bases on separate strands in double stranded DNA. The pattern of the CD spectrum allows one to differentiate between the A-, B- and Z-

conformations of DNA. While the exact shape and magnitude of the spectrum depend on the sequence of the bases, the overall pattern of the spectra remain the same, allowing one to identify different conformations. All CD spectra were recorded using a Jasco J-810 Spectropolarimeter.

3-2-3 Photoluminescence Spectroscopy

Photoluminescence (PL) spectroscopy is a non-destructive method of probing the electronic band structure of a semiconductor. It is a process in which an electron that has been excited into the conduction band relaxes into the valence band, emitting a photon with energy equal to that of the band gap[10].

PL can be observed from individually dispersed semiconducting nanotubes[14]. The absorption of photons gives rise to a series of optical transitions with energies denoted E_{11}, E_{22} etc. as described earlier in Section 2-1-2. In metallic nanotubes there are allowed energy states at the Fermi level, and so the exciton decays through non-radiative relaxation processes. However, in semiconducting nanotubes the exciton relaxes into the lowest energy band before recombining and emitting a photon, as shown in schematically in Figure 3-2 (A)[15]. Only individual nanotubes and small bundles containing just semiconducting SWNTs fluoresce. When aggregation occurs, interactions with metallic SWNTs mean that the exciton can decay by non-radiative relaxation processes, effectively quenching the PL. Thus, PL provides a spectroscopic method of characterising the individually dispersed semiconducting SWNTs in solution. A PL map for a DNA-nanotube solution is shown in Figure 3-2B. The sample is excited over an energy range corresponding to the E_{22} transitions, while the emitted radiation is detected over an energy range corresponding to nanotubes' E_{11} transitions. A number of distinct peaks can be seen, each corresponding to a different (n,m) species of semiconducting nanotubes. A knowledge of the E_{11} and E_{22} transition energies for different nanotubes allows each peak to be assigned to a different nanotube species[16]. The position of these peaks can shift slightly, depending on the environment around the nanotube[17-20].

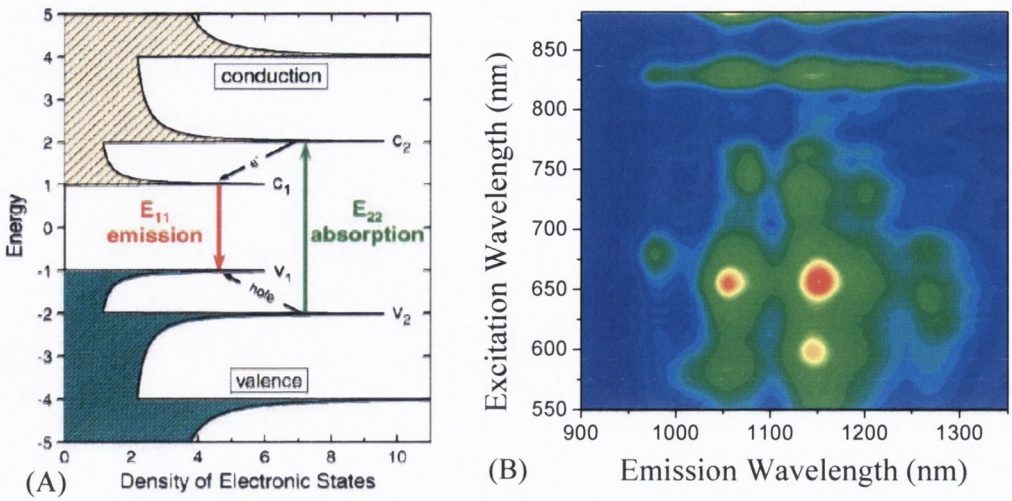


Figure 3-2[15] (A) DOS of a semiconducting nanotube with E_{22} absorption and E_{11} emission. (B) PL map for HiPCO SWNTs. Each peak corresponds to an (n,m) family of nanotubes.

When working at low concentrations, the PL emission intensity is generally proportional to the number emitting species, in this case the number of emitting SWNTs. However, when working at higher concentrations, the PL can deviate from this linear relationship as a result of a number of separate effects[21]. Firstly, for highly concentrated solutions, it is possible for all the incident light to be absorbed and re-emitted, giving a maximised PL signal. Thus, any further increase in the number of emitting species will fail to further increase the emission and the PL signal will saturate. Another important effect observed at high concentrations is the inner-filter effect. This effect occurs in cases where the detector only 'sees' light that is emitted from the very centre of the cuvette. Thus, any light that is absorbed and re-emitted from the regions around the edges cannot be detected, reducing the observed PL intensity. This effect can be reduced by using a small cuvette which is matched to the geometry of the spectrometer. Finally, when the PL and absorption spectra overlap, the emitted light can be re-absorbed by the solution preventing it from reaching the detector and leading to a decrease in the observed photoluminescence. Thus, these three effects must be accounted for when working at high nanotube concentrations[21].

Finally, the observed PL spectra consist of the emission from the individual SWNTs plus a contribution from the dark count from the NIR detector which leads to

a constant experimental error. This dark count was reduced by cooling the NIR-detector to -80 °C and then removing the remaining dark count from each spectrum by subtracting an appropriate straight-line baseline.

NIR-PL measurements in this work were made using an Edinburgh Instruments FLS920 fluorescence spectrometer with a Hamamatsu R5509 near-IR photomultiplier tube.

3-2-4 Atomic Force Microscopy

The atomic force microscope (AFM) belongs to the family of scanning probe microscopes. The basic mechanism consists of moving a very sharp probe across the surface of the sample, while monitoring the sample-tip interactions. When the apex of the AFM tip and the sample surface are in close proximity, they exert a force on each other, the magnitude and direction of which is dependent on the distance between them, as described by the Lennard-Jones function (Figure 3-3 left). When there is a small separation between the tip and the sample surface, an attractive force is experienced between them, causing the cantilever to bend slightly towards the sample. However as the distance between them reduces further, a strong repulsive force is experienced, causing the cantilever to bend away from the sample. Thus, as the tip scans the sample surface, the cantilever is deflected, tracing out the profile of the surface.

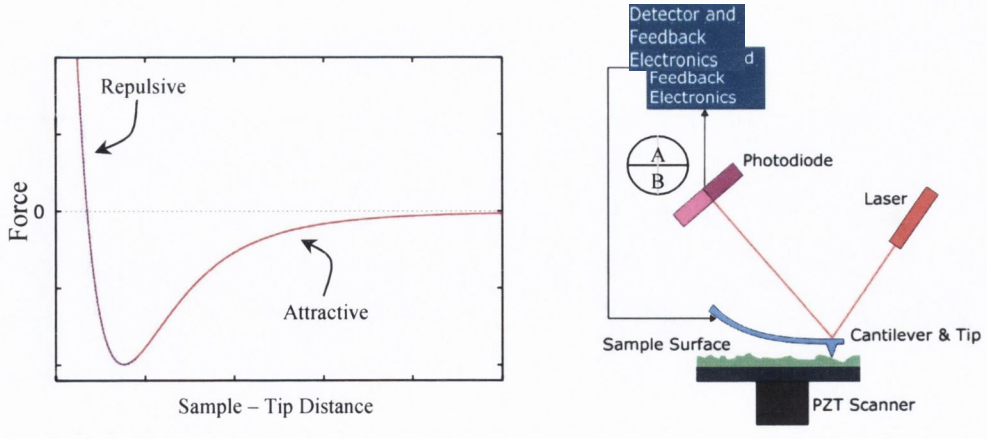


Figure 3-3 (Left) Plot of the Lennard-Jones Function and (Right) Simplified diagram of an AFM

Figure 3-3 (right) shows a simplified schematic diagram of an AFM. The sample is mounted on a piezoelectric column, which allows the specimen to be scanned in the x and y directions, while modulating the height in the z-direction. A flexible cantilever, with a sharp tip mounted on the end, scans across the sample surface. The variations in the sample height are monitored using a laser beam which reflects off the back of the cantilever and is detected by a photodiode detector. The photodiode detector consists of four quadrants. The deflection of the cantilever is measured from the differential signal between the top two elements (A) and the bottom two elements (B). A feedback system is used to control the tip-sample interactions.

The three primary modes of the AFM are contact mode; non-contact mode; and tapping mode[22]. In contact mode, the tip and the sample are in the repulsive regime and make contact through the layer of adsorbed water from the surrounding atmosphere on the sample surface. As tip moves across the surface, the cantilever deflection is monitored by the photodiode detector. The feedback loop maintains a constant cantilever deflection by vary the height of the piezoelectric and moving the sample up and down in the z-direction. The vertical movements of the piezoelectric scanner are recorded by the computer to give a topological image of the sample. The advantages of contact mode are high scanning speeds and the ability to obtain atomic resolution images. However, the large lateral forces caused by 'dragging' the tip across the sample surface can distort the images and damage soft surfaces.

In non-contact mode, the cantilever oscillates at a frequency that is slightly higher than the cantilever's resonant frequency with amplitude of less than 10 nm. This results in an AC output from the photodiode detector. When the tip comes close to the sample surface (without actually touching it), van der Waals forces decrease the amplitude of oscillation and change its resonant frequency. The feedback loop maintains the amplitude of oscillation and frequency by varying the height of the sample as the tip scans the surface of the sample. Again, this vertical movement is recorded by the computer, giving topological information about the sample surface. The advantage of non-contact AFM is that no force is exerted on the sample. However, this is offset by lower lateral resolution and slow scan speeds. In addition to this, non-

contact AFM can only be used on extremely hydrophobic samples where there is only a very thin layer of adsorbed water.

In tapping mode, the cantilever oscillates at or near its resonant frequency with amplitudes ranging between 20 nm and 100 nm. The tip moves over the surface, gently tapping it. The greater amplitude of oscillation allows the tip to make contact with the sample through the adsorbed layer of water but prevents it from becoming stuck. The feedback loop maintains a constant amplitude of oscillation by moving the sample up and down in the z-direction with the piezoelectric column. Once again the movements of the piezoelectric column are recorded by the computer, giving topological information about the surface of the sample. Tapping mode AFM gives high lateral resolution images while decreasing the forces normal to the sample and virtually eliminating lateral forces, however it is slightly slower than the contact mode AFM.

The feedback system is optimised by adjusting the gains in the feedback circuit[23]. The target state (eg. amplitude of oscillation in tapping mode) is defined by a user-specified amplitude set-point. The integral gain is used to correct the cumulative error between the system and its target state, while the proportional gain adjusts the system by an amount proportional to the error. If the gains are too high, the feedback loop will overcorrect for the error, leading to feedback oscillations and producing very noisy images. Equally, if the gains are too low the error correction will be sluggish and the piezoelectric column will adjust the height of the sample too slowly, giving inaccurate topographical information. Consequently, it is necessary to set the gains at the maximum possible level without introducing feedback oscillation.

All AFM analysis in this work was carried out using a multimode Nanoscope III atomic force microscope (AFM) in tapping mode. POINTPROBE silicon cantilevers (typical tip diameter D_{Tip}~80 nm) were used throughout. The large size of the AFM tip in comparison to the diameter of a nanotube introduces significant tip effects in lateral measurement, making the nanotubes appear considerably larger in the x-y plane than in reality. Consequently, all diameters were established by measuring their heights (z-direction).

3-2-5 Transmission Electron Microscopy

The transmission electron microscope (TEM) is very similar to the common microscope, with one major difference — it uses an electron beam instead of light to illuminate the sample. The advantage of this is that electrons have a shorter wavelength than light, giving better resolution and magnification.

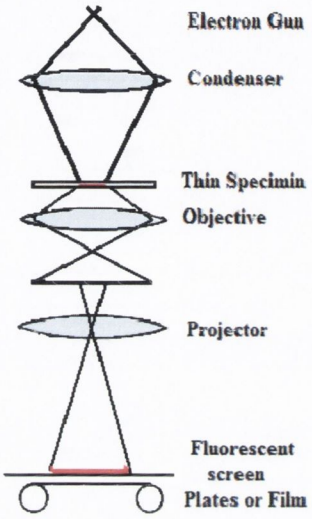


Figure 3-4 The main components of a TEM

The main components of a TEM are shown in schematically Figure 3-4. The electron gun generates a source of radiation, which is focused into a coherent beam and then passed through an extremely thin sample. A series of electromagnetic lenses and apertures are necessary to form a coherent, symmetrical beam that is as free from aberrations as possible. An image forms on the fluorescent screen, which is then recorded on photographic paper or with a CCD camera which is linked to a computer.

Three main imaging methods exist for the TEM: Bright Field, Dark Field and High Resolution. An objective aperture is required for both bright field and dark field modes. The objective aperture is a metal plate with holes punched in it, which is inserted just below the objective lens. The function of the objective aperture is to allow either the transmitted electron beam (bright field) or the diffracted electron beam (dark field) to form the image (Figure 3-5). In bright field mode, the incident electron beam is transmitted through the sample, allowing some of the electrons pass directly through while others undergo slight inelastic scattering. Contrast in an image is created by

differences in scattering in different areas of the sample. Dark field imaging is used for crystalline samples, where the electron beam is elastically scattered, producing a many diffracted beams. A dark field image is formed when one of these diffracted beams is allowed to pass through the objective aperture. In high resolution TEM (HRTEM), a larger objective aperture (or no aperture) is usually used, allowing an image to be formed by the interference of many diffracted beams which reflects the atomic structure of the sample. HRTEM images were recorded by Dr. Valeria Nicolosi using a FEI Tecnai F20 HRTEM and a JEOL 400F HRTEM.

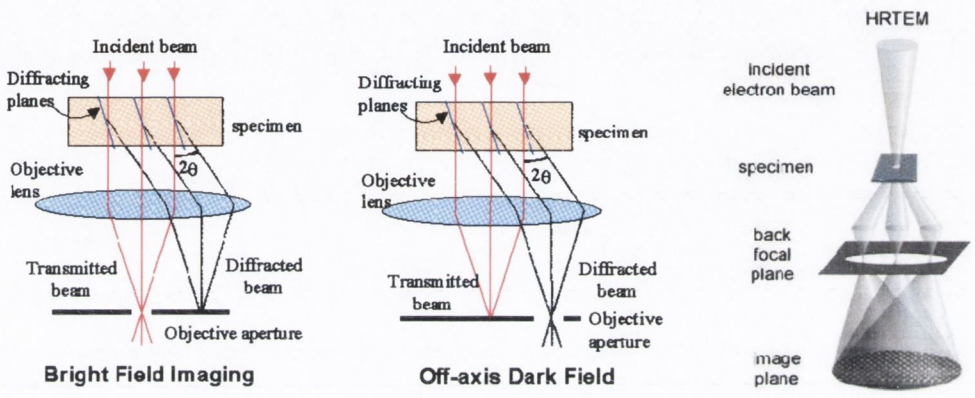


Figure 3-5[24] (Left) Bright-field Setup, (Centre) Dark-field setup, (Right) schematic of HR TEM

3-3 References

1. Nikolaev, P. et al. Gas-phase catalytic growth of single-walled carbon nanotubes from carbon monoxide. Chemical Physics Letters 313, 91-7 (1999).
2. www.cnanotech.com
3. Herring Sperm DNA purchased from Sigma Aldrich. Product number: D3159
4. Salmon Testes DNA purchased from Sigma Aldrich. Product number: D1626
5. Calf Thymus DNA purchased from Sigma Aldrich. Product number: D1501
6. PolyA, purchased from Amersham Bioscience. Product number: 27-4110-01
7. Purchased from Sigma Genosys
8. Deuterium Oxide, 99.9 atom % D. Purchased from Sigma Aldrich. Product number:151882
9. Softley, T. P. Atomic Spectra (Oxford University Press, New York, 1994).
10. Fox, M. Optical Properties of Solids (Oxford University Press, Oxford, 2001).
11. Winter, M. J. Chemical Bonding (Oxford University Press, New York, 1994).
12. Atkins, P. W. Physical Chemistry (Oxford University Press, Oxford, 1986).
13. Bloomfield, V. A., Crothers, D. M. & Tinoco, I. Nucleic Acids: Structures, Properties and Functions (University Science Books, California, 2000).
14. O'Connell, M. J. et al. Band gap fluorescence from individual single-walled carbon nanotubes Science 297, 593-596 (2002).
15. Weisman, R. B., Bachilo, S. M. & Tsyboulski, D. Fluorescence spectroscopy of single-walled carbon nanotubes in aqueous suspension Applied Physics A (Materials Science Processing) A78, 1111-16 (2004).
16. Bachilo, S. M. et al. Structure-assigned optical spectra of single-walled carbon nanotubes Science 298, 2361-6 (2002).
17. Choi, J. H. & Strano, M. S. Solvatochromism in single-walled carbon nanotubes. Applied Physics Letters 90, 223114 (2007).
18. Chou, S. G. et al. Optical characterization of DNA-wrapped carbon nanotube hybrids Chemical Physics Letters 397, 296-301 (2004).
19. Okazaki, T. et al. Photoluminescence mapping of "as-grown" single-walled carbon nanotubes: A comparison with micelle-encapsulated nanotube solutions. Nano Letters 5, 2618-2623 (2005).
20. Htoon, H., O'Connell, M. J., Cox, P. J., Doorn, S. K. & Klimov, V. I. Low temperature emission spectra of individual single-walled carbon nanotubes: multiplicity of subspecies within single-species nanotube ensembles. Physical Review Letters 93, 027401-1 (2004).
21. Rickard, D., Giordani, S., Blau, W. J. & Coleman, J. N. Quantifying the contributions of inner-filter, re-absorption and aggregation effects in the photoluminescence of high-concentration conjugated polymer solutions. Journal of Luminescence In Press, Corrected Proof.
22. Inc., D. I. Digital Instruments Multimode SPM Instruction Manual (1998).
23. Morris, V. J., Kirby, A. R. & Gunning, A. P. Atomic Force Micrscopy for Biologists (Imperial College Press, London, 1999).
24. www.mse.arizona.edu

Chapter 4

Optimising Sample Preparation

4-1 Introduction

The first objective of this work was to carry out a systematic study of the factors controlling the quality of the DNA-SWNT dispersions. The aim was to optimise all parameters in order to obtain a reliable method of preparing high quality, homogeneous, reproducible dispersions. It quickly became obvious that this would be far more complex than initially anticipated. Numerous different factors were investigated. These included:

- Optimising the sonication process
- Comparing different DNA:SWNT ratios
- Considering different types of DNA
- Exploring the use of mild centrifugation to remove large aggregates and insoluble material from the samples.

4-2 Results

4-2-1 Sonication — Temperature, Vessel Shape & Position

It was found that optimising the sonication process was absolutely critical to the preparation of high quality dispersions. All samples were sonicated in a Branson 1510 sonic bath. Early on, it was noticed that the water temperature of the sonic bath had a significant effect on the quality of the dispersions. This was not unexpected as in other reported work, DNA-SWNT dispersions are generally prepared by sonicating at low temperatures in an ice-water bath[1-7]. To investigate the optimum sonication temperature for our dispersions, three separate samples were prepared by placing DNA stock solution, SWNTs and Millipore water together in a vessel and sonicating them at temperatures of 40 °C and 20 °C and in ice-water. After one hour's sonication, visible agglomerates of nanotubes were observed in the two higher temperature samples,

while a translucent, black dispersion, with no visible agglomerates was obtained from the ice-water sonication. Consequently, all subsequent dispersions were sonicated in an ice-water sonic bath where the water temperature was maintained at <8°C by adding ice regularly. In contrast to other reported work[8, 9], it was found that it was unnecessary to denature the double-stranded DNA (ds-DNA) before sonication. Thus, nanotube dispersion were achieved by sonicating ds-DNA and SWNTs together in water. Both the binding mechanism of ds-DNA and nanotubes and the temperature dependence of sonication are discussed further in Chapter 6. Interestingly, it was found that once the DNA-SWNT dispersions had been sonicated in ice-water for ~2 hrs, they could be heated to >85°C while remaining stable.

The next matter to be investigated was the effect of the shape of the vessel[10] and its position in the sonic bath on the samples. It was found that the sonication intensity was dependent on the volume of ice in the bath and varied immensely in different areas of the sonic bath. It was observed that the most vigorous agitation occurred when the vessel was suspended centrally, at a depth of 5–10mm, allowing a standing wave to form in the bath. A number of different vessels, both plastic and glass, with a variety of shapes were investigated to ascertain the effect of vessel shape on dispersion quality. It was found that better dispersions were obtained when glass vessels with curved bases were used[10]. In particular, the best results were achieved using small round bottom flasks which were less than half-full.

The immersion depth of the round bottom flask had a critical effect on the sonication of its contents. When the flask was immersed deeply in the bath, the nanotube pellets disintegrated into a fine powder, but did not disperse throughout the liquid. The exact depth at which this occurred varied, depending on the volume of ice and the depth of water in the bath. Once the nanotube pellets had fully disintegrated, the flask was raised to a slightly higher position, allowing the nanotube powder to disperse throughout the liquid. However, it should be noted that once the vessel was placed in the raised position, any remaining lumps of nanotubes tended to 'bob about' in the liquid, rather than breaking up and dispersing throughout the liquid. Thus it was necessary to ensure that the nanotube pellet fully disintegrated before raising the round bottom flask. It was thought that crushing the nanotube pellets into a powder with a pestle and mortar might improve the sonication process. However, it was found that

the nanotube powder tended to float on the surface of the water rather than dispersing throughout the liquid. Finally, it was discovered that the nanotube pellets would only break up when placed in small volumes of liquid. Consequently, for the first 2 minutes, only the DNA stock solution and the SWNTs were sonicated. Water was then added in 0.5mL volumes every two minutes until the dispersion reached the required concentration.

4-2-2 High Powered Sonic Tip

The next matter to be considered was the role of high powered sonication in sample preparation. In general, when preparing SWNT dispersions, it is considered necessary to sonicate with a high-powered sonic tip in order to disrupt the van der Waals forces between adjacent nanotubes, allowing the nanotubes to be dispersed[11-16]. To explore the effect of high powered sonication on the DNA-SWNT dispersions, a sample was prepared at a concentration of 0.05 mg/mL, with a ratio of 1:1. The sample was sonicated in an ice-water sonic bath for a total of 2 hrs, before being diluted by a factor of 10 and sonicated for a further 60min. The final 0.005 mg/mL sample was divided between six sample bottles and sonicated with a sonic tip (120W, 60kHz) for a variety of times, ranging from 30 s to 540 s. Each sample bottle was placed in a beaker of ice-water during sonication to prevent heating in the sample. UV-VIS absorption spectra were recorded immediately after sonication, and again after 24 hrs and 96 hrs hours. The absorbance spectra recorded immediately after sonication are shown in Figure 4-1.

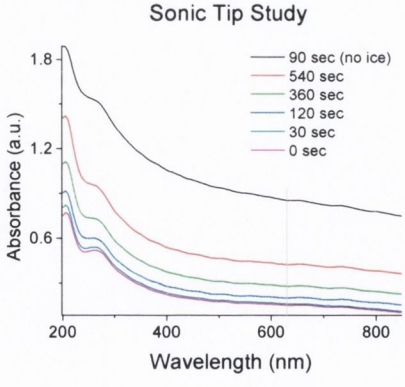


Figure 4-1 Absorption Spectra for DNA-SWNT samples, sonicated for various times using high powered Sonic Tip

It is clear that high-powered sonication increases the background absorbance level of the sample. To obtain a clearer view of the changes, the absorbance values at 630 nm (shown by the vertical grey line) are shown in Figure 4-2 as a function of sonication time.

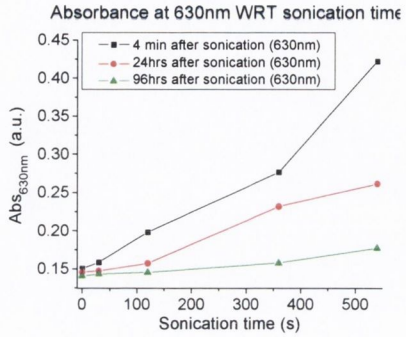


Figure 4-2 Absorbance values at 630 nm as a function of sonication time.

It was found that the background absorbance grew as the sonication times increased, as shown by the black trace. The red and green traces show the absorbance at 630 nm as recorded after 24 hrs and 96 hrs respectively. In both cases the absorbance was found to increase with sonication time; however the magnitude of the increase reduced over time. This reduction in background absorbance coincided with the appearance of a black nanotube sediment at the bottom of each sample bottle. Visually, there appeared to be greater quantities of sediment in the samples that had been sonicated for longer. No sediment was observed in the unsonicated sample.

For completeness, a herring-sperm DNA solution (concentration 0.05 mg/mL) was sonicated with the sonic tip in ice-water for times ranging from 30 s to 540 s. No significant changes in the absorption spectra were observed over this timescale (Figure 4-3).

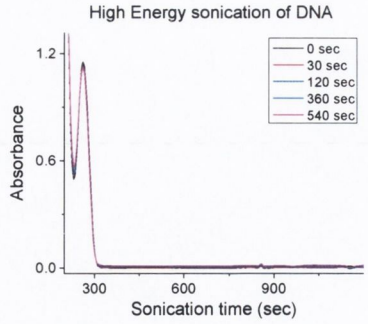


Figure 4-3 Absorption Spectra for a 0.05 mg/mL DNA solution, sonicated for various different times with the sonic tip.

As discussed in Chapter 3, the Beer-Lambert Law states that:

$$A = \varepsilon.C.l$$

where A is absorbance, ε is the extinction coefficient, C is the concentration and *l* is the cuvette pathlength. Given that the concentrations of the DNA-SWNT samples do not change during sonication, it must be concluded that the sonic tip causes changes in the samples that increases the extinction coefficient. Over the 96 hrs following sonication, the samples became unstable causing nanotube sedimentation. It was not possible to calculate the concentration after sedimentation because it is not known if the extinction coefficient changes further during this time. It is clear that the extinction coefficient does not revert to its original value, because, in spite of the sedimentation, the absorbance in the sonicated samples remained greater than that of the unsonicated sample. However, regardless of any changes in extinction coefficient, it was clear that high energy sonication produces unstable dispersions.

Two possible explanations for the observed changes in the DNA-SWNT dispersion stability were considered. Firstly, it was thought that the high power sonication might increase the level of debundling, thus increasing the exposed nanotube surface area. Consequently, it was suggested that the greater quantities of DNA might be needed to interact with the increased surface area. The experiment was repeated at a ratio of 5:1, but, again, sedimentation occurred after sonication with the sonic tip. Secondly it was suggested that, in spite of the ice-water, there was insufficient cooling in the sample and so, localised heat effects might produce unstable samples. Thus, 3 mL of the original 1:1 sample was sonicated for 90s without ice-water cooling. The absorption spectrum is shown in Figure 4-1. The sample had a disproportionately high background absorbance and, again, nanotube sedimentation was observed over the following 96 hrs. It was thus concluded that heating effects were causing the dispersions to become unstable. This is not unexpected, given that low-energy sonication (sonic bath) is only effective at low temperatures.

Based on this set of experiments, it was concluded that there was no long term advantage from high-powered sonication, and so, all subsequent dispersions were prepared using only the sonic bath.

4-2-3 Sonication Time

The next issue to be considered was the optimum sonication time for the sonic bath. A DNA-SWNT sample was prepared at a concentration of 0.01 mg/mL using herring sperm DNA at a ratio of 2:1. The sample was sonicated in an ice-sonic bath for one hour, after which 1mL was removed every half hour for the following 2 hours, yielding a set of samples with sonication times ranging from 1–3 hrs. UV-VIS absorption spectra were recorded for all samples and are shown in Figure 4-4 (A). It was found that the absorbance increased slightly with increased sonication time.

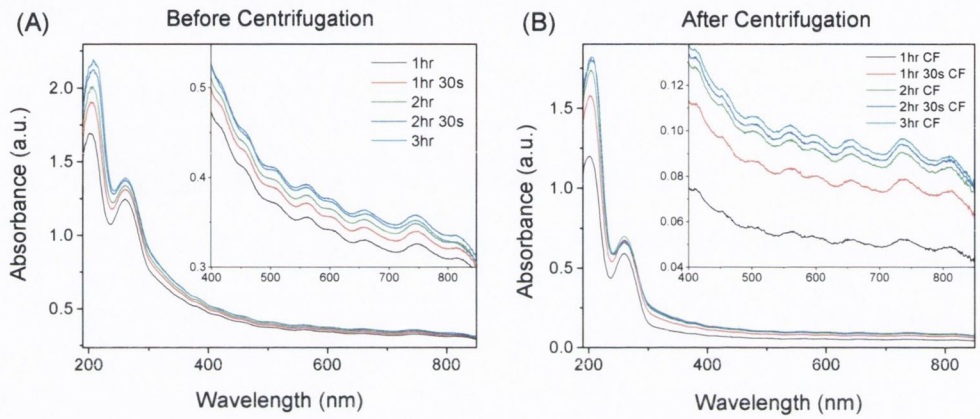


Figure 4-4 Absorbance Spectra for Samples which have been sonicated in the sonic bath for various different times, before (A) and after (B) centrifugation at 13,200 rpm

Next, the samples were centrifuged at 16,000g using an Eppendorf 5415D Centrifuge, before recording the absorption spectra again. The results are shown in Figure 4-4 (B). Centrifugation removes all bundles with sizes above a certain cut off point (the size of this cut-off point depends on both the centripetal force applied and the duration of centrifugation). The sample with the greatest number of nanotube bundles with sizes below this cut-off point will have the maximum concentration after centrifugation. The sample concentrations after centrifugation were determined using the Beer Lambert Law, and are shown in Figure 4-5 as a function of sonication time.

A significant increase in the post-centrifuge concentration was observed when the sonication time was increased from 1hr to 2 hrs. However for greater sonication times the increase was found to be very small and within the errors of the

spectrometer. It was decided that this increase was too small to warrant the extra sonication time and so, all subsequent dispersions were sonicated for a total of 2 hrs

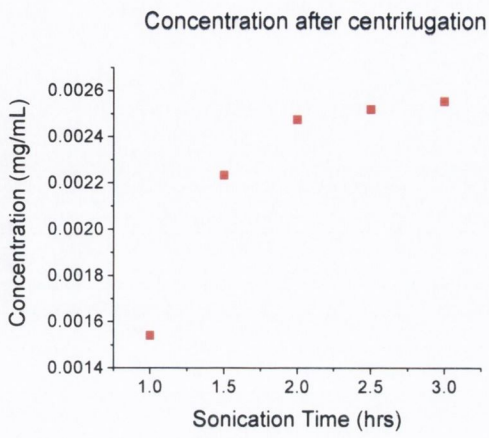


Figure 4-5 Concentration after centrifugation as a function of sonication time.

4-2-4 Ratio of DNA to SWNTs

At the time these experiments were being carried out, there was no consensus in literature on the optimum ratio of DNA to nanotubes for dispersions and a wide variety of ratios, ranging from as high as 8.5:1[3] down to 1:1[1] (DNA:SWNT), were reported. It was therefore decided to carry out a systematic study to determine the optimum DNA:SWNT ratio. This proved to be very challenging due to reproducibility issues between separate samples. As stated earlier, the intensity of sonication varies in different areas of the sonic bath[10] and is dependent on the depth of water, the volume and position of ice in the bath, the depth and position of the round bottomed flask and even the size of the round bottom flask and the volume of its contents. Every effort was made to minimise the effects of these factors, from building custom-made holders which suspended the flask at exactly the same position and depth every time, to attempting to keep the water height and the volume of ice constant. Regardless, it was observed that different samples appeared to be sonicated with different intensities. Eventually it was decided to place the round bottom flask in the position that provided the greatest visual agitation of its contents.

The following experiment was carried out in an attempt to determine the best DNA:SWNT ratio. Two DNA-SWNT dispersions were prepared with concentrations of 0.05 mg/mL and ratios of 1:1 and 3:1, using Herring Sperm DNA. Absorption spectra were recorded using a Cary 300 Scan UV-VIS spectrometer in kinetic mode. Spectra were recorded every 3 hrs for a total of 63 hrs, scanning over a 200 nm to 850 nm wavelength range. Figure 4-6 (A) & (B) show the initial absorbance spectra and the absorbance at 650 nm as a function of time respectively. It was found that the sample with a ratio of 1:1 had a greater absorbance at all wavelength above 300 nm and less sedimentation over the following 63 hrs than the 3:1 sample.

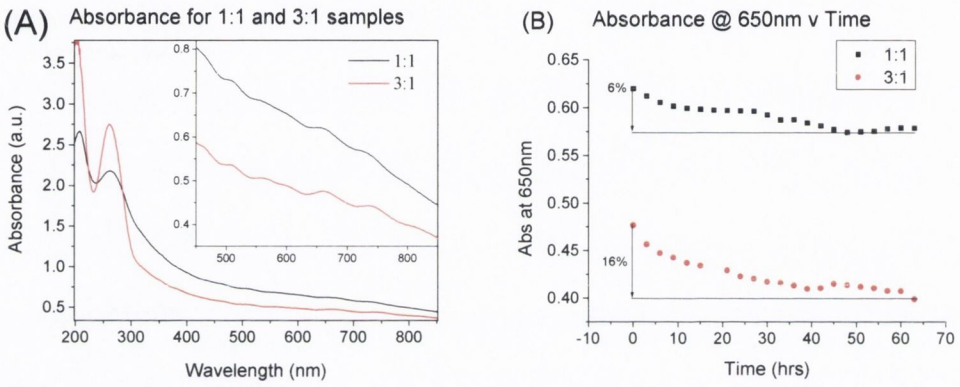


Figure 4-6 (A) Absorption Spectra for two samples prepared with ratios of 1:1 and 3:1. (B) Absorbance at 650 nm of each sample as a function of time after sonication.

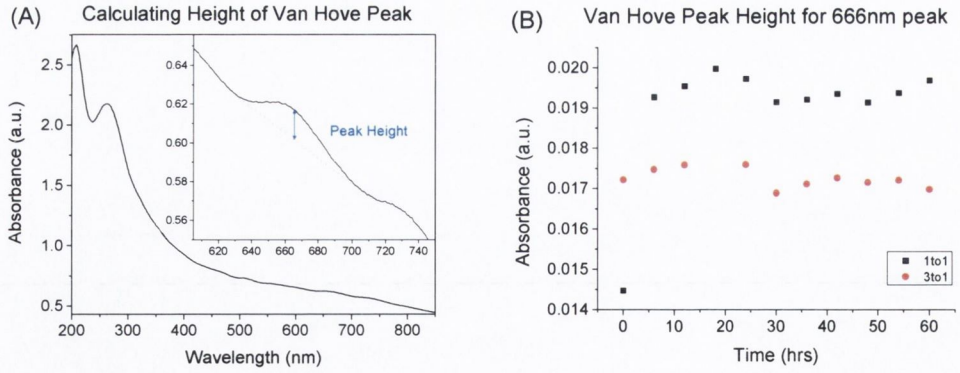


Figure 4-7 (A) Method for calculating the peak heights. The peak height was measured by subtracting a straight line background from the absorption peak and measuring the maximum height after this background has been removed. (B) The peak heights at 666 nm as a function of time for the 1:1 and the 3:1 samples.

The van Hove peak heights at 666 nm were calculated as shown in Figure 4-7 (A), and are shown as a function of time in Figure 4-7 (B). Initially the van Hove peaks were greater in the 3:1 sample. However, the peaks in the 1:1 sample grew considerably in the first 3 hrs, and exceeding that of the 3:1 sample for the remainder of the experiment. On the basis of this experiment, it was thought that a ratio of 1:1 was optimum.

However, when the experiment was repeated for three similar dispersions with ratios of 1:1, 2:1 and 3:1 respectively, different results were obtained. The initial absorbance spectra and the absorbance at 650 nm as a function of time are shown in Figures 4-8 (A) & (B) respectively. In this experiment, it was found that the absorbance was greatest in the 3:1 and the 2:1 samples, while the 1:1 sample had slightly lower values. The peak height was greatest in the 1:1 sample, but a greater increase was observed in the 2:1 and 3:1 samples as shown in Figure 4-8 (C).

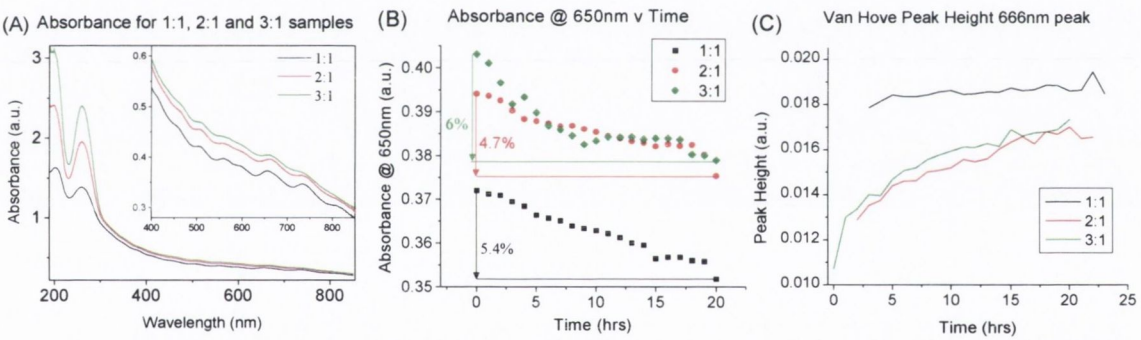


Figure 4-8 (A) Absorption Spectra for three samples with ratios of 1:1, 2:1 and 3:1. (B) Absorbance at 650 nm as a function of time for the three samples. (C) Van Hove Peak heights as a function of time.

This experiment was repeated a number of times without obtaining repeatable results. In addition, the reasons for the differences in the magnitude of absorbance in different samples were unclear. The temperature of the samples was maintained at <8° throughout sonication making it unlikely that heating effects were the responisble for the inconclusive results. Later concentration studies (Chapter 5) found that, for dispersions prepared with natural DNA, the extinction coefficient is relatively

insensitive to the size of the nanotube bundles[17] and therefore it is unlikely that the greater absorbance is due to smaller nanotube bundles. It was felt that the most probable cause was differences in the effective concentrations of the samples resulting from the incomplete disintegration of the nanotube pellets during the early stages of sonication.

On a number of occasions, it was found that the nanotubes precipitated out of solution overnight in the samples with ratios of 1:1. Finally it was decided that a ratio of 2:1 would be used for subsequent experiments. It was felt that it was the strength of sonication, rather than the ratio of DNA to SWNTs that was the critical factor in defining the magnitude of absorbance and the sample's stability over time, and that adding extra DNA to the dispersion was of no benefit. It was therefore decided that it would be preferable to use the smallest ratio that reliably produced stable dispersions.

4-2-5 Different Types of DNA

It was decided that it would be preferable to use natural DNA for the majority of the studies in this thesis. Natural DNA is readily available and inexpensive and would enable us to increase our understanding of the DNA-SWNT system before graduating to expensive custom-synthesised oligonucleotides. Three different types of natural DNA were available — herring sperm DNA, salmon testes DNA and calf thymus DNA. To compare the dispersion efficiency of each DNA type, samples were prepared with the three DNAs, each at a concentration of 0.01 mg/mL and a ratio of 2:1. The absorption spectra were recorded immediately after sonication and again 1 month later. The 1 month-old samples were then centrifuged at 16,000g for 1hr to accelerate sedimentation, leaving only the small bundles and individually dispersed nanotubes in solution. The spectra are shown in Figure 4-9.

All three types of DNA produced translucent, black solutions without any visible nanotube agglomerates. All samples were found to be stable, with minimal sedimentation occurring during the first month. Interestingly, a time-dependent increase in the van Hove peak height was again observed over the course of the following month, as shown in Figure 4-10. The largest growth occurred in the sample

prepared with salmon testes DNA. This sample also had the largest van Hove peaks after centrifugation. According to the literature available at the time[18], it was believed that intensity of van Hove absorption peaks was an indication of the size of the nanotube bundles, with smaller bundles producing sharper van Hove peaks. It has since been discovered that there is a time dependent sharpening of the van Hove peaks which is independent of bundle size (Chapter 6).

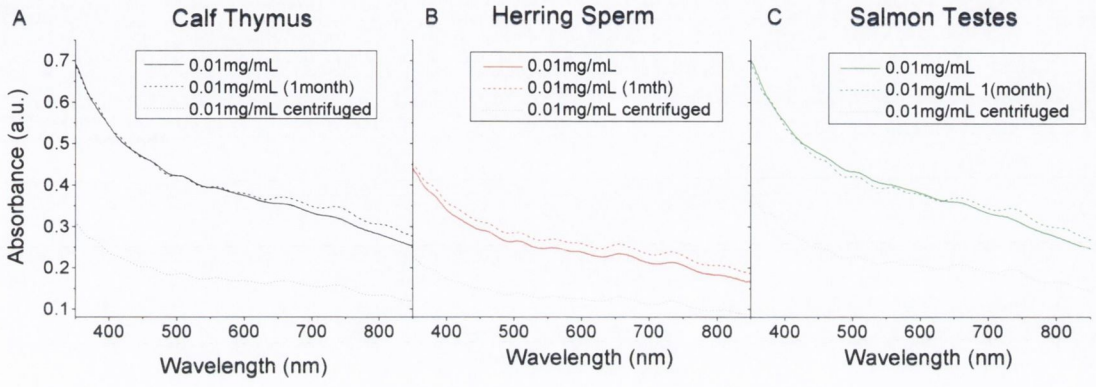


Figure 4-9 Absorption spectra taken immediately after sonication, 1 month after sonication and after centrifugation at 13,2000 rpm are shown for samples dispersed with Calf Thymus DNA (A), Herring Sperm DNA (B) and Salmon Testes DNA (C)

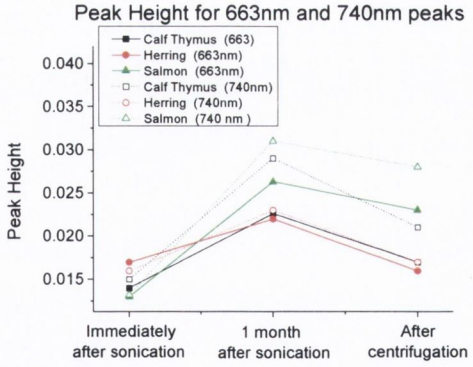


Figure 4-10 Peak heights for the 663 nm and 740 nm peaks for three samples prepared with Calf Thymus, Herring Sperm and Salmon Testes DNAs.

The concentrations after centrifugation were calculated from the change in absorbance at 650nm and were found to be 4.4×10^{-3} mg/mL; 4.7×10^{-3} mg/mL and 5.5×10^{-3} mg/mL for the samples prepared with calf thymus DNA, herring sperm DNA and salmon testes DNA respectively. Centrifugation removes bundles with sizes above some cut-off point. Consequently the samples with the highest concentration after centrifugation must contain the greatest number of small bundles and individual SWNTs. It was therefore concluded that the sample prepared with salmon testes DNA had the smallest bundles in solution after 1 month. Salmon testes DNA was therefore chosen as the dispersant for subsequent experiments, both as a result of its superior dispersion properties and in order to further explore the time dependent increase in the van Hove absorption peaks.

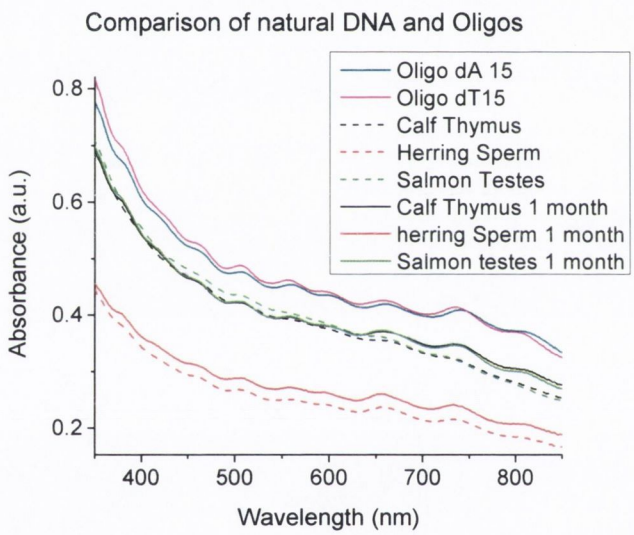


Figure 4-11 Comparison of absorption spectra for samples prepared with natural DNA and custom synthesises oligonucleotides

As a comparison, two samples were prepared using two different oligonucleotides, dA_{15} (15 adenine nucleotides) and dT_{15} (15 thymine nucleotides). Absorption Spectra are shown in Figure 4-11. It was found that both dispersions had well defined van Hove peaks immediately after sonication. These were of similar size to those measured after 1 month in the dispersions prepared with natural DNA. In addition, the van Hove peaks were blue shifted in the dT_{15} sample with respect to the dA_{15} sample. Given that the herring sperm DNA also had reasonably well defined

peaks immediately after sonication, it was suggested that the height of the van Hove absorption peaks may be related to the length of the DNA, with shorter DNA producing sharper van Hove absorption peaks quicker.

4-2-6 Reproducibility

The issue of reproducibility was readdressed with respect to concentration. From separate studies carried out in-house, it was known that the sizes of the nanotube bundles in a dispersion are dependent on the sample concentration[11]. It was thought that if the concentration of the dispersions was dropped sufficiently, then the smaller bundle sizes might reduce the effects of different sonication intensities. A stock solution was prepared at a concentration of 0.1 mg/mL with a ratio of 2:1 and sonicated in an ice-water sonic bath for 2 hrs. The sample was then diluted by a factor of 2 with water and split in two. Each dilution was sonicated separately in the ice bath for 30 mins. A UV-VIS absorption spectrum was taken of each sample and then one of the samples was diluted further by a factor of 2. Again, this dilution was split in two and each half was sonicated separately for another 30 min. This process was repeated for three sets of dilutions, as shown schematically in Figure 4-12.

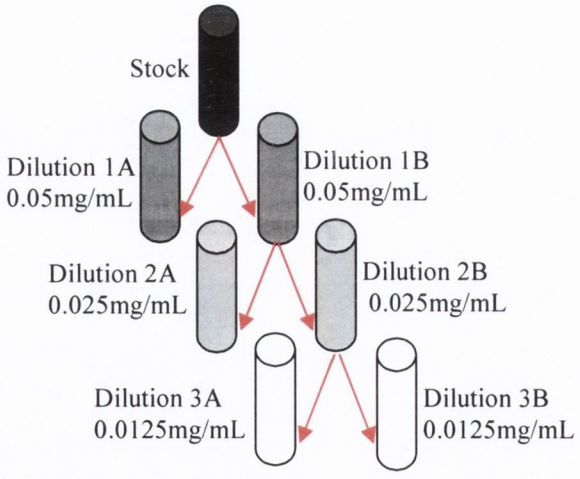


Figure 4-12 Schematic Diagram of the dilution series prepared for reproducibility experiments

The UV-VIS absorption spectra are shown on Figure 4-13 (A). It was found that at each concentration, both samples had absorption spectra that were indistinguishable

within the error of the spectrometer. This would suggest that once the nanotubes are adequately dispersed in a stock solution, any further dilutions have reproducible concentrations and slight differences in the intensity of the sonication have a negligible effect on the samples' optical properties. Thus, within a dilution series all results were deemed to be fully reproducible. This was taken as further evidence that the differences in the magnitude of absorption observed in earlier experiments was due to the incomplete disintegration of the nanotube pellets during the initial stages of sonication, leading to differences in the effective concentration of the dispersions.

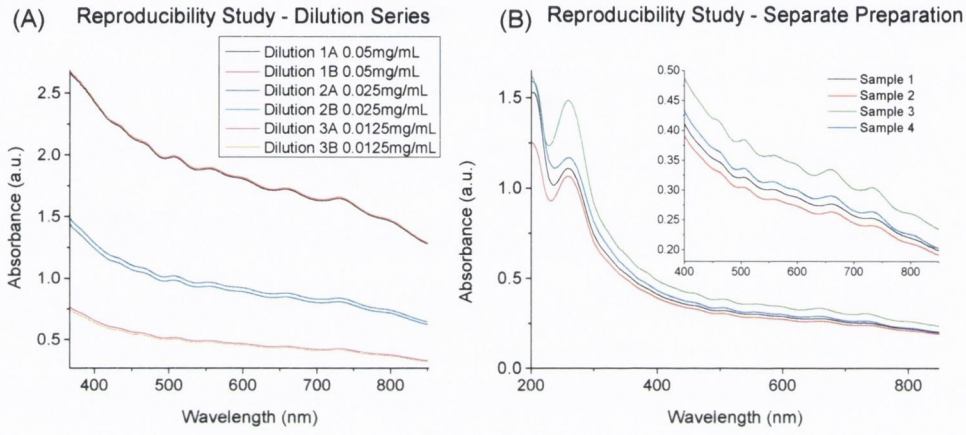


Figure 4-13 (A) Absorption Spectra for samples prepared within a dilution series in order to check reproducibility for samples prepared from the same stock solution. (B) Absorption Spectra for samples prepared and sonicated separately

With this in mind, the issue of reproducibility between separate samples was investigated. Four samples were prepared separately with concentrations of 0.01 mg/mL and ratios of 2:1. In an effort to ensure that the whole nanotube pellet was dispersed in the liquid, the DNA and nanotube were placed together in the round bottom flask and a spatula was used to crush the pellet into as many pieces as possible. The pressure of spatula also forced air bubbles out of the pellets, allowing them to sink to the bottom of the flask where the sonication is most intense. The flask was then immersed deeply in the sonic bath and sonicated until all visible lumps of nanotubes had disintegrated, before raising it in the bath to disperse the nanotubes throughout the liquid. All samples were sonicated for a total of two hours. The absorption spectra are

shown in Figure 4-13 (B). It is clear that there are differences between the spectra, but they were relatively small in comparison to earlier results. If it is assumed the differences in the absorbance of each sample is predominately due to a failure to fully disperse all the nanotubes, then the larger the absorption, the greater the fraction of nanotubes dispersed in the sample and the closer the sample is to its intended concentration. By this logic, sample 3 must be the closest to 0.01 mg/mL, allowing the average error of the other three samples to be calculated as ~16%. It must be stated that the real value is probably slightly greater than this, as we have assumed that the all nanotubes are fully dispersed in Sample 3, which may not be the case and cannot be verified. However, to a first approximation, the errors were found to be reasonably small, showing that we have found a reproducible method of preparing DNA-SWNT dispersions.

4-2-7 Optical Microscopy and Light Centrifugation

A set of 5 samples with concentrations ranging from 0.1 mg/mL to 0.005 mg/mL were prepared and viewed under an optical microscope in order to measure the size of the nanotube aggregates in solution. The samples were observed with a 40× optical lens and were viewed while wet to prevent drying effects altering the results. 10μL of solution was dropped onto a glass slide and covered with a plastic cover slip. This volume was found to be optimum, creating a film of solution that was thin enough to allow all the aggregates to be in focus at the same time. Small aggregates, with diameters of 1–10μm, could be seen floating in all but the least concentrated sample. It is thought that these aggregates are lumps of nanotubes that did not disintegrate during the initial stages of sonication, rather than nanotubes that were dispersed but re-aggregated. These aggregates were removed by lightly centrifuging the samples at 3,300*g* for 1 hr. (This is in contrast to ultracentrifugation where acceleration fields of up to 122,000*g* are employed for up to 4 hrs).

Light centrifugation was carried out on a full concentration range in order to study its effects on different sample concentrations. A stock solution was prepared at 0.3 mg/mL, from which five serial dilution were made, the lowest concentration being

1×10^{-3} mg/mL. Each sample was centrifuged at 3,300g and analysed using UV-VIS-NIR absorption spectroscopy. The results are shown in Figure 4-14 (A), the solid and dotted lines show the samples before and after centrifugation respectively. The percentage loss at each concentration is shown in Figure 4-14 (B). It was found that in each dilution the concentration had decreased by between 5% and 21% after sonication with a mean loss of 15%.

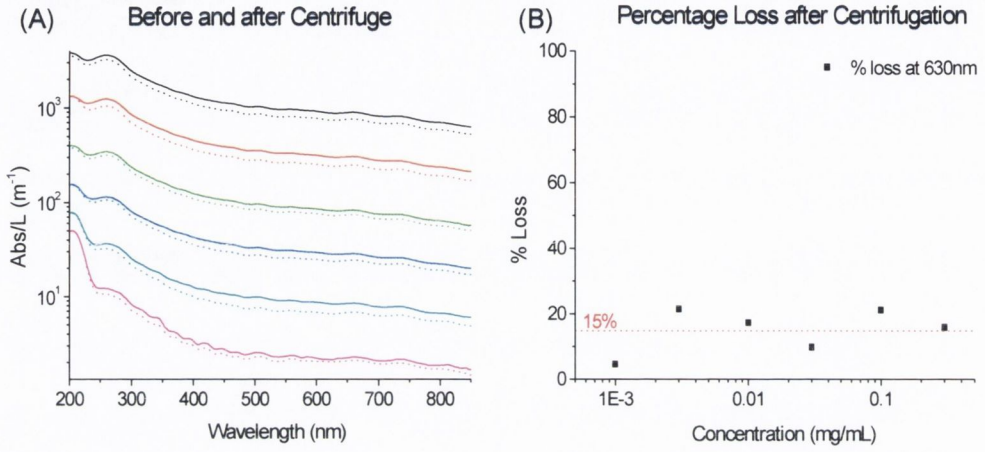


Figure 4-14 (A) The UV-VIS absorbance spectra divided by cuvette length (Abs/L) is shown as a function of wavelength for a range of concentrations. (B) The reduction in concentration is shown as a percentage as a function of concentration. The mean loss is 15%.

4-3 Conclusions

In conclusion, a range of different experiments were carried out in an attempt to find the optimum method of preparing DNA-SWNT dispersions. The following method was found to be the most effective and was used when preparing subsequent dispersions:

Sonicated salmon testes DNA solution (concentration of 1 mg/mL) is added to the SWNT pellets in a round bottomed flask at a ratio of 2:1. The pellet is crushed into small pieces using a spatula. The flask is then immersed deeply in an ice-water sonic bath and sonicated until the pellet has fully disintegrated. The depth of the flask is then adjusted and sonication continues, with water being added in 0.5mL volumes every two minutes until the dispersion reaches the intended concentration. The dispersions are sonicated for a total of 2 hrs, with ice being added to the sonic bath every 20–30 min to prevent the temperature rising above 8°C. The samples are then centrifuged at 3,300g to remove all large aggregates and insoluble material. UV-VIS absorption spectra are recorded before and after centrifugation and are used to calculate the final concentration of the sample.

4-4 References

1. Zheng, M. et al. DNA-assisted dispersion and separation of carbon nanotubes Nature Materials 2, 338-342 (2003).
2. Zheng, M. et al. Structure-based carbon nanotube sorting by sequence-dependent DNA assembly Science 302, 1545-8 (2003).
3. Nakashima, N., Okuzono, S., Murakami, H., Nakai, T. & Yoshikawa, K. DNA Dissolves Single-walled Carbon Nanotubes in Water Chemistry Letters 32, 456 - 457 (2003).
4. Hu, C. et al. DNA functionalized single-walled carbon nanotubes for electrochemical detection. Journal of Physical Chemistry B 109, 20072-20076 (2005).
5. Strano, M. S. et al. Understanding the nature of the DNA-assisted separation of single-walled carbon nanotubes using fluorescence and Raman spectroscopy Nano Letters 4, 543-50 (2004).
6. Arnold, M. S., Stupp, S. I. & Hersam, M. C. Enrichment of single-walled carbon nanotubes by diameter in density gradients Nano Lett. 5, 713-718 (2005).
7. Chen, R. J. & Zhang, Y. Controlled precipitation of solubilized carbon nanotubes by delamination of DNA Journal of Physical Chemistry B 110, 54-57 (2006).
8. Gigliotti, B., Sakizzie, B., Bethune, D. S., Shelby, R. M. & Cha, J. N. Sequence-Independent Helical Wrapping of Single-Walled Carbon Nanotubes by Long Genomic DNA Nano Lett. 6, 159-164 (2006).
9. Badaire, S. et al. Liquid crystals of DNA-stabilized carbon nanotubes. Advanced Materials 17, 1673-1676 (2005).
10. Niyogi, S. et al. Ultrasonic dispersions of single-walled carbon nanotubes Journal of Physical Chemistry B 107, 8799-8804 (2003).
11. Coleman, J. N. et al. Binding kinetics and SWNT bundle dissociation in low concentration polymer-nanotube dispersions Journal of Physical Chemistry B 108, 3446-3450 (2004).
12. Bergin, S. D. et al. Exfoliation in Ecstasy: Liquid crystal formation and concentration dependent debundling observed for single wall nanotubes dispersed in the liquid drug γ-Butyrolactone. Submitted (2007).
13. Ryan, K. P. et al. Carbon nanotube nucleated polymer crystallization. Fullerenes Nanotubes and Carbon Nanostructures 13, 431-434 (2005).
14. Cadek, M. et al. Reinforcement of polymers with carbon nanotubes: the role of nanotube surface area. Nano Letters 4, 353-6 (2004).
15. Murphy, R. et al. High-yield, nondestructive purification and quantification method for multiwalled carbon nanotubes Journal of Physical Chemistry B 106, 3087-91 (2002).
16. Giordani, S. et al. Debundling of single-walled nanotubes by dilution: observation of large populations individual nanotubes in amide solvent dispersions. Journal of Physical Chemistry B 110, 15708-18 (2006).
17. Cathcart, H. et al. Spontaneous Debundling of Single-Walled Carbon Nanotubes in DNA-Based Dispersions. J. Phys. Chem. C 111, 66-74 (2007).
18. O'Connell, M. J. et al. Band gap fluorescence from individual single-walled carbon nanotubes. Science 297, 593-596 (2002).

Chapter 5

Full Concentration Study

5-1 Introduction

The aim of this study was to develop a deeper understanding of the nature of the dispersion of nanotubes using DNA and to explore the effects of concentration on the nanotube bundle sizes. At this point it is worth considering that any as-produced dispersion of SWNTs, in any medium will consist of both individual SWNTs and bundles with a range of sizes[1-3]. More specifically, dispersions are observed to have characteristic bundle diameter distributions[2]. An understanding of the factors influencing the bundle size distribution would allow one to tailor the dispersions such that the bundle size distribution is narrow, with a mean close to the size of an individual nanotube. This would remove the need to ultracentrifuge dispersions to remove bundles, dramatically increasing nanotube yield. In this study, we showed that the primary factor controlling the bundle size distribution in DNA based dispersions is the nanotube concentration.

One result of this would be the development of a cheap, simple and efficient method of producing high quality dispersions of individual SWNTs using DNA as the dispersant. There are two possible ways of maximising efficiency and minimising cost; firstly by using a low cost, natural DNA as the dispersant and secondly by minimising the nanotube wastage during centrifugation. In many of the studies discussed in the literature survey in Chapter 2, expensive, custom synthesised oligonucleotides have been used. While natural DNA has been used, in general this has only been the case when high quality dispersions are not required[4-8]. However, where individually dispersed SWNT are required it has generally been considered necessary to use oligo-nucleotides[9-16]. In addition, in most research on DNA-SWNT dispersions published to

date, ultra-centrifugation has been carried out on the dispersions in order to remove all bundles with size above some cut-off point. A review of the literature suggests that this cut-off point is close to the size of an individual nanotube, resulting in dispersions rich in individual SWNTs[11,16,17]. However the cost of ultra-centrifugation is the loss of as much as 99% of the nanotube mass from the dispersion[17].

5-1-1 Effects of Sonication on the Nanotube Bundles

In this study, all dispersions are sonicated in an ice sonic bath. The input of sonic energy from the sonic bath overcomes the London interactions between the SWNTs, creating a large population of individual SWNTs and small bundles. However, this increase in the number of bundles/nanotubes per unit volume of solution decreases the inter-bundle separation and so increases the probability of re-aggregation. Many more individual SWNTs/small bundles will be produced per unit volume in more concentrated dispersions, resulting in very high probability of re-aggregation. The eventual distribution of bundle diameters within a sample is therefore critically dependent on nanotube concentration, rather than solely on sonication parameters. We suggest that by diluting the dispersions and hence increasing inter-bundle separation, we can push the bundle size distribution towards lower values, thus negating the need for centrifugation.

It should be pointed out that a dispersed equilibrium is not observed for SWNT-water mixtures and therefore the processes described above must be mediated by the presence of the DNA. However, it is not clear how the SWNT-DNA interaction proceeds in the early, non-equilibrium, stages of dispersion formation.

5-1-2 Beneficial Results of the Concentration Study

The results from these experiments showed that the bundle diameter distributions in these dispersions are indeed dependent on the SWNT concentration[1]. Consequently, as the concentration of the SWNT dispersion is reduced, the number of individual nanotubes and very small bundles increases. Systematic concentration studies will

allow us to correlate mean bundle size with concentration, allowing one to make an informed decision when trying to balance the needs for minimum bundle size and maximum concentration. In addition to this, we aim to find the concentration at which all SWNTs are dispersed either individually or in extremely small bundles. Alternatively, if one chooses to centrifuge the dispersion, it would be useful to calculate the nanotube concentration at which the number of individual nanotubes in the dispersion is maximised, allowing one to obtain the greatest number of individual nanotubes from centrifugation. Finally, it has previously been assumed that DNA-nanotube hybrids exist in water as a dispersion rather than as a solution. It was thought that debundling is thermodynamically unfavourable and only occurs with the aid of sonication to break up the bundles. We will investigate the effects of dilution on the bundle diameter distributions in the absence of this sonication.

5-2 Experimental Procedure

Two DNA-SWNT dilution series (0.1 mg/ml – 3.7×10^{-4} mg/ml range) were prepared and analysed using AFM, UV-VIS absorption spectroscopy, sedimentation apparatus and NIR photoluminescence. A stock sample was prepared at 0.1 mg/mL with a ratio of 2:1 using Salmon Testes DNA in Milliopore water using the method described in Section 4-10. From this stock sample, two sets of serial dilutions were made. In order to investigate the effects of sonication on the bundle diameter distribution, in one dilution series each sample was sonicated for 30 min in an ice-water sonic bath before making the next serial dilution; while in the second series, each sample was gently shaken but not sonicated before making the next serial dilution. All samples were left to stand for ~18 hrs before depositing a small volume of each on freshly cleaved mica and allowing the water to evaporate in ambient conditions. The samples were analysed by atomic force microscopy (AFM) in tapping mode. The distribution of diameters at each concentration was established by measuring 200 different bundles from a number of different AFM images taken from different points on the mica (Figure 5-1).

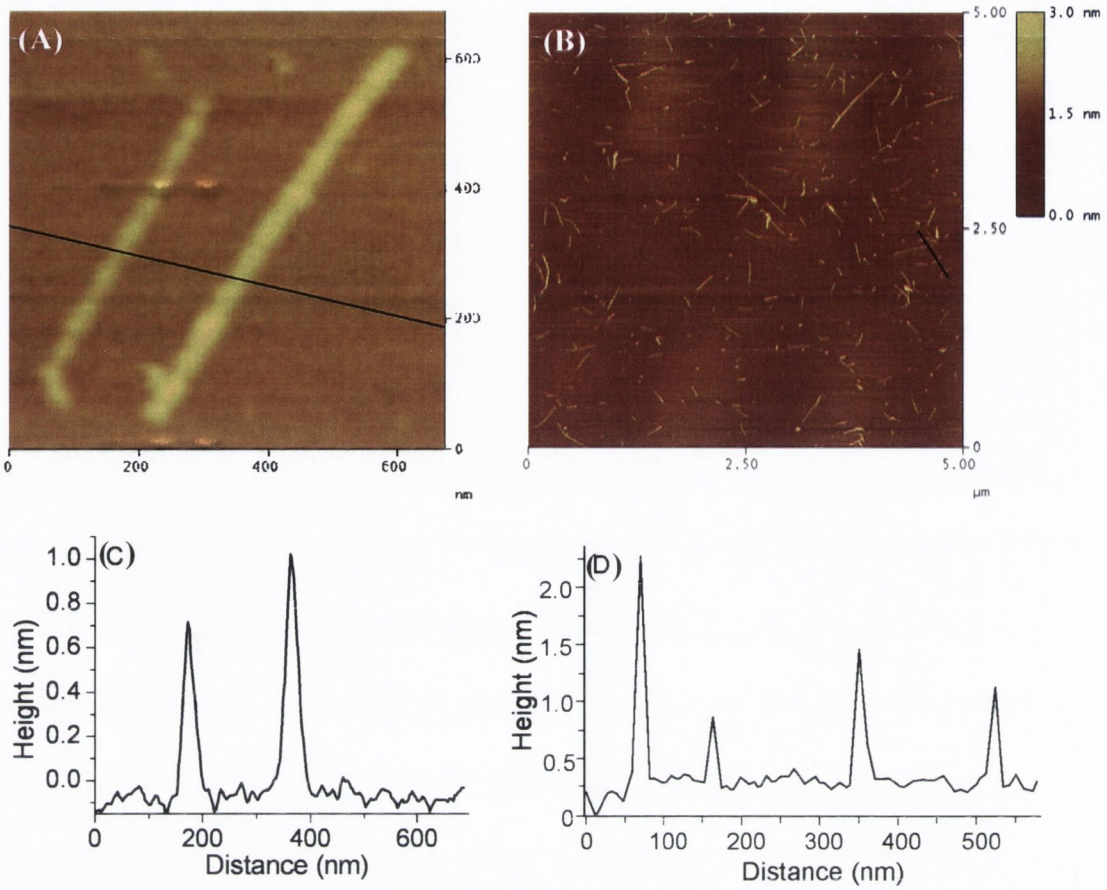


Figure 5-1

(A) An AFM image of two individually dispersed SWNTs. (B) A typical AFM image of a 1×10^{-3} mg/mL dispersion. (C) and (D) show the cross sections of two lines appearing in A and B respectively.

As discussed in Section 4-2-7, each sample was centrifuged at 3,300g to remove the large bundles and insoluble material. UV-VIS-NIR absorption spectra recorded before and after centrifugation showed the concentration to have decreased by 11% –17 % in each sample. Analysis of AFM images showed the bundle diameter distributions to be indistinguishable before and after centrifugation using statistical hypothesis testing (T-test) (Figures 5-3 (B) & (C)). It can therefore be concluded that the centrifugation only removes very large aggregates which were not dispersed during the initial sonication and are too big to be imaged using AFM. Consequently, the

concentration after centrifugation is the true nanotube concentration of the dispersion and is used exclusively from this point.

The long-term stability of the DNA-SWNT dispersions was established using a sedimentation apparatus that was developed in-house by Nicolosi *et. al.* [18]. This apparatus allows one to monitor the changes in the concentration due to sedimentation over time. Infra red photoluminescence measurements were made on dispersions that had been prepared some months previously. No sedimentation or aggregation was observed over this period.

5-3 Results

5-3-1 Dispersion Stability

Once prepared, the dispersions were found to be stable for more than 1 year at room temperature with little or no visible sedimentation. Sedimentation studies were carried out on a dispersion with a concentration of 2.7×10^{-2} mg/mL. This concentration is the most concentrated dispersion at which the transmittance through a 1 cm cuvette was high enough to obtain reliable data.

Figure 5-3 (A) shows the absorbance as a function of time over the 17 days after the initial preparation. The dispersion was extremely stable with less than 4% SWNTs sedimenting over this time. The bundle diameters of 200 nanotubes were measured from AFM images, allowing one to monitor the changes in the bundle sizes within the dispersion over this time (Figures 5-3 (C) & (D)). It was found that the mean diameter had increased slightly from 1.68 nm on Day 0 to 2.05 nm on Day 17. There are two possible reasons for this increase, either slight aggregation is occurring within the dispersion or else the conformation of the adsorbed DNA has reorganised over time to form a more uniform covering. While the wrapping of DNA around the SWNT has been suggested[5,6,11,12,16,19,20], this would be expected to be a slow process. Initially, the DNA is likely to be arranged haphazardly on the surface of the SWNT and so the observed diameters would be dependent on the point along the nanotube at which one measured the diameter, as shown by the arrows in Figure 5-2 (left). Consequently, the

AFM diameters measured at this time would yield average diameters for partially wrapped nanotubes. However, the DNA is thought to slowly wrap around the SWNT, finding its optimum conformation over time and forming a uniform covering on the nanotube. The result of this process would be the expansion of the apparent bundle diameter as measured by AFM, as shown in Figure 5-2 (right).

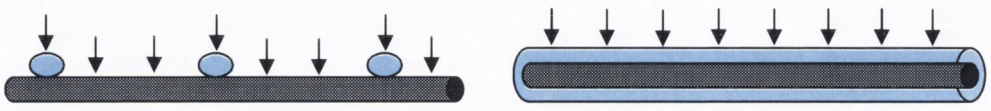


Figure 5-2 Schematic diagram of a partially DNA-covered SWNT (left) and a fully covered SWNT (right). The black arrows show the diameters that would be observed at different points on the DNA-nanotube hybrid.

The diameter distribution of the 2.7×10^{-2} mg/mL dispersion measured on day 17 (Figure 5-3 (D)) is found to be statistically indistinguishable from that measured on day 0, if one allows for the fact that the DNA rearranges itself on the walls of the individual nanotubes ($d\leq1.4$ nm), adding an extra 1 nm to their diameters. This yields diameters that are consistent with the values of 1–2 nm for DNA-SWNT hybrids quoted elsewhere in literature[11]. In reality, the contribution of the DNA to the hybrid diameter may be greater or less than the estimated 1 nm, depending on both the mode of binding and whether the ssDNA binds helically or linearly to the SWNT.

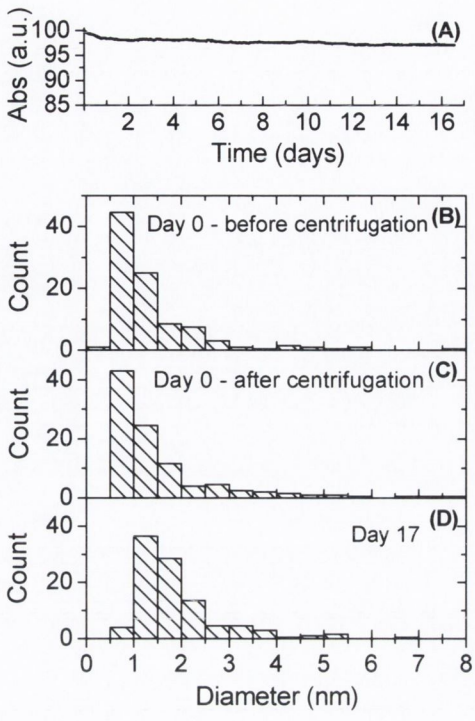


Figure 5-3 (A) The absorbance is shown in as a function of time. The dispersion was extremely stable with less than 4% SWNTs sedimenting over the 17 days after the initial preparation. (B) The bundle diameter distribution of the samples before centrifugation as measured by AFM. (C) The bundle diameter distribution after centrifugation. The distributions (B&C) were found to be indistinguishable using statistical hypothesis testing (T-test), showing that only bundles that are too large to be imaged with AFM are removed from the dispersions. (D) The bundle diameter distribution on day 17. A slight increase in bundle diameters is observed. This is thought to be due to the adsorbed DNA reorganising itself on the walls of the individual SWNT over time to form a more uniform covering. The result of this process would be the expansion of the apparent bundle diameter as measured by AFM. All diameter distributions are normalised to 100 nanotubes.

5-3-2 The effect of concentration on the bundle diameter distribution

The dependence of the bundle diameter on concentration was investigated as described in Section 5-2. Typical AFM images for three different concentrations are shown in Figure 5-4. Visually, it is clear that the bundle sizes decrease as the concentration is reduced.

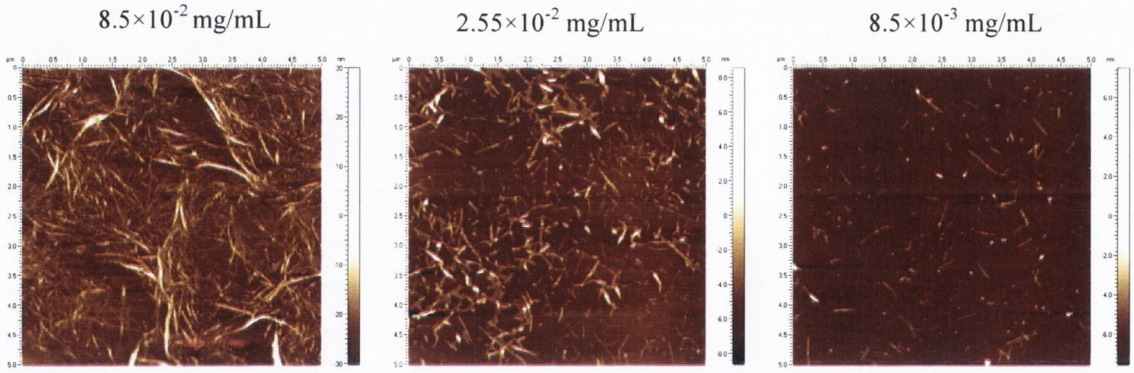


Figure 5-4 Typical AFM images for three concentrations. Each image is 5μm×5um. The diameter distributions are shown in Fig. 22

The diameters of 200 nanotubes were measured from a number of AFM images at each concentration in order to obtain statistics on the bundle diameter distributions. Figure 5-5 shows the diameter distributions for the sonicated dilution series. It can clearly be seen that both the mean bundle diameter and the distribution width decrease with decreasing concentration. Furthermore, at low concentration the distribution converges on a population of individually dispersed SWNTs. This clearly demonstrates that the bundle diameter distribution is dependent on concentration of the sample.

Figure 5-6 shows the mean bundle diameter as a function of concentration. For the sonicated dispersions, the mean diameter decreases linearly before saturating at a minimum diameter below concentrations of 0.027 mg/mL. Below this concentration, the diameter distributions within the dilution series are found to be indistinguishable using statistical hypothesis testing (T-test). The sonicated dispersions saturate at mean diameters of 1.65 nm, which roughly corresponds to a bundle containing three small diameter nanotubes (D = 0.7 nm) which has a bundle diameter of 1.61 nm (including a van der Waals distance of 0.35 nm between adjacent tubes) or to one larger nanotube, each with associated solubilising DNA. A bundle of seven small nanotubes has a diameter of 2.5 nm, which is greater than the measured mean diameter.

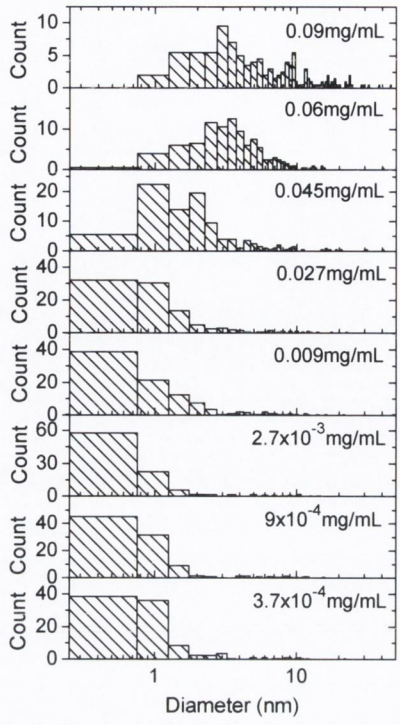


Figure 5-5 Histograms of bundle diameters for DNA-dispersed SWNTs (normalised to 100 nanotubes) over a number of concentrations, ranging from 0.09 mg/mL to 3.7×10^{-4} mg/ml. It was found that both the bundle diameters and the distribution width decrease with decreasing concentration. Furthermore, at low concentration the distribution converges on a population of individually dispersed SWNTs.

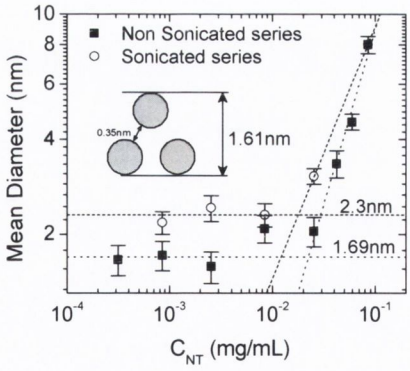


Figure 5-6 Mean bundle diameter as a function of concentration as obtained from the diameter distributions are shown for both the sonicated and the unsonicated dilution series. The error bars are calculated from the standard error of the distribution. In both cases, the mean bundle diameter decreases linearly with decreasing concentration, before saturating at approximately at 1.69 nm and 2.3 nm in the sonicated and unsonicated series respectively.

5-3-3 Dispersion or Solution?

Initially it was considered necessary to sonicate the dispersions between each dilution to facilitate the break up of the nanotube bundles. In order to confirm the role of sonication on the debundling process a second dilution series was prepared without additional sonication between dilutions. It was expected that no debundling would be observed in this dilution series. Surprisingly, it was found that the bundle diameter distribution still decreased with decreasing concentration. The mean diameters for the unsonicated dilution series are also shown in Figure 5-6. It can be seen that the mean diameter decreases linearly before saturating at a minimum mean diameter of 2.3 nm below concentrations of 0.009 mg/mL. All dilutions were statistically indistinguishable below this concentration.

The observation that the debundling of small bundles and ropes occur spontaneously with decreasing concentration leads to the important conclusion that we have a *DNA-SWNT solution rather than a dispersion.* This is a very surprising and exciting discovery. It implies that when the nanotube concentration is reduced, it is thermodynamically favourable for the bundle size distribution to rearrange itself to adapt to the new concentration. For this to occur, it must be possible for individual SWNT to spontaneously desorb from a bundle, diffuse through the solvent before subsequently adsorbing onto another bundle. At equilibrium, the rate of desorption is equal to the rate of adsorption. When the concentration of the dispersion is decreased, the mean distance between the bundles increases, and thus the time taken by a nanotube to diffuse through the solution and adsorb onto a new bundle also increases. However, because the bundles' immediate surroundings remain unchanged, the kinetics governing the desorption process are unaffected and so the adsorption rate falls below the desorption rate and large numbers of smaller bundles are created. However, as the number of bundles increases, the distance between the nanotube centres reduces, until the rate of adsorption and the rate of desorption become equal again. In this way, a new dynamic equilibrium is reached which is appropriate to the new concentration and is characterised by smaller bundles.

However, we must not lose sight of the fact that this process requires the presence of the DNA to act as a dispersant. In order to allow desorption of individual

nanotubes from the bundle, the DNA cannot be wrapped tightly around the bundle. On the other hand, the DNA must coat the nanotube completely enough to shield it from the water. This means that, at least in the non-equilibrium stage, the DNA must coat the nanotube in a way that allows significant DNA mobility.

In order for debundling to occur, the interaction energy between the DNA and the SWNTs must be comparable to the binding energy between two nanotubes. The free energy of binding for DNA and SWNTs was calculated by Zheng for different nucleotides and was found to be comparable to the free energy of association of two nanotubes[11]. This effect is enhanced by the presence of an electrostatic repulsive force between the strands of DNA attached to the nanotubes, overcoming the attractive London interactions between the SWNTs, and making it thermodynamically favourable for the SWNTs to debundle.

5-3-4 Number density and absolute number of individual SWNTs

From the diameter distributions, it is possible to estimate the number density and the mass fraction of individual nanotubes in our samples. The number density (N_i/N_T) is the fraction of objects that are individual nanotubes, where N_i is the number of individual tubes and N_T is the total number of objects measured. Given that the diameter of HiPCO SWNTs is 0.7–1.4 nm, it has been assumed that anything with a diameter of 1.4 nm or less is an individual SWNT. However, it should be pointed out that we do not take into account the contribution of the DNA coating to diameter, and thus the N_i/N_T values quoted are slightly underestimated. It can clearly be seen that this quantity increases with decreasing concentration reaching a value of approximately 0.83 in sonicated dispersion and 0.6 in the unsonicated dispersion (Figure 5-7 (A)). This compares with number fraction of 0.7 individual nanotubes observed for SWNT dispersed in NMP[2].

These values show that while DNA is capable of debundling SWNTs without the aid of sonication, we obtain greater yields of individual SWNTs when the dispersions are sonicated between dilutions. The data is consistent with the idea that individual nanotubes desorb from bundles, diffuse through the solvent before

adsorbing onto new bundles in a dynamic equilibrium. At lower concentrations, this equilibrium will be characterised by a larger fraction of individual nanotubes.

In addition, it is probable that debundling by DNA in the absence of sonication is a slow process and that the unsonicated dispersions have not yet reached equilibrium. The unsonicated samples are left to stand for ~18 hrs before AFM analysis. It is probable that the N_i/N_T values for the unsonicated samples will approach those for the sonicated samples if given more time to equilibrate.

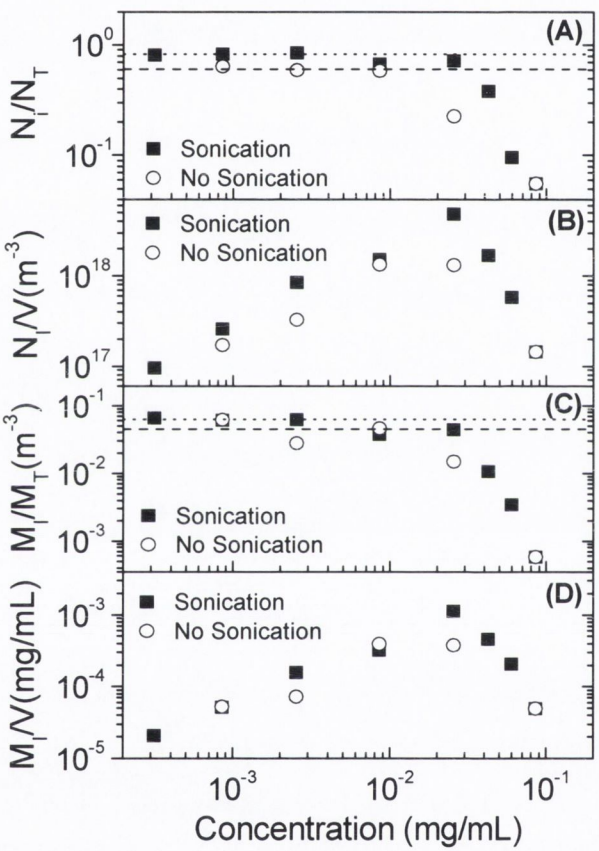


Figure 5-7 (A) Number fraction of individual SWNTs as a function of concentration as obtained from the diameter distributions. It has been assumed that anything with a diameter of 1.4 nm or less is an individual SWNT. This quantity increases with decreasing concentration reaching a value of approximately 83% in sonicated dispersion (dotted line) and 60% in the unsonicated dispersion (dashed line). (B) Number of individual SWNTs per unit volume as a function of concentration. It is clear that the absolute number of individual SWNTs per unit volume of solution is maximised in the region of 2.7×10^{-2} mg/mL. (C) Mass fraction of individual SWNTs. At low concentrations, values of up to 6.2% individual nanotubes in the sonicated dispersions (dotted line) and up to 4.5% individual nanotubes in the unsonicated dispersions (dashed line) are obtained. (D) Partial concentration of individual SWNTs. This value is maximised in the region of 2.7×10^{-2} mg/mL.

The number fraction (N_i/N_T) can be used to calculate the absolute number of individual tubes per unit volume of solution (N_i/V)[2,3], which is calculated as follows:

$$\frac{N_i}{V} = \frac{N_i}{N_T} \times \frac{N_T}{V}$$

where N_i is the number of individual tubes; N_T is the total number of objects measured and V is the volume of solution.

$$\frac{N_T}{V} = \frac{M_T}{\langle M_{NT} \rangle V} = \frac{C_{NT}}{\langle M_{NT} \rangle}$$

where M_T is the total mass of nanotubes; $\langle M_{NT} \rangle$ is the mean mass of one nanotube and C_{NT} is the nanotube concentration (mg/mL).

$$\langle M_{NT} \rangle = \rho_{NT} \langle V_{NT} \rangle = \rho_{NT} \left(\frac{\pi \langle D^2 \rangle L_{bun}}{4} \right)$$

where ρ_{NT} is the nanotube density (taken to be 1500 kg/m^3)[21]; $\langle V_{NT} \rangle$ is the mean volume of one nanotube; $\langle D^2 \rangle$ is the mean square diameter of the bundles and L_{bun} is the bundle length.

giving

$$\frac{N_i}{V} = \frac{N_i}{N_T} \times \frac{4C_{NT}}{\rho_{NT} \pi \langle D^2 \rangle L_{bun}}$$

To a first approximation, L_{bun} is taken to be constant. The values of L_{bun} as a function of concentration are shown in Figure 5-8. The average values were found to be ~260 nm in the sonicated series and ~300 nm in the unsonicated series using AFM. Interestingly, these values are much smaller than those observed for HiPCO SWNTs dispersed in NMP, where individual nanotubes were observed to have lengths of 785 ± 70 nm[22] after 4 hrs in the sonic bath and 4min under a high-powered sonic tip. By comparison, the nanotubes in our dispersions are subjected to much less vigorous sonication, suggesting that the nanotubes must be sheared during sonication as a result of interactions with the DNA, rather than as a result of sonication alone.

The calculated values for N_i/V can be seen in Figure 5-7 (B). It is clear that the absolute number of individual SWNTs per unit volume of solution is maximised in the region of 2.7×10^{-2} mg/mL. This is a surprising result. Instinctively, one might expect

to be able to increase the numbers of individual SWNTs in solution by increasing the concentration of the dispersion, however, this is clearly not the case. Similar results have been observed for SWNT dispersed in N-methyl-pyrrolidone[2] and inorganic nanowires in isopropanol[3]

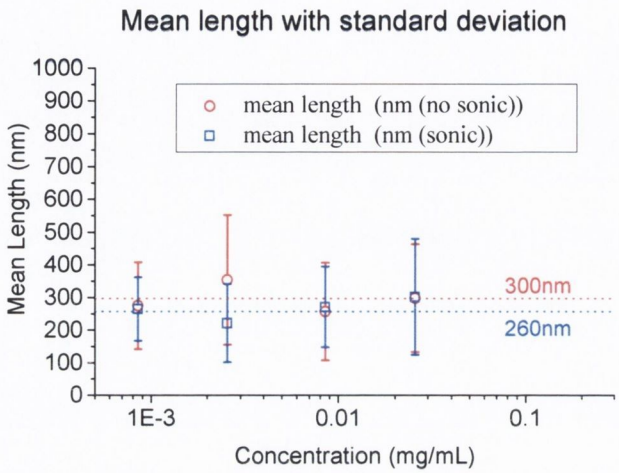


Figure 5-8 Mean length of nanotube bundles as a function of concentration. The error bars are calculated from the standard deviation of the dispersion showing the range of bundle lengths. It was not possible to calculate the mean nanotube lengths at 0.1 mg/mL as overlapping of the nanotubes in the AFM images made it impossible to find the beginning and end of each nanotube.

5-3-5 Mass Fraction & Partial Concentration of Individual Nanotubes

The mass fraction (M_i/M_T) is the fraction of total mass contributed by individual tubes. It allows for the fact that larger bundles contain a greater number of SWNTs, which is not taken into account in the number fraction. It is calculated using the following equation

$$\frac{M_i}{M_T} = \frac{\sum_{D<1.4nm} D^2 L_{ind}}{\sum D^2 L_{bun}} \approx \frac{\sum_{D<1.4nm} D^2}{\sum D^2}$$

where M_i is the total mass of individual nanotubes and M_T is total nanotube mass and L_{ind} and L_{bun} are the mean lengths of an individual nanotube and a nanotube bundle respectively. This calculation makes the approximation that the lengths of the bundles

are similar to those of the nanotubes. This approximation is based on the bundle length distributions as shown in Figure 5-9. It can be seen that the distributions are relatively narrow at every concentration.

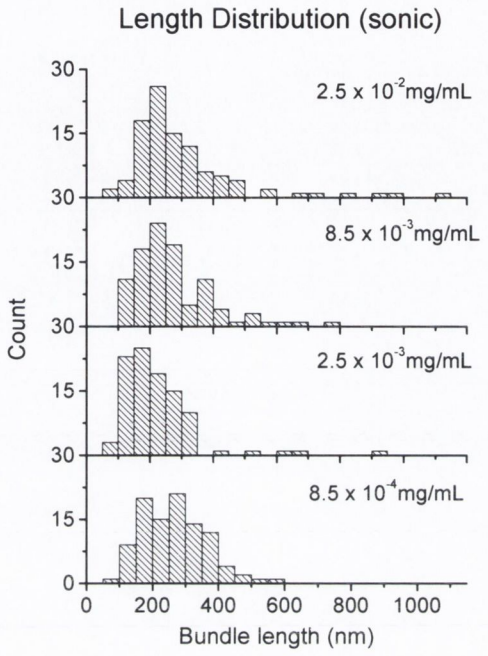


Figure 5-9 Length Distributions for nanotubes and bundles in the sonicated dilution series over a range of concentrations.

It can be seen in Figure 5-7 (C) that at low concentrations we obtain up to 6.2% individual nanotubes by mass in the sonicated dispersions and up to 4.5% individual nanotubes in the unsonicated dispersions.

The partial concentration of individual tubes (M_i/V) can be calculated using the following equation;

$$\frac{M_i}{V} = \frac{M_i}{M_T}\frac{M_T}{V} = \frac{M_i}{M_T}C_{NT}$$

It can be seen in Figure 5-7 (D) that this value is maximised in the region of 0.027 mg/mL, showing this to be the concentration with the greatest partial concentration of individually dispersed SWNT. Clearly this is the optimum concentration for ultra-centrifugation in order to obtain a maximum yield of individual SWNTs.

5-3-6 IR Photoluminescence

We have been able to derive much information about the system from AFM studies of deposited bundles. However, the possibility remains that the concentration dependence of the bundle size distributions is actually dominated by drying effects. In fact, theoretical studies have shown that concentration dependent bundling effects can actually occur for one-dimensional objects that are mobile during drying[23]. In order to rule this possibility out we need an in-situ measurement technique that gives information about either the bundle size distribution or alternatively the population of individual nanotubes. Such a technique is infra-red photoluminescence which is sensitive only to individual nanotubes.

Near infra-red photoluminescence (PL) measurements were made on a number of DNA-SWNT dispersions with a range of concentrations. Shown in Figure 5-10 is a typical photoluminescence map, measured in a dispersion with a concentration C_{NT}=0.01 mg/mL. The PL provides additional strong evidence for the presence of a significant fraction of individual nanotubes in DNA based dispersions, as PL is only observed from individual nanotubes. This is because the PL is almost completely quenched in large bundles of SWNTs due to energy transfer to metallic nanotubes[17].

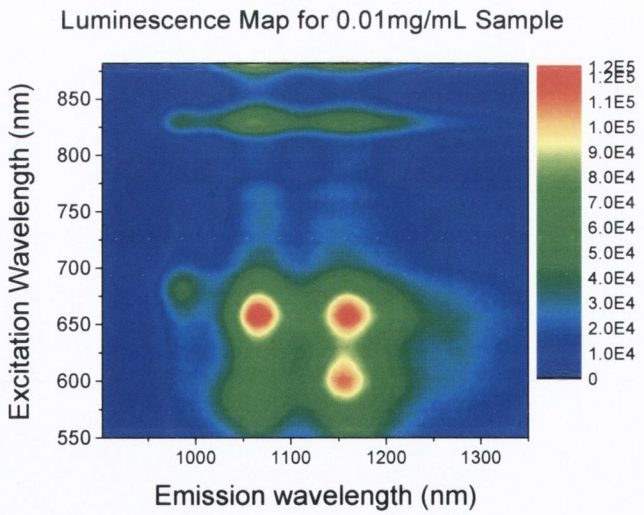


Figure 5-10 Luminescence contour map of Hipco SWNTs dispersed with Salmon Testes DNA in Millipore Water at a concentration of 0.01 mg/mL.

PL emission spectra (excited at 655 nm) are shown in Figure 5-11 as a function of nanotube concentration. The spectral shape is reasonably concentration independent, indicating no changes occur in the populations of individual nanotube types as the overall concentration is changed. The PL intensity increases initially as the concentration is decreased before falling again at lower concentrations. The PL intensity, I_{PL}, of a given peak is proportional to the total number of individual nanotubes involved in that specific optical transition. As the spectral shape is unchanged with concentration, the intensity of the peak at 1042 nm, for example, is proportional to the total number of individual nanotubes in the sample and hence:

$$I_{PL} \propto N_i/V.$$

The fact that the intensity increases initially as the concentration decreases shows clearly that the number of individual nanotubes increases as concentration is lowered even though the total number of nanotubes decreases.

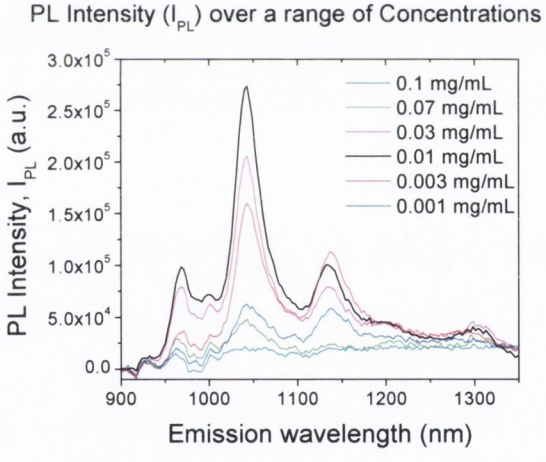


Figure 5-11 Photoluminescence line-spectra, excited at 655 nm for SWNT dispersed in DNA/water at a range of nanotube concentrations.

The intensity of the 1042 nm peak has been plotted in Figure 5-12 (A) as a function of concentration. The AFM data for N_i/V has also been plotted on this graph for comparison. The PL data has been normalised to the AFM data at high concentration.

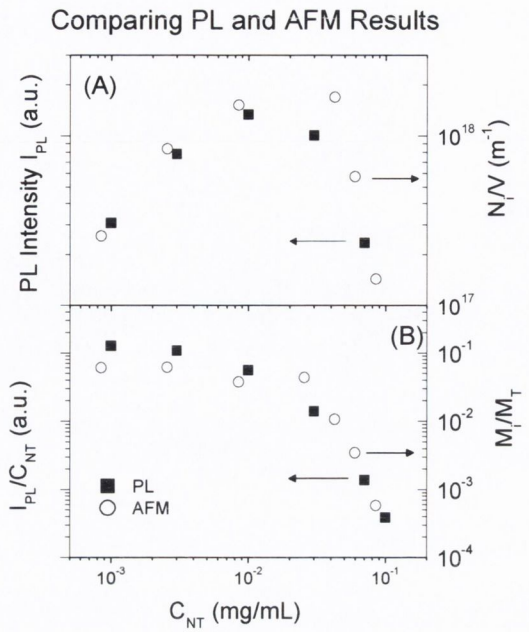


Figure 5-12 (A) The normalised PL intensity is compared to N_i/V, as calculated by AFM, as a function of concentration. (B) The PL intensity divided by nanotube concentration is compared to the mass fraction of individual nanotubes as a function of concentration.

The concentration dependence of the PL intensity matches the AFM data for N_i/V almost perfectly. In addition, the PL intensity can be normalised to concentration and expressed as I_{PL}/C_{NT}. It can be easily shown that this quantity is proportional to the mass fraction of individual nanotubes:

$$I_{PL}/C_{NT} \propto (N_i/V) \times (1/C_{NT})$$

but $$C_{NT} = M_T/V$$

$\rightarrow$ $$I_{PL}/C_{NT} \propto N_i/M_T$$

To a first approximation, all individual nanotubes have similar diameters and lengths:

therefore $$N_i \propto M_i$$

giving $$I_{PL}/C_{NT} \propto M_i/M_T$$

The concentration normalised PL intensity has been plotted on Figure 5-12 (B). Again its concentration dependence matches very well to the AFM data for M_i/M_T which has also been plotted for comparison. This shows categorically that the statistical data for populations of individual nanotubes as a function of concentration applies to the nanotubes in solution and not just after drying. This confirms that the concentration dependence of the bundle size distributions in-situ is a real effect.

5-3-7 Comparing Dilution to Ultra-Centrifugation

The calculated values of M_i/V and M_i/M_T can also be verified by ultracentrifugation. As mentioned previously, centrifugation removes bundles with sizes that are larger than a cut off value, assumed to be close to the size of individual nanotubes. Consequently, the concentration after ultra-centrifugation should be equal to the partial concentration of individual nanotubes before centrifugation (M_i/V).

Similarly, the fraction of the concentration remaining after ultra-centrifugation ($C_{afterCF}/C_{beforeCF}$) should be equal to the mass fraction of individual nanotubes (M_i/M_T) To test this, a starting dispersion was prepared at a concentration of 0.08 mg/mL and from this, two serial dilutions (2.7×10^{-2} mg/mL and 9×10^{-3} mg/mL) were made with sonication and two similar dilutions were made without. The samples were then ultra-centrifuged at 122,000g for 4 hrs to remove all nanotube bundles. Absorbance spectra were recorded before and after ultra-centrifugation and are shown in Figure 5-13. The absorbance after centrifugation is significantly smaller due to the loss of nanotubes.

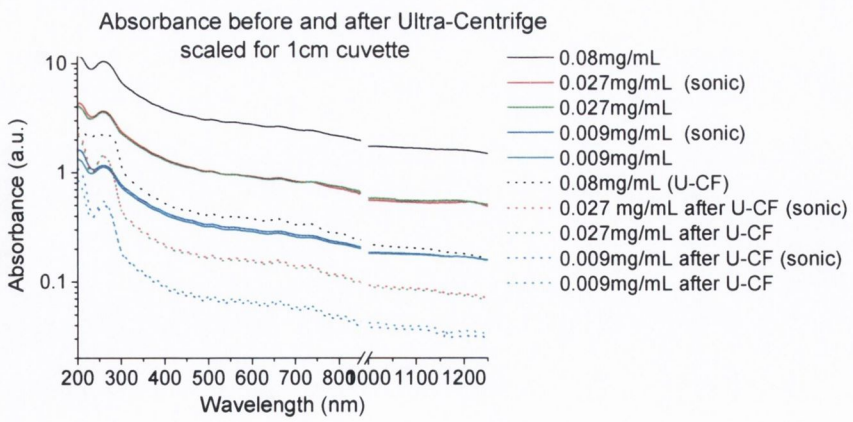


Figure 5-13 UV-VIS-NIR Absorbance Spectra taken before (solid line) and after (dotted line) ultra-centrifugation at 122,000g.

In order to estimate the new concentration after centrifugation, the nanotube extinction coefficient (ε) was calculated by measuring the sample absorbance as a function of concentration. The absorbance divided by cuvette length (Abs/L = εC) are shown in Figure 5-14 (A). It should be pointed out that when the solutions are diluted, the absorption peaks both red shift and blue shift, depending on their wavelength. In addition new peaks appear. These effects are thought to be associated with the debundling of the nanotubes. The absorbance divided by cuvette length at 720 nm is plotted as a function of concentration in Figure 5-14 (B) and was found to scale linearly with concentration as predicted by the Beer-Lambert Law. The extinction coefficient was calculated from the slope of the graph and was found to be 2700 $mLmg^{-1}m^{-1}$. The linearity of this curve is interesting because we know from the AFM measurements that the bundle size distribution varies significantly over this concentration range. Hence, the fact that the absorption-concentration graph is linear suggests that the extinction coefficient is only weakly dependent on the size of the nanotube bundles in solution.

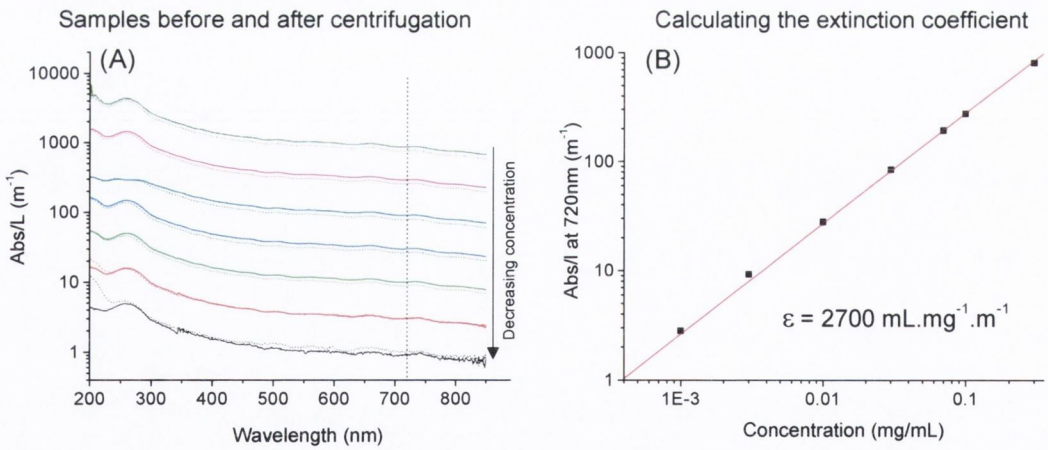


Figure 5-14 (A) UV-VIS absorbance divided by cuvette length (abs/L) as a function of wavelength for a range of concentrations is shown. (B) The absorbance divided by cuvette length at 720 nm is shown as a function of concentration. The extinction coefficient was calculated from the slope, which passes through zero, and was found to be 2700 $mL.mg^{-1}.m^{-1}$. The absorbance scales linearly with concentration as predicted by the Beer-Lambert Law.

It should be noted that the van Hove absorption peaks are relatively broad and that their relative height and width remain unchanged throughout the dilution series. This implies that intensity of the van Hove absorption is influenced by factors other than just the quality of the dispersion. A time-dependent sharpening in the van Hove peaks has been observed, suggesting that it may be related to the wrapping of the DNA. This is investigated further in Chapter 6.

Approximate concentrations after ultra-centrifugation have been calculated from the measured absorbance using the obtained extinction coefficient. The concentrations after ultra-centrifugation (M_i/V) were found to be much higher than the values predicted by the AFM studies. It was found that the original 0.08 mg/mL dispersion had a post-centrifuge concentration of 0.01 mg/mL meaning that 12.5% had remained in solution, while the 0.027 mg/mL dispersions had a new concentration of 0.005 mg/mL equating to 18.5% remaining in solution and the 0.009 mg/mL dispersions had a final concentration of 0.0021 mg/mL showing that 23.3% remained in solution. This is far greater than the values of M_i/M_T measured in the AFM studies as shown in Figure 5-15 (A).

One explanation for the high concentrations is that the ultra-centrifugation has not removed all the bundles from the solution. New values of M_i/M_T and M_i/V were calculated from the AFM data to include bundles with diameters below various different cut-off values. It was found that the two sets of data agreed reasonably well (Figures 5-15 (B) & (C)) when a cut-off value of 4 nm was used. Under these circumstances the maximum calculated value of M_i/V from the AFM images shifted up to 0.06 mg/mL in agreement with the absorption results. The values for M_i/M_T were found to increase with decreasing concentration, proving that the number of individual SWNTs and small bundles ($D<4$ nm) does indeed increase with decreasing concentration.

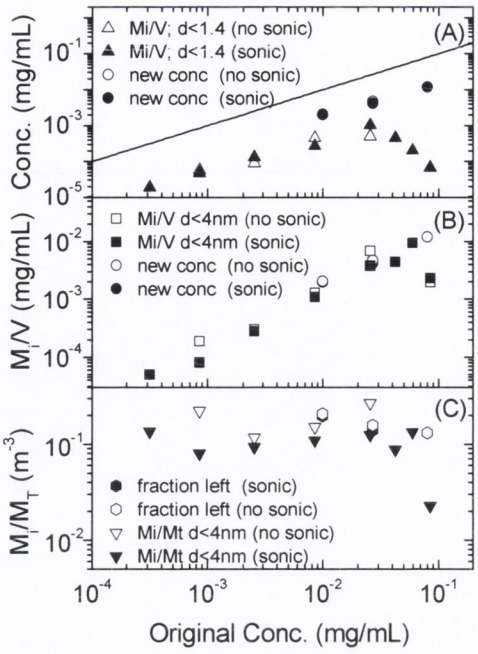


Figure 5-15 (A) The concentration of the samples after ultra-centrifugation as calculated by absorption spectroscopy and the partial concentration of individual nanotubes before centrifugation, M_i/V as calculated from the diameter distributions. These values were expected to be equal. However, it is clear that the concentrations after ultra-centrifugation are greater than the values of M_i/V. The straight line shows the original concentration. (B) Values of M_i/V were recalculated from diameter distributions to include bundles of up to 4 nm. These values agreed well with the values obtained from ultra-centrifugation. (C) The ratio of the concentration before to the concentration after ultra-centrifugation should be equal to the mass fraction of individual nanotubes, M_i/M_T. It was found that this data also agreed well when a cut-off value of 4 nm was used.

AFM images were taken of the dispersions after ultra-centrifugation. Two representative images are shown in Figure 5-16. Diameter distributions measured from these and other images are presented in Figure 5-17. These confirmed that fact that bundles with diameters of up to 4 nm had indeed remained in solution. This was an unexpected result, contradicting reports in literature[11,16,17] where it is assumed that ultra-centrifugation removes all but the individual SWNTs. Even at the lowest

concentration studied (0.0021 mg/mL after centrifugation), a number of small bundles remain. In fact, these diameter distributions are very close to equilibrium, concentration dependent, distributions for the relevant concentrations as shown in Figure 5-5. This shows that ultracentrifugation is, in fact, equivalent to dilution. Both procedures work by reducing the nanotube concentration, allowing the bundle diameter distribution to come to a new equilibrium with a reduced mean. The difference is that dilution works by the addition of solvent while ultracentrifugation works by removal of solute. This discovery raises further questions as to the advantages of ultra-centrifugation over dilution.

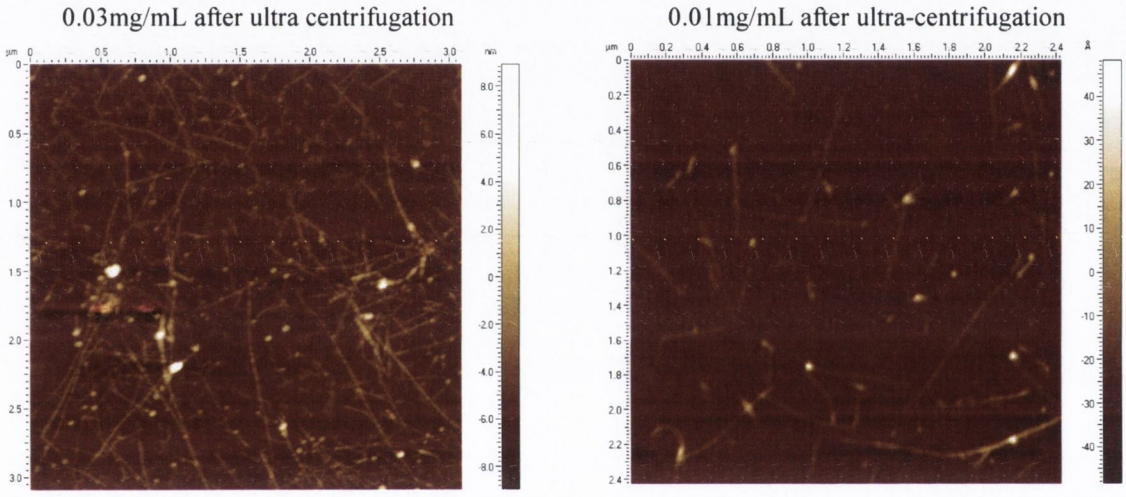


Figure 5-16 AFM images of the 0.027 mg/mL solution and the 0.009 mg/mL solution after ultra-centrifugation.

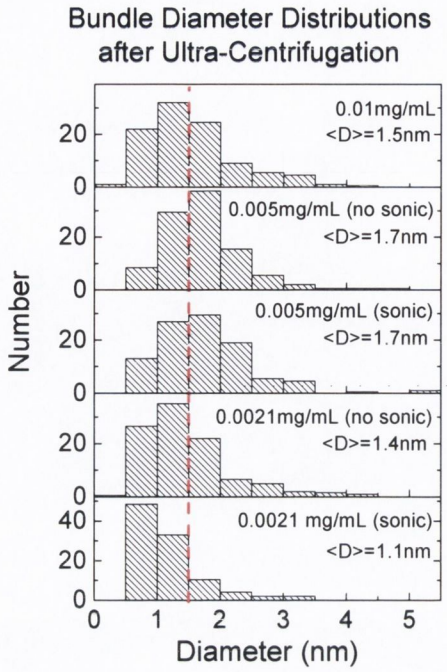


Figure 5-17 Bundle diameter distributions for samples diluted to a range of concentrations, measured after ultracentrifugation. The text in each panel indicates the concentration (after ultracentrifugation); whether the sample was sonicated after dilution and the mean diameter. The dashed, vertical red line represents the diameter of the largest individual SWNT in this material.

5-4 Conclusion

In conclusion, we have found natural salmon testes DNA to be an excellent dispersant of SWNT in aqueous solutions. It has been shown that the distribution of bundle diameters within a sample is critically dependent on nanotube concentration rather than on sonication. It has also been shown that debundling occurs spontaneously when the concentration of the solution is reduced, leading to the conclusion that DNA-SWNT hybrids exist in water as a solution rather than as a dispersion. We have discovered that at low concentrations, dispersions with number densities of up to 83% individual SWNTs, equating to partial concentrations of up to 6.2% can be achieved. This clearly demonstrates that dilution could be used as a viable and cost effective alternative to ultra-centrifugation. However, if ultra-centrifugation is the preferred method for obtaining individually dispersed SWNTs, it has been found that the partial concentration of individual SWNTs is maximised in dispersions with a nanotube concentration of ~0.027 mg/mL. It must also be noted that bundles with diameters of up to 4 nm remained solution even after 4 hrs ultra-centrifugation at 122,000g.

5-4 References

1. Coleman, J. N. et al. Binding kinetics and SWNT bundle dissociation in low concentration polymer-nanotube dispersions. Journal of Physical Chemistry B 108, 3446-3450 (2004).
2. Giordani, S. et al. Debundling of Single-Walled Nanotubes by Dilution: Observation of Large Populations of Individual Nanotubes in Amide Solvent Dispersions. J. Phys. Chem. B 110, 15708-15718 (2006).
3. Nicolosi, V., Vengust, D., Mihailovic, D., Blau, W. J. & Coleman, J. N. Debundling by dilution: Observation of significant populations of individual MoSI nanowires in high concentration dispersions. Chemical Physics Letters 425, 89-93 (2006).
4. Barisci, J. N. et al. Properties of carbon nanotube fibers spun from DNA-stabilized dispersions Advanced Functional Materials 14, 133-8 (2004).
5. Dovbeshko, G. I., Repnytska, O. P., Obraztsova, E. D. & Shtogun, Y. V. DNA interaction with single-walled carbon nanotubes: a SEIRA study Chemical Physics Letters 372, 432-7 (2003).
6. Gigliotti, B., Sakizzie, B., Bethune, D. S., Shelby, R. M. & Cha, J. N. Sequence-Independent Helical Wrapping of Single-Walled Carbon Nanotubes by Long Genomic DNA Nano Lett. 6, 159-164 (2006).
7. Nakashima, N., Okuzono, S., Murakami, H., Nakai, T. & Yoshikawa, K. DNA Dissolves Single-walled Carbon Nanotubes in Water Chemistry Letters 32, 456 - 457 (2003).
8. Badaire, S. et al. Liquid crystals of DNA-stabilized carbon nanotubes. Advanced Materials 17, 1673-1676 (2005).
9. Arnold, M. S., Stupp, S. I. & Hersam, M. C. Enrichment of single-walled carbon nanotubes by diameter in density gradients Nano Lett. 5, 713-718 (2005).
10. Strano, M. S. et al. Understanding the nature of the DNA-assisted separation of single-walled carbon nanotubes using fluorescence and Raman spectroscopy Nano Letters 4, 543-50 (2004).
11. Zheng, M. et al. DNA-assisted dispersion and separation of carbon nanotubes Nature Materials 2, 338-342 (2003).
12. Zheng, M. et al. Structure-based carbon nanotube sorting by sequence-dependent DNA assembly Science 302, 1545-8 (2003).
13. Chen, R. J. & Zhang, Y. Controlled precipitation of solubilized carbon nanotubes by delamination of DNA Journal of Physical Chemistry B 110, 54-57 (2006).
14. Chou, S. G. et al. Optical characterization of DNA-wrapped carbon nanotube hybrids Chemical Physics Letters 397, 296-301 (2004).
15. Huang, X., McLean, R. S. & Zheng, M. High-resolution length sorting and purification of DNA-wrapped carbon nanotubes by size-exclusion chromatography Analytical Chemistry 77, 6225-6228 (2005).

16. Hu, C. et al. DNA functionalized single-walled carbon nanotubes for electrochemical detection. Journal of Physical Chemistry B 109, 20072-20076 (2005).
17. O'Connell, M. J. et al. Band gap fluorescence from individual single-walled carbon nanotubes. Science 297, 593-596 (2002).
18. Nicolosi, V. et al. Solubility of $Mo_6S_{4.5}I_{4.5}$ nanowires in common solvents: A sedimentation study. Journal of Physical Chemistry B 109, 7124-7133 (2005).
19. Heller, D. A. et al. Optical detection of DNA conformational polymorphism on single-walled carbon nanotubes. Science 311, 508-11 (2006).
20. Lustig, S. R., Jagota, A., Khripin, C. & Zheng, M. Theory of structure-based carbon nanotube separations by Ion-exchange chromatography of DNA/CNT hybrids Journal of Physical Chemistry B 109, 2559-2566 (2005).
21. Coleman, J. N. et al. Improving the mechanical properties of single-walled carbon nanotube sheets by intercalation of polymeric adhesives. Applied Physics Letters 82, 1682-1684 (2003).
22. Giordani, S. et al. Debundling of single-walled nanotubes by dilution: observation of large populations individual nanotubes in amide solvent dispersions. Journal of Physical Chemistry B 110, 15708-18 (2006).
23. Tucknott, R. & Yaliraki, S. N. Aggregation properties of carbon nanotubes at interfaces. Chemical Physics 281, 455-463 (2002).

Chapter 6

The Evolution of DNA wrapping of Nanotubes

6-1 Introduction

While undertaking previous experiments on the dispersion efficiency of DNA, a number of unusual effects were observed which warranted further investigation. In particular, two principle observations were cause for interest. Firstly, a time-dependent sharpening of the van Hove absorption peaks was observed, and secondly, samples which had no detectable near-IR photoluminescence (PL) spectra when first prepared were found to have strong peaks two months later. According to literature, well-resolved absorption spectra and intense fluorescence peaks are an indication of a large population of individually dispersed SWNTs, while the aggregation is known to quench fluorescence and broaden the van Hove peaks[1-7]. By this understanding, one conclusion is that the DNA-SWNT samples must initially be dominated by bundles, which slowly break up to yield a solution that is rich in individually dispersed nanotubes. However, AFM analysis shows that a significant population of individual SWNTs is present when the samples are first prepared[8]. Consequently, it was thought that more complex factors might be influencing the optical properties of the system. The nanotubes' optical properties are sensitive to their chemical environment[9-15] and so a number of different factors could be responsible for the observed changes. These factors are; 1) interactions between the nanotube and the surrounding solvent; 2) interactions between the nanotubes and the DNA; 3) interactions between different nanotubes; and 4) photochemical processes, where the absorption of light provides the necessary activation energy for reactions to occur. It was decided to carry out a full kinetic study in order to better understand these properties.

A solution was prepared at a concentration of 0.025 mg/mL, with a ratio of 2:1 (DNA:SWNT) using double stranded salmon testes DNA in D_2O as described in Chapter 4. The concentration after centrifugation was established using absorption

spectroscopy and was found to be 0.018 mg/mL. In order to ensure that the changing optical properties were not caused by photochemistry processes, half the sample was kept in the dark, while the other half was kept under ambient light conditions. Both solutions were maintained at room temperature (~22 °C) throughout the experiment. The solutions were monitored weekly using five different methods of analysis. UV-VIS-NIR absorption spectroscopy was used to probe the nanotubes and monitor the concentration of the sample; circular dichroism was employed to check for changes in the conformation of the DNA; NIR photoluminescence (PL) spectroscopy was utilised to probe the individual semiconducting nanotubes; AFM was used to monitor changes in the bundle diameter distributions and high resolution TEM allowed us to examine the DNA-SWNT complexes. Both solutions were monitored for just over three months. No significant differences were observed between the two samples. Consequently only the results from the dark sample are presented in this chapter. It will be shown, that the observed changes in the optical properties are directly linked to the degree of DNA wrapping of nanotubes in the samples.

6-2 Results

6-2-1 Absorption and Photoluminescence Spectroscopy

The UV-VIS-NIR absorption spectra are presented in Figure 6-1 (A) with some of the spectra omitted for clarity. Significant changes in the absorption spectra were observed over the 3 month duration of this experiment, characterised by a transformation from badly-defined absorption peaks to a set of intense, well-resolved peaks. The inset shows an expanded view of two S_{22} peaks in the 600 nm to 800 nm wavelength region. These peaks were observed to blue-shift slightly between days 28 and 35. The higher energy peak was found to shift by 4 nm, resulting in a final wavelength of 655 nm, while the lower energy peak shifted by 6 nm, resulting in a final wavelength of 735 nm. The peak heights were measured as described in Figure 4-7 and are shown in Figure 6-1 (B). It was found that both peaks increased slightly in intensity between days 28 and 35. There was no significant change in the peak width (FWHM) over this time.

The most remarkable changes to the spectrum occurred in the 850 nm to 1350 nm region, where S_{11} transitions occur. Initially, the spectrum had no well-defined features in this region. Between days 7 and 28, a set of very broad, weak peaks could be distinguished from the background absorption. By day 35, a major change had occurred in the sample, giving rise to the appearance of intense and well-resolved peaks. No significant change in the spectrum was observed after this time. The peak heights are calculated as shown in Figure 4-7 and are shown as a function of time in Figure 6-1 (B). It is clear that all peaks increased in height between days 28 and 35, but the increase in the S_{11} transitions is far more dramatic than for the S_{22} transitions. The peak positions are shown in Figure 6-1 (C), showing that both the appearance of new peaks and the slight shifting of other peaks between days 28 and 35. A slight decrease in the 260 nm DNA peak height is also observed at later timescales.

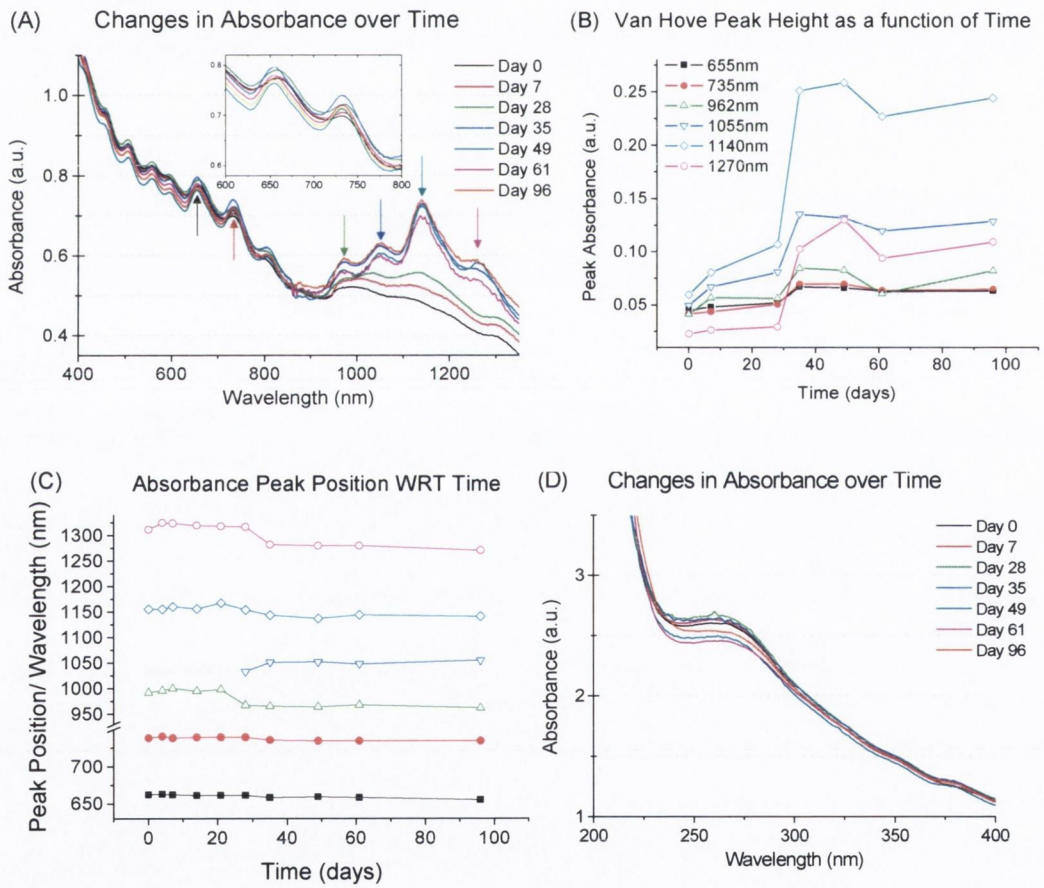


Figure 6-1 (A) The absorption spectra taken at various times over a three month duration. (B) Peak heights are shown as a function of time for various different van Hove peaks (C) Peak position as a function of time. (D) The DNA peak at various different times

Similar time-dependent changes in the solution were observed using NIR photoluminescence spectroscopy (PL). PL line spectra were recorded weekly, exciting at 655 nm and detecting emission over a wavelength range of 900 nm to 1400 nm. Individual semiconducting nanotubes with chiralities of (8,3), (7,5), (7,6) and (9,5) are expected to emit in this wavelength range[1]. PL maps were also recorded in order to check for shifts in the peak positions and changes in the relative peak intensities. The maps were recorded with excitation wavelengths between 550 nm and 890 nm, and emission wavelengths between 900 nm and 1350 nm.

The PL line spectra are shown in Figure 6-2 (A). During the first 28 days, there was virtually no detectable PL emission. Two broad, weak peaks were observed at wavelengths of 1220 nm and 1322 nm. It is possible that the 1220 nm peak could be weak emission from (9,5) nanotubes. However, there are no known emission peaks at 1322 nm. It is likely that both peaks originate from small bundles containing only semiconducting nanotubes, where interactions between adjacent nanotubes causes the emission to become significantly broadened and red-shifted. These peaks do not change significantly in height over the duration of the experiment.

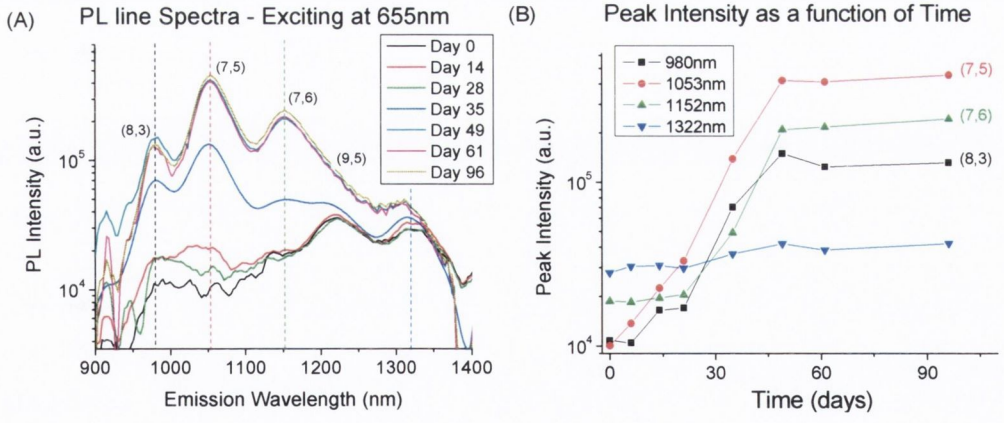


Figure 6-2 (A) NIR-PL line spectra, excited at 655 nm, were recorded weekly over a 3 month period. (B) NIR-PL peak heights as a function of time

In close agreement to observations from the absorption spectroscopy, a major change occurred in the sample between days 28 and 35, causing the PL to be 'switched on', producing a set of PL emission peaks. The intensity of these peaks grew

throughout the following week, yielding an intense, well-defined PL spectrum on day 49. No significant changes in the peak intensities were observed after this time. The peak heights are shown in Figure 6-2 (B), demonstrating that the greatest intensity changes occur between days 28 and 49.

PL maps showed time-dependent intensity changes for a number of other semiconducting peaks. Maps of the solution on days 14 and 96 are presented in Figure 6-3 (A) & (B). The black labels show the nanotube peak positions as calculated by Bachillo *et. al.* for HiPCO SWNTs dispersed with SDS in H_2O[4], while the red labels show peak positions as calculated by Chou *et. al.* for CoMoCAT SWNTs dispersed with oligonucleotides[16].

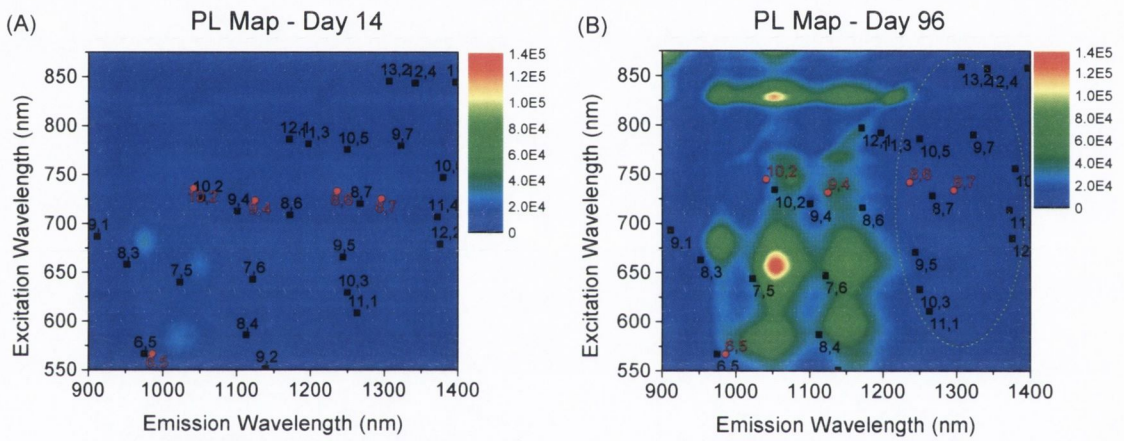


Figure 6-3 (A) A PL map recorded on day 14 (B) A PL map recorded on day 96. The emission peaks from larger diameter SWNT that should be observed at longer emission wavelengths (inside dotted oval) are missing

The emission peaks in the prepared samples are shifted from these assigned positions as a result of interactions between the DNA and SWNTs. On day 14, the map is featureless. However, on day 96 a number of different PL peaks can be clearly seen, demonstrating that a significant number of individual semiconducting SWNTs are present at this time. It should be noted that a set of peaks originating from large diameter nanotubes that are usually observed at longer emission wavelengths are missing. There are two possible reasons for this, either the DNA is selectively debundling the small diameter nanotubes while the large diameter nanotubes remain in

bundles, or the interactions between DNA and nanotube differ on the basis of diameter, resulting in different emission intensities from different diameter nanotubes.

It should be noted that obtaining repeatable emission spectra in the early stages of this experiment proved to be very difficult. It was found that, in young samples, the nanotube emission changed as a result of irradiation with an intense light, such as the excitation beam in the PL spectrometer. The PL emission was observed to increase, and sometimes subsequently decrease, upon exposure to an intense light source. Thus, it was found that the PL spectrum changed slightly after the first line scan was recorded; while the photoluminescence observed after recording a map was significantly different to that observed before. These changes were found to be reversible, disappearing again after a few hours. The changes in emission intensities were found to be extremely small in comparison to the changes observed between days 35 and 49. In addition, this light dependent phenomenon was not observed after day 35. However, in order to minimise the effects of this light dependence on the earlier NIR-PL spectra, the sample was kept in the dark and all line scan were recorded immediately after the sample was removed from the darkened container. Reasons for the observed light dependence are discussed in Section 6-2-6.

As mentioned earlier, the improvement in the absorption and PL spectra could be partially explained by a time-dependent debundling effect increasing the population of individual SWNTs. From earlier concentration studies, it was found that spontaneous debundling could occur in DNA-SWNT dispersions. It was suggested that the system might take far longer to equilibrate than originally anticipated and that the DNA might somehow exfoliate individual semiconducting SWNTs from bundles over time. While this theory does not explain the lack of photoluminescence immediately after sample preparation, when a large population of individual SWNTs is known to be present, it was thought that additional changes in the number fractions of individual SWNTs could be contributing to the observed results. It was therefore decided to monitor the bundle diameter distribution throughout the duration of the experiment.

6-2-2 Atomic Force Microscopy

AFM images of the sample were taken weekly in order to examine the sizes of the nanotubes/bundles in solution. The bundle diameter distributions were calculated by measuring the diameters of 150 nanotubes and are shown in Figure 6-4 (A). It is clear that a large population of very small bundles/nanotubes with diameters of <2 nm is present in the solution at all times throughout the experiment. The mean diameter is shown as a function of time in Figure 6-4 (B). It was found that the mean diameter actually increased from an initial value of 1.5 nm to 2.4 nm over the first 2 weeks of the experiment. The diameters then reduced slightly, settling at a mean value of ~2 nm after day 35. It is thought that the changes in the diameter distribution represents the progression from unwrapped to wrapped SWNTs. Initially, the diameters are very small because the DNA is only very loosely associated with the nanotubes and large areas of the nanotube walls are left uncovered. Thus to a first approximation, the diameter distributions at this time represent the diameters of the nanotubes alone. However, over time the DNA rearranges itself on the walls of the nanotube and finds its optimum conformation, tightly wrapped around the nanotube. The added contribution of the DNA to the hybrid diameter results in the apparent increase in diameter, as measured by AFM at longer timescales. Between these two stages, there must exist a period where the DNA is interacting with the nanotube, but is not tightly wrapped around it. Thus, the DNA contribution to the hybrid diameter will vary during this period, depending on the degree of coverage and the mode of binding. We suggest that this may be the reason for the slightly larger mean diameters, measured on day 14.

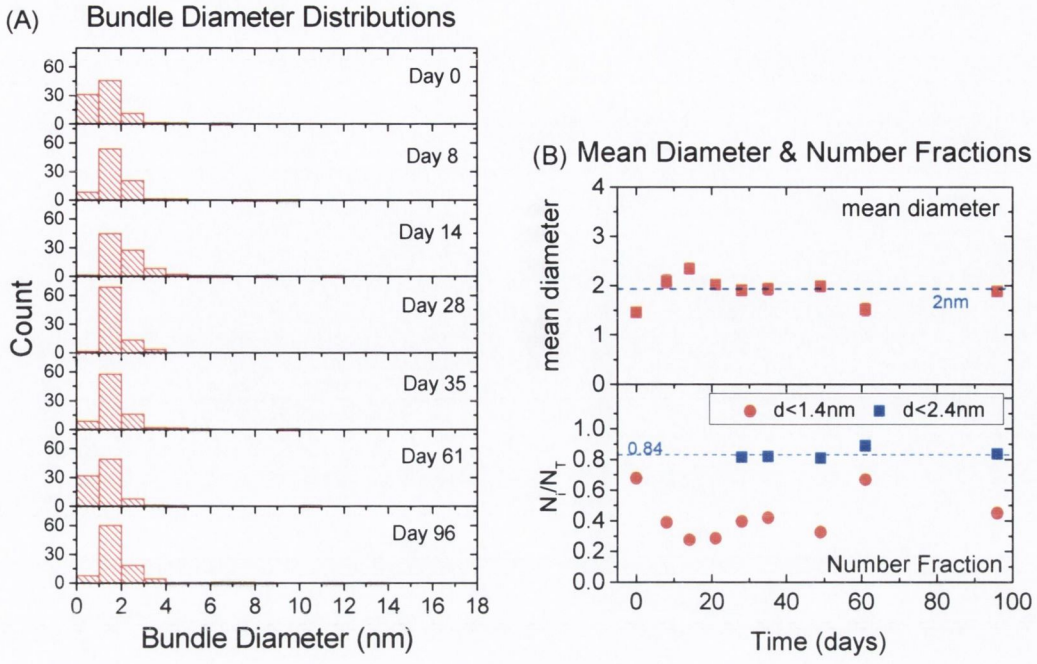


Figure 6-4 (A) Bundle Diameter Distributions for the sample at various times normalised to 100 nanotubes. (B) Mean diameter and number fraction as a function of time. The number fractions are calculated for cut-off values of 1.4 nm (SWNTs only) and 2.4 nm (DNA-SWNT hybrids)

The fraction of individually dispersed SWNTs (N_i/N_T), calculated with a cut-off value of 1.4 nm, is presented in Figure 6-4 (B). Initially this value is very large, indicating that, despite the lack of photoluminescence, a large population of individual SWNTs is present at this time. However, because the cut-off diameter does not allow for the contribution of the DNA to the hybrid diameter, the number fraction appears to decrease over the following weeks as DNA wrapping takes place. For comparison, the values of N_i/N_T are recalculated for the later stages of the experiment to include a DNA contribution of 1 nm to the hybrid diameter. It was found that when DNA coverage is included, the number fraction after day 35 is relatively constant with a value of 0.84 ± 0.04. It can thus be concluded that once the SWNTs are wrapped, the fraction of individual nanotubes remains constant with time. Again, it must be noted that the exact contribution of the DNA to the hybrid diameter at longer timescales is unknown and depends on the mode of binding. The number fractions calculated to include the DNA-wrapping are therefore only approximate.

In conclusion, it is unlikely that the changes in the absorption and photoluminescence spectroscopy can be correlated to a change in the nanotube bundle diameter distribution. The AFM data shows a large population of individual SWNTs present in the solution at all times. The number fractions calculated for the DNA-wrapped nanotubes at longer timescales are slightly greater than those obtained in the early stages of the experiment, indicating that limited debundling may occur. However, the increase is very small and is unlikely to be responsible for the observed changes. It must be noted that the improvement in absorption and PL spectra coincides with the time at which the fluctuations in the mean diameters stabilise. If our understanding of these variations is correct, then it must be considered that the completion of DNA wrapping could be responsible for the changes in the optical properties of the system.

However, while the AFM measurements show that the mean bundle diameter changes during the first 35 days, it is impossible to gain any conclusive information about DNA wrapping using this technique. Another measurement technique that is sensitive to the structure of the DNA is needed to further clarify the role of the DNA wrapping in the observed changes of the optical properties of the solution. Such a technique is circular dichroism spectroscopy, which is sensitive to the conformations adopted by the DNA.

6-2-3 Circular Dichroism Spectroscopy

Circular Dichroism (CD) measurements were carried out weekly on the solution and are shown in Figure 6-5 (A). The observed CD spectrum has positive and negative components, centred around 260 nm. Both components are approximately equal in magnitude and the positive band lies at a higher wavelength than the negative band. This spectrum is typical of right-handed, double-stranded DNA in its B-form[17]. The magnitude of the spectrum was found to continuously decrease throughout the experiment, but the basic pattern remained unchanged. Thus, although the intensity of the signal reduces, it cannot be interpreted as a change in the DNA conformation. The change in magnitude is shown clearly in Figure 6-5 (B) which shows the peak to peak height of the spectra.

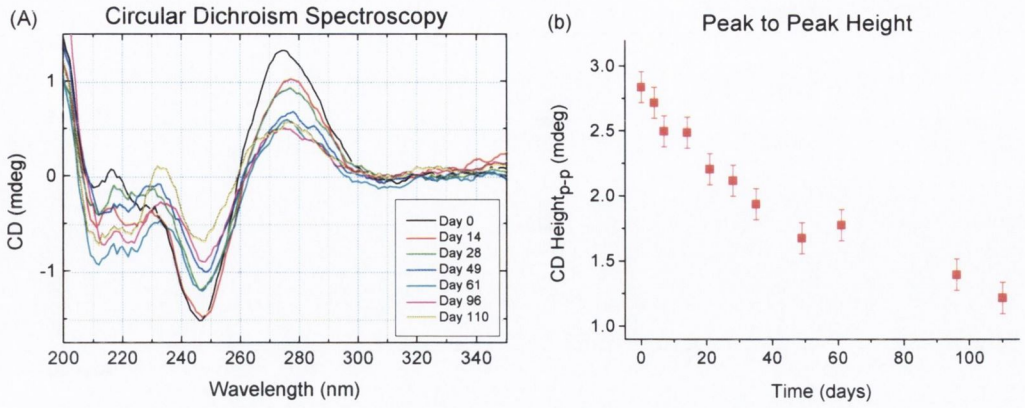


Figure 6-5 (A) Circular Dichroism Spectra recorded at different times throughout the three months. (B) Peak to peak heights of the CD spectra are shown as a function of time

We suggest that these spectra can be interpreted with respect to the fraction of free DNA in solution. The free DNA is not bound to any nanotubes and is free to adopt the usual B-form in water, yielding the spectra observed in Figure 6-5 (A). Initially, the majority of the DNA is free in solution and the CD intensity is maximised. However, as increasingly more DNA adsorbs onto the nanotube walls, the overall CD intensity decreases. It is suggested that nucleotide bases interact with the walls of the nanotube via base-nanotube stacking interactions, while the sugar-phosphate backbone extends away from the nanotube and is exposed to the surrounding water[18]. Therefore, when a strand of DNA adsorbs onto the nanotube walls, the helicity of the backbone changes and the stacking between consecutive nucleotide bases is disrupted. The disruption of stacking between bases leads to a large decrease in the CD intensity. For example, the CD intensity of adenylyl-3'-5'-adenosine (ApA) is a factor of 10 times greater than that of adenosine alone as a result of interactions between the stacked bases[19]. Thus when wrapping occurs, the contribution from base-base stacking interactions disappears and the CD intensity decreases dramatically. In addition, it is possible that electronic coupling between the nucleotide bases and the SWNTs, leads to a decrease in the DNA absorbance intensity and so further decreases the CD intensity. This would account for the slight decrease in the DNA absorption seen at later timescales (Figure 6-1 (D)). This effect has previously been seen for interactions

between anthracene and SWNTs[20]. Thus, as the DNA wraps around the nanotube, the CD effectively switches off.

In order to clarify to relationship between the concentration of free DNA in solution and the intensity of the CD signal, CD measurements were carried out on a number of DNA-only solutions, with concentrations ranging from 0.05 mg/mL down to 0.009 mg/mL. The CD spectra and the peak to peak heights are shown in Figures 6-6 (A) & (B) respectively.

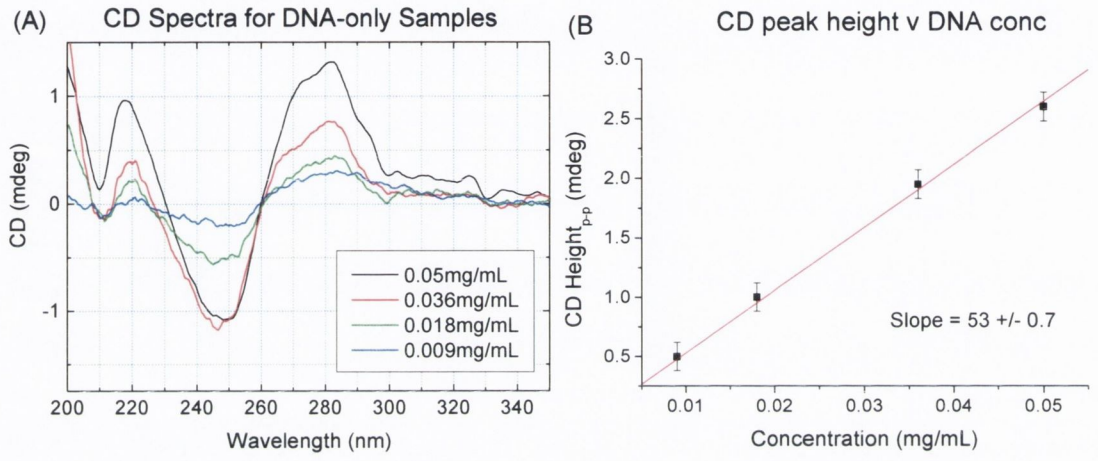


Figure 6-6 (A) CD spectra for DNA-only samples with a range of concentrations. (B) Peak to peak heights of the CD spectra are shown as function of concentration.

Figure 6-6 (B) allows us to determine the relationship between the concentration of free DNA and the CD peak-peak height. Using the slope of 53±0.7 mdeg.mL.mg^{-1}, calculated from Figure 6-6 (B), one can calculate both the concentration of free DNA and the concentration bound DNA (where $C_{boundDNA}=C_{totalDNA}-C_{freeDNA}$) for the DNA-SWNT sample as a function of time as shown in Figure 6-7. It was found that the free DNA in solution on day 0 is ~0.053 mg/mL, which matches well to the concentration of DNA of the solution when first prepared (0.05 mg/mL), within the errors of the spectropolarimeter. This suggests that, while nanotube bundles sediment out of solution during centrifugation, all the DNA remains and so the effective ratio of DNA:SWNTs increases to a value of 2.8:1.

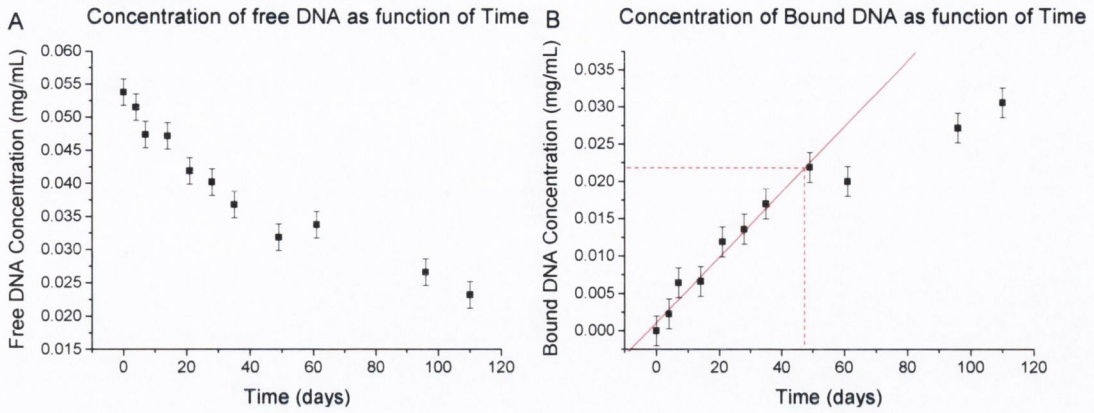
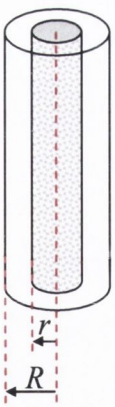


Figure 6-7 Concentration of free DNA (A) and bound DNA (B) as a function of time. The dashed red line shows the time at which a full monolayer of DNA coats the SWNTs

Using the following model, we can, to first approximation, calculate the time at which a full monolayer of DNA covers the walls of the nanotubes.

Firstly, we make the approximation that the bound DNA fully coats the nanotube with a uniform coating (as shown schematically below), yielding a hybrid radius R for a given nanotube of radius r and length L.



Thus, we can say that:

$$\frac{C_{boundDNA}}{C_{NT}} = \frac{m_{boundDNA}/V}{m_{NT}/V} = \frac{\rho_{DNA}\left(R^2 - r^2\right)\pi L}{\rho_{NT}\left(r^2\right)\pi L}$$

where C_{NT} and $C_{boundDNA}$ are the concentrations of the nanotubes and the bound DNA respectively; $m_{boundDNA}$ and m_{NT} are the masses of bound DNA and nanotubes respectively; V is the volume of solution; and ρ_{DNA} and ρ_{NT} are the densities of DNA and nanotubes respectively.

This equation can be rearranged to give:

$$C_{BoundDNA} = C_{NT}\frac{\rho_{DNA}}{\rho_{NT}}\left[\left(\frac{R}{r}\right)^2 - 1\right]$$

To a first approximation, we have assumed that the nanotube radius, $r \approx 0.5$ nm; the hybrid radius, $R \approx 1$ nm; the density of SWNTs, $\rho_{NT} \approx 1500$ kg/m^3; and the density of DNA, $\rho_{DNA} \approx 625$ kg/m^3 (ρ_{DNA} was calculated from HRTEM image analysis as shown in Section 6-2-4). Thus, one can calculate that when a full monolayer coats the nanotube, the concentration of bound DNA ($C_{boundDNA}$) is:

$$C_{BoundDNA} = C_{NT}\frac{625}{1500}\left[\left(\frac{1}{0.5}\right)^2 - 1\right] = 0.022\text{mg/mL}$$

Referring back to Figure 6-7 (B), we find that this concentration of bound DNA occurs on approximately day 47, indicating that a full monolayer of DNA coats the nanotubes at this time. This is a very exciting result as it suggests that the time at which a full DNA monolayer coats the nanotubes coincides with point at which the PL spectra is fully switched on. It should be noted that the concentration of bound DNA increases linearly up to this point, but increases sublinearly after this time. This not unexpected, as DNA and SWNTs are expected to bind readily to one another, however, once the layer of DNA coats the nanotube, the DNA-SWNT hybrid and the DNA have a lower affinity for one another and the binding rate reduces. It must be remembered that the values used in this calculation are only approximate and so the time taken for the monolayer to form may vary slightly from this value.

In conclusion, the CD results suggest that a significant quantity of B-form DNA is present in the samples during the early stages of the experiment. A time dependent reduction in the intensity of the CD has been observed, which can be explained by a shift from a phase dominated by free DNA to one dominated by bound DNA. This suggests that DNA wrapping is indeed occurring over time and that the bound DNA is in single-stranded form, where adjacent bases are unable to interact with each other. The concentrations of free and bound DNA in solution were calculated with respect to time, allowing one to calculate that a full layer of DNA covers the walls of the nanotubes on day 47. This was found to coincide with the time at which the PL is fully 'switched on'. However, these results alone do not produce the

irrefutable evidence needed to confirm this wrapping process. Another technique is required to support this evidence. Such a technique is high resolution transmission electron microscopy (HRTEM), which allows the DNA- nanotube hybrid to be observed in detail.

6-2-4 High Resolution Transmission Electron Microscopy

HRTEM images were recorded by Dr. Valeria Nicolosi in order to investigate the nature of the DNA-nanotube hybrid. Specifically, small volumes of the solution were deposited on holey carbon grids and imaged using a FEI Technai F20 HRTEM at an acceleration voltage of 200kV and a JEOL 400F HRTEM at an acceleration voltage of 100kV. A selection of HRTEM images are shown in the following pages, demonstrating clear evidence for progressive formation of a DNA coating on the nanotubes as a function of time.

The images obtained from the one day old solution show that both individual nanotubes and small bundles are present at this time (Figure 6-8). The DNA appears to be clustered haphazardly around the nanotube bundles, and large areas of the nanotubes are uncoated by DNA. The nanotube walls can be clearly distinguished from their surroundings.

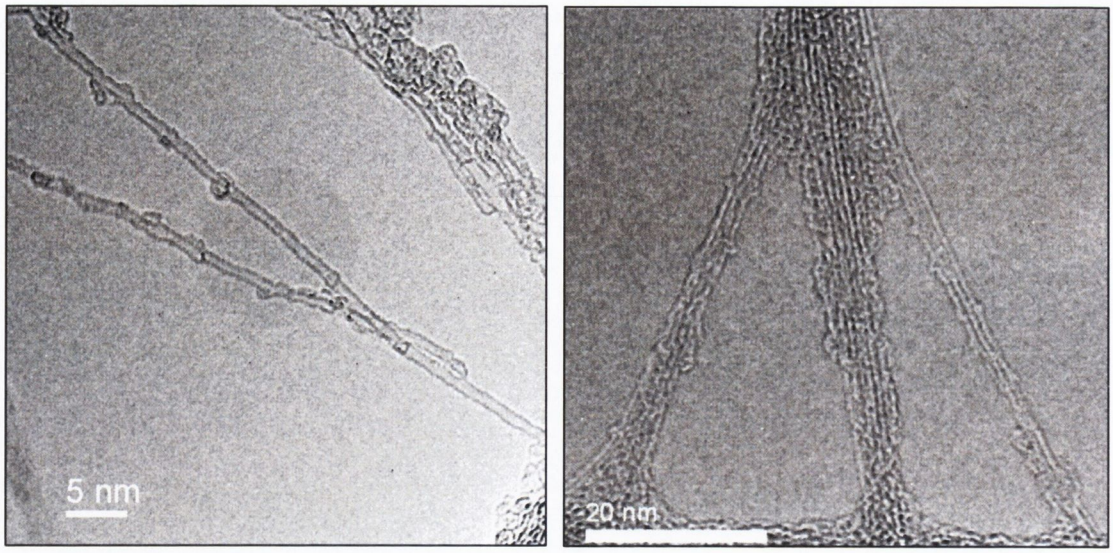


Figure 6-8 HRTEM images recorded from a 1 day old sample

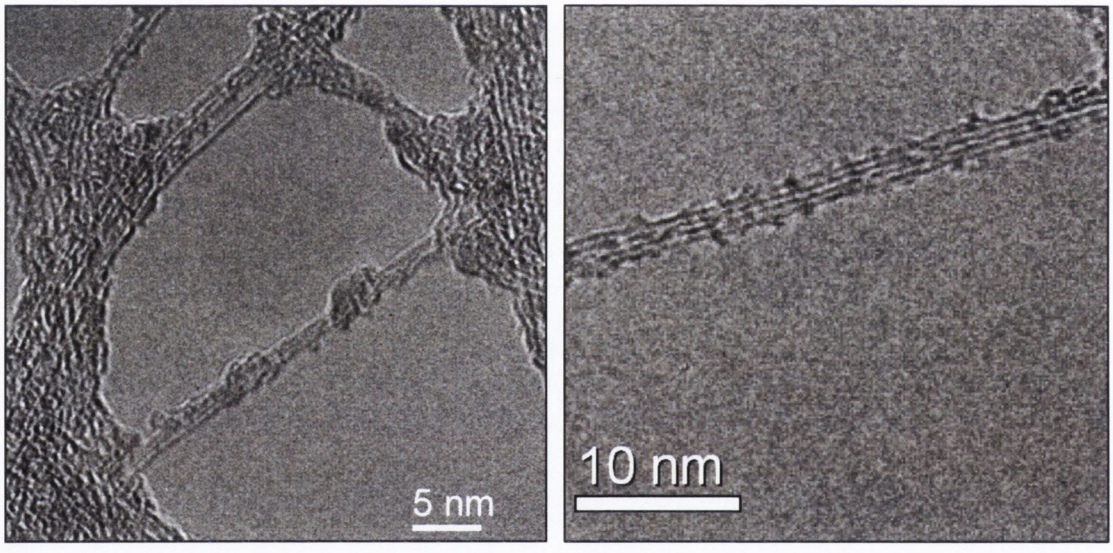


Figure 6-9 HRTEM images recorded on day 16 (left) and day 21 (right)

On day 16, the DNA coverage has increased, but significant areas of the nanotube walls still remain uncoated (Figure 6-9) and the diameter of the hybrid varies hugely along its length. By day 21, DNA can be seen to cover most of the nanotube.

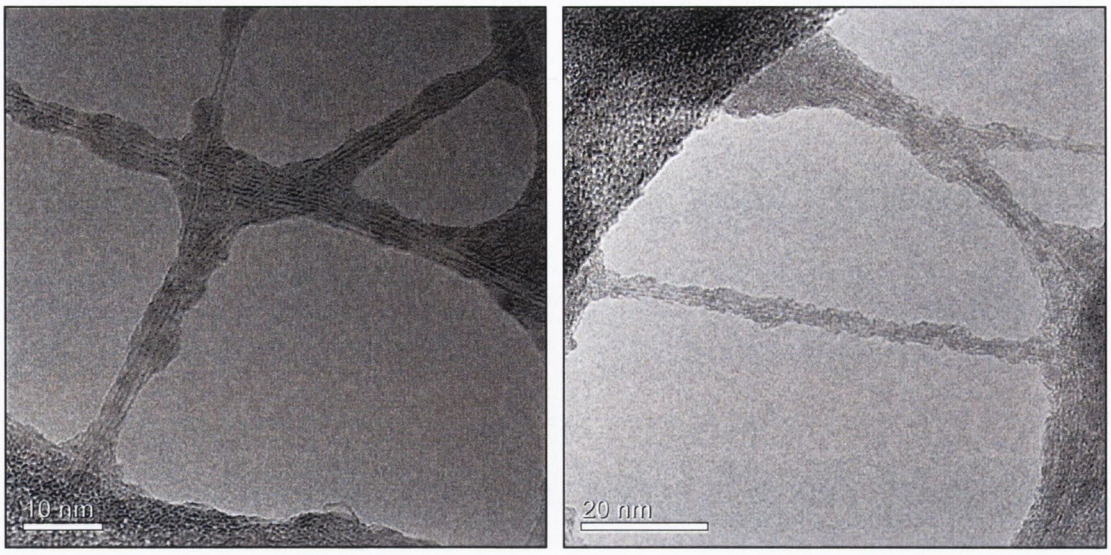


Figure 6-10 HRTEM images recorded from a 35 day old sample

On day 35, almost all of the nanotube walls are coated with DNA (Figure 6-10) and by day 96, there is a thick DNA covering on the nanotubes making it impossible to distinguish the walls of the nanotube the surrounding DNA (Figure 6-11).

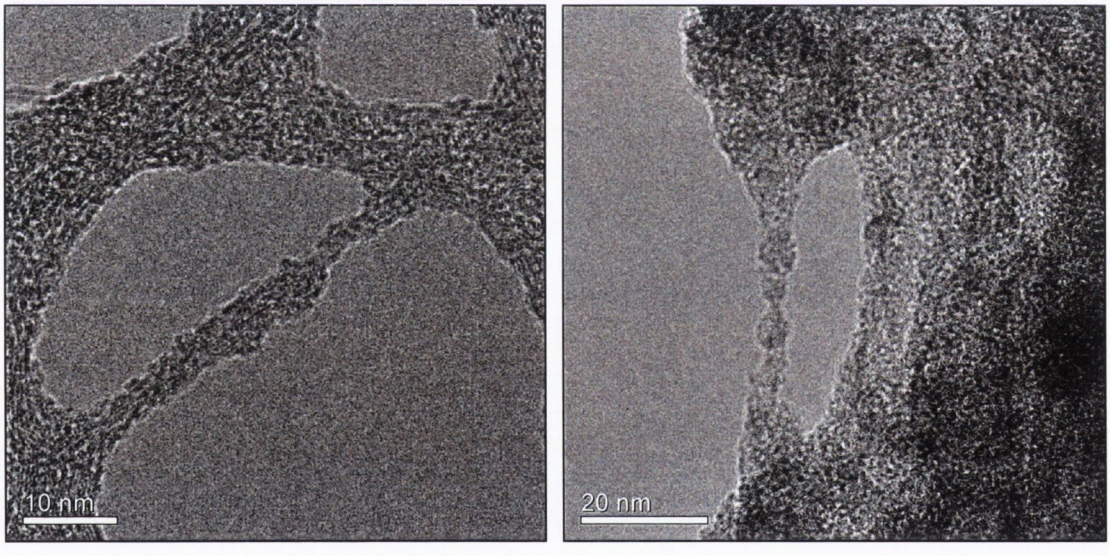


Figure 6-11 HRTEM images recorded from a 96 day old sample

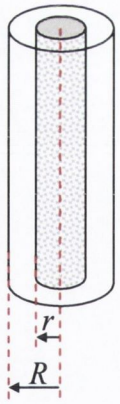
These results are extremely exciting and show overwhelming evidence for the progressive formation of a DNA coating on the walls of the nanotube. It should be noted that the DNA coating on the nanotubes is almost complete by day 35, coinciding with the time at which the absorbance spectra and PL spectra start to improve. Again this suggests that the 'switch on' time for the absorption and PL spectra is linked to the

completion of a DNA monolayer. It should also be noted that while the absorption spectra reaches its maximum intensity by day 35, the PL grows over a longer timescale, starting to increase in intensity on day 35 and reaching its maximum intensity by day 49, coinciding with the time at which a full monolayer coats the nanotubes according to the CD data. Thus, it can be concluded that the PL spectra is more sensitive to the degree of DNA coverage than the absorption spectra. However in both cases, changes in the fluorescent and absorption properties are observed once the majority of the nanotube walls are coated in DNA.

To verify the model used to calculate the concentrations of free DNA from the CD data, we can compare the calculated concentrations of free DNA to the observed DNA coverage in the HRTEM images. Assuming that the DNA coverage of the nanotubes in the HRTEM images is typical of all nanotubes in solution, it is possible to measure both the area of the image covered by the DNA-nanotube hybrid ($A= 2R.L$) and the area covered by the nanotube alone ($a=2r.L$).

To a first approximation, one can assume that:

$$\left(\frac{A}{a}\right)^2 \equiv \left(\frac{R}{r}\right)^2$$



Again, we make the approximation that the bound DNA fully coats the nanotube with a uniform coating, yielding a hybrid diameter $D=2R$ for a given nanotube of diameter $d=2r$ and length L. While this approximation is known to be incorrect during the earlier stages of the experiment at least, the aim is to calculate the concentration of free DNA in solution and therefore the way in which the DNA is bound to the walls of the nanotube is immaterial to this calculation.

Thus: $$C_{freeDNA} = C_{totalDNA} - C_{NT}\frac{\rho_{DNA}}{\rho_{NT}}\left[\left(\frac{R}{r}\right)^2 - 1\right]$$

The concentration of free DNA ($C_{freeDNA}$), calculated from the CD data, is plotted as a function of the calculated values of $\left[\left(\frac{R}{r}\right)^2 - 1\right]$ in Figure 6-12, allowing one to calculate a value of 625 $kg.m^{-3}$ for ρ_{DNA} from the slope.

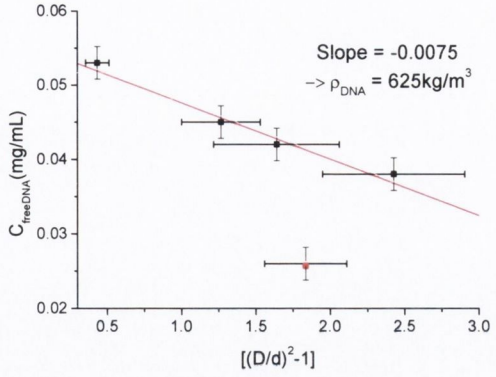


Figure 6-12 CD peak-to-peak height as a function of $[(R/r)^2-1]$ as calculated from HRTEM images

These values agree very well at all timescales except day 96 (shown in red), when the DNA wrapping is so advanced that it is impossible to see the walls of the nanotube and so the obtained values of A/a (≡ R/r) are very inaccurate. It can therefore be assumed, that in the early stages of the experiment at least, the concentrations of free DNA calculated from the CD data, are indeed dependent on the DNA coverage, as observed in the HRTEM images.

According to molecular modelling experiments, single-stranded DNA binds to nanotube by wrapping helically around the nanotube[18,21]. Phase images from AFM have shown periodic helical wrapping of nanotubes for single-stranded DNA[22,23]. However, to our knowledge no evidence for helical wrapping has been shown to date for nanotubes dispersed with double-stranded DNA (ds-DNA). In addition, DNA wrapping has never been observed with HRTEM for either single-stranded or double-stranded DNA. We therefore present the following HRTEM images (Figure 6-13 (A) – (D)) showing the helical wrapping of nanotubes by salmon testes DNA, approximately one month after sample preparation. These images suggest that the nanotubes are wrapped by two separate strands of DNA. In transmission electron microscopy, the electron beam is transmitted through the sample, making it impossible to differentiate between the front and back of the specimen. Thus, the DNA on both the front and back of the nanotube can be seen in the images, appearing to criss-cross along the length of the nanotube. We suggest that this is the backbones of two individual strands of DNA wrapping helically around the nanotube, phase-shifted by 180° with respect to each other, creating the criss-crossing pattern shown schematically in Figure 6-13E (right).

By comparison, a single strand of DNA would make a zig-zag pattern (Figure 6-13E (left))

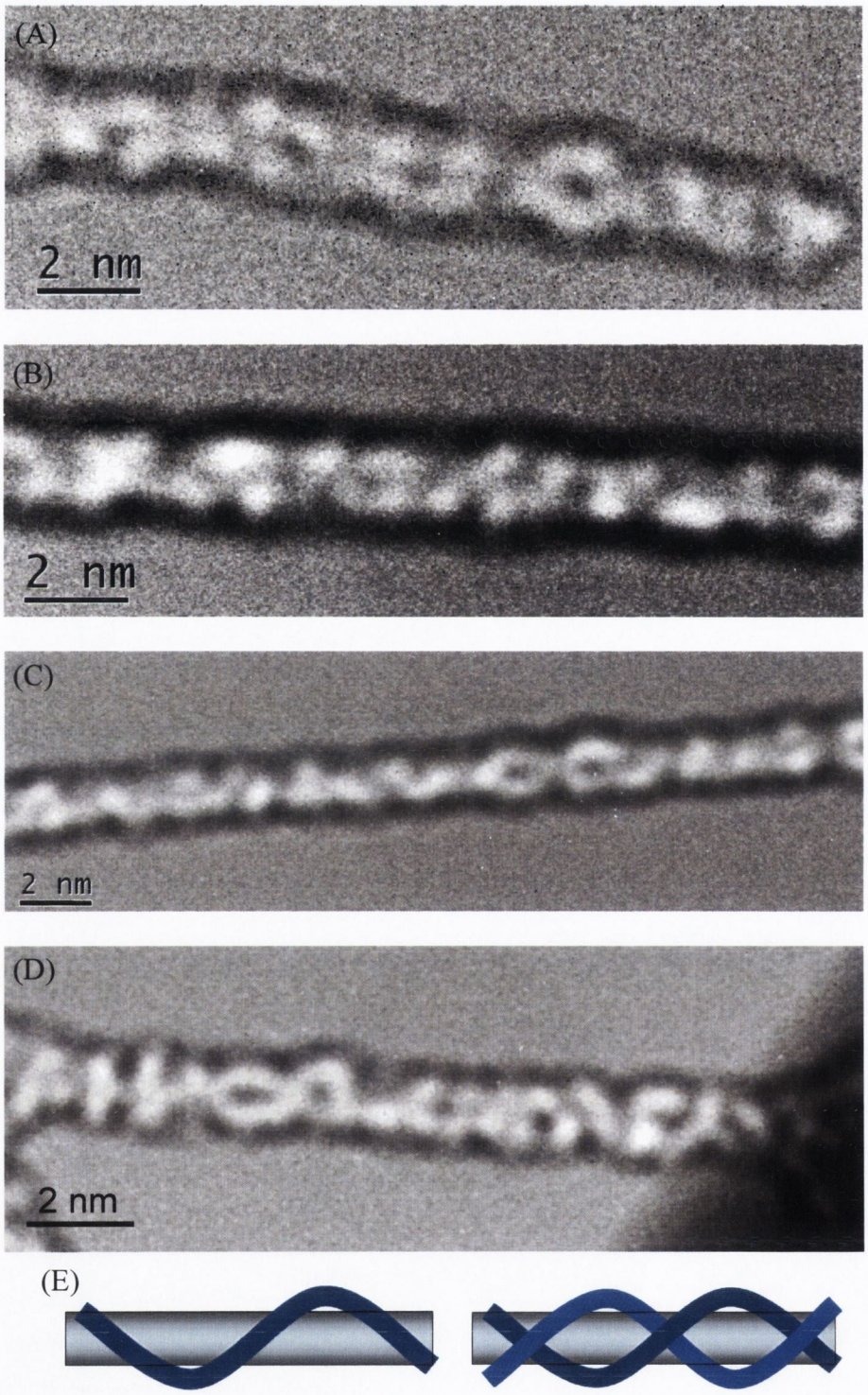


Figure 6-13 (A-D) Various HRTEM images showing DNA wrapping of nanotubes for a 35 day old sample. (E) Schematic diagrams for single-stranded & double-stranded wrapping

These images suggest that the binding mechanism of ds-DNA and SWNTs is one in which the ds-DNA unzips onto the nanotube, allowing the two separated strands to interact with the nanotube. This mechanism could be facilitated by dangling ends on the ds-DNA interacting with the SWNT. By phase shifting by 180° with respect to each other, both the nanotube coverage and the distance between the negatively-charged phosphates on the backbone of each strand are maximised. It should be noted that this unzipping mechanism suggests a possible reason for the need to prevent heating in the dispersion during the initial sonication. If the ds-DNA was allowed to gain enough thermal energy to denature, it is likely that the long single-stranded DNA molecule would then interact with many different SWNTs, binding them together and creating large aggregates of SWNTs. However, by keeping the DNA at low temperatures and forcing it to unzip onto the SWNT, it is more likely to attach to just one SWNT, thus mediating debundling.

6-2-5 Temperature Studies

While the previous analysis shows clear evidence for the progressive wrapping of nanotubes by DNA and its influence on the solution's optical properties, many questions still remain. In particular, we hoped to gain a greater understanding of the factors controlling the wrapping process and to explain the reasons for the improvement in the PL and absorption spectra which occurs when a full monolayer of DNA covers the SWNT. It was suggested that the wrapping process is dependent on unzipping the DNA, and thus energy is required to overcome the stacking interactions and the hydrogen bonding. By increasing the temperature of the solution, we hoped to accelerate the unzipping of the double-stranded DNA and thus, decrease the timescale for DNA wrapping of the nanotubes to occur. It was decided to carry out a series of temperature experiments in order to clarify the effects of elevated temperature on the solutions. Three samples were prepared at a concentration of 0.018 mg/mL and a ratio of 2:1 by sonicating for 2 hrs in an ice sonic-bath and held at temperatures of 35 °C, 45 °C and 55 °C respectively.

As before, a time-dependent improvement in the absorption and NIR-PL spectra, coupled with a reduction in the CD intensity was observed. The timescales for

these changes were found to reduce as the solution temperature increased. The peak heights for the 1053 nm and 1152 nm peaks are shown for each sample in Figure 6-14 (A). The vertical dashed blue lines show the times, *t*, at which the PL is deemed to be fully switched on in each sample. This was found to range from 49 days in the 22 °C sample, to just 10 days in the 55 °C sample. The shape and magnitude of the PL signal was found to vary with temperature. Figure 6-14 (B) shows the PL spectra of each sample at the 'switch on' times (as shown by the vertical blue lines). It was found that the 35 °C sample had the strongest photoluminescence, while the spectra for the 45 °C and the 55 °C samples are very weak. The emission peaks were observed to blue-shift by ~3-6 nm in the 45 °C and 55 °C solutions, and visible aggregation was observed in both samples over time. For completeness, a similar, one-day-old DNA-SWNT solution was refluxed at 110° for between 1 and 4 hrs. Weak NIR-PL emission and a slight improvement in the absorption spectra were observed after 4 hrs refluxing as shown in Figure 6-14 (C). The emission spectrum was blue shifted by ~10 nm with respect to the 35 °C solution.

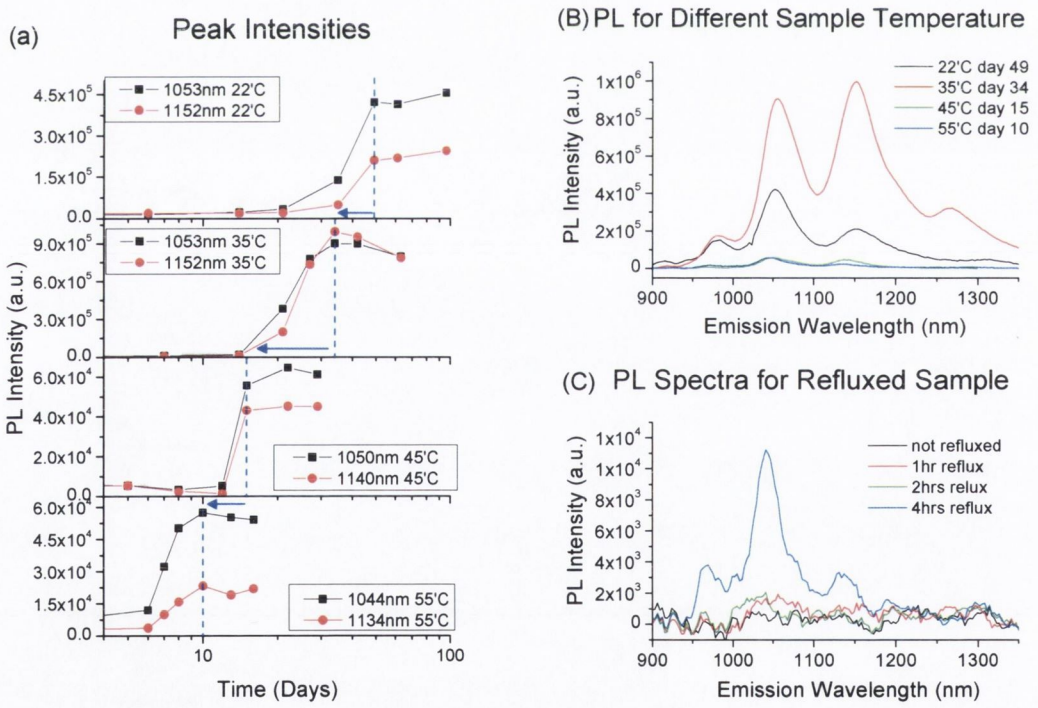


Figure 6-14 (A) Peak heights are shown as a function of time for four different samples with temperatures ranging from 22 °C to 55 °C. The blue lines show the time *t* at which the PL is 'switched on' (B) PL line spectra, exciting at 655 nm, for each sample at time *t*. (C)* PL spectra, exciting at 655 nm, for a sample after refluxing

A NIR-PL map of the 35 °C solution on day 34 is presented in Figure 6-15 (A). All nanotube peaks have increased in intensity with respect to the room temperature sample and the emission peaks from large diameter nanotubes that were previously missing are present in this sample. Thus, either there is greater degree of debundling of all (n,m) nanotube species in the 35 °C solution, or there is better interaction between the DNA and SWNT increasing NIR-PL emission of all semiconducting nanotubes. AFM analysis shows that the diameter distribution is slightly greater in the 35 °C sample (Figure 6-15 (B)), with a mean diameter of 2.5 nm and number fractions of 0.74 for d ≤ 2.4 nm or 0.35 for d ≤ 1.4 nm. Thus, the increase in PL emission cannot be attributed to extensive debundling.

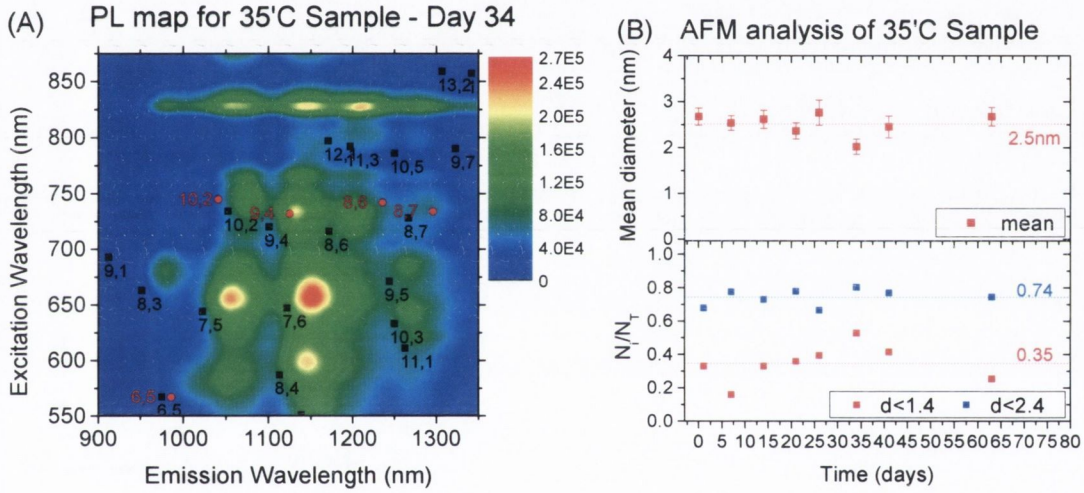


Figure 6-15 (A) PL map for 35 °C sample. It should be noted that the coloured intensity scale is approximately two times greater than for the 22 °C sample. The peaks from larger diameter SWNT that were missing in the 22 °C sample are present here. (B) Mean diameters and number fractions for the 35 °C sample as calculated from AFM images.

In order to gain a better understanding of the temperature dependence of the rate of DNA wrapping, the data was analysed using the Arrhenius equation:

$$\frac{1}{t} = Ae^{-\varepsilon_A/kT}$$

where t is the time taken for the PL to switch on, A is a pre-exponential factor, k is the Boltzmann constant, T is the temperature of the system and ε_A is the activation energy.

Taking the natural log of each side of the equation gives:

$$-\ln(t) = {}^{-\varepsilon_A}/_{kT} + \ln(A)$$

Figure 6-16 shows a plot of -ln(t) as a function of $1/T$, giving a straight line with a slope of $-\varepsilon_A/k$. The activation energy was calculated from the slope and found to be 0.43 eV (41 kJ.mol^{-1}).

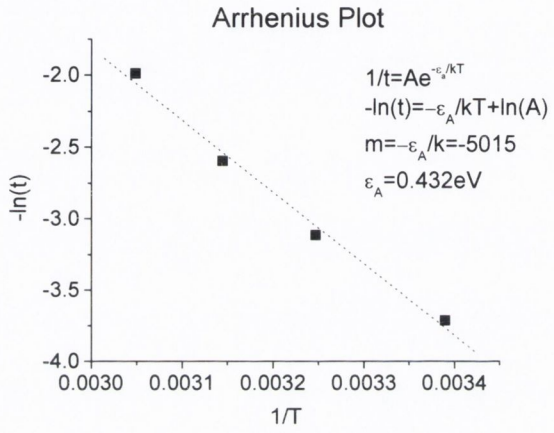


Figure 6-16 The activation energy is calculated from the slope of the Arrhenius plot as 0.43 eV

Thus, it can be concluded that there is some rate limiting process with an activation energy of ~0.43 eV, that controls the time, t, taken for a full monolayer of DNA to cover the walls of the SWNT. It is not yet understood what this rate limiting process is. However, the activation energy lies within the range of the activation energies that are observed for polynucleotide duplex formation, which typically range from -0.5 eV to 0.7 eV, depending on both base sequence and salt concentration[17]. When two polynucleotide strands form a duplex, the rate limiting step is the formation of a nucleus containing a small number of base pairs (generally 4–6 base pairs). Once this nucleus has formed, it is energetically favourable for the rest of the base pairs to zip up, forming the double helix. Thus, the activation energy is relatively small and is dependent on the sequence of the base pairs in the nucleus. The stability of the nucleus is temperature dependent and as the temperature increases, the stability decreases. Thus, for some base sequences, negative activation energies are observed. The dissociation of a duplex requires that all the base pairs in the chain break to return to

this nucleus. Consequently, the energy need to dissociate the duplex is much larger and increase with increasing chain length. Activation energies of 4 eV have been calculated for the dissociation of a duplex containing 18 base pairs[24]. Thus, the low activation energy obtained for the DNA-SWNT samples implies that the mechanism of DNA wrapping cannot be one in which the DNA duplex fully dissociates before covering the nanotube walls. Rather, it is more likely that a small number of base pairs dissociate and interact with the nanotube, allowing them to unzip onto the walls of the nanotube. The dissociation of a small number of base pairs would yield activation energies similar to those observed in this experiment[17]. An activation energy of 40 kJ/mol is equivalent to breaking 10 hydrogen bonds, which would equate to the dissociation of 4–5 base pairs. Thus, it is possible that this is the rate limiting process in the system.

6-2-6 Role of O_2 and pH in PL quenching

While it is known that the PL emission and van Hove absorption intensity increase dramatically upon the completion of a full monolayer coverage of DNA, little is yet understood about the processes controlling this sudden change. Computational calculations carried out by Wall et. al. show that these changes cannot be attributed to a change in the electronic structure of the nanotube as a result of interactions between the nanotube and DNA[25]. Intuitively, it would seem that the DNA coating must segregate the SWNT from its surroundings, possibly shielding the nanotube from the surrounding water which is known to decrease NIR-PL emission through non-radiative decay processes[13]. However, it is unlikely that this fully explains the results. Similar luminescence quenching has been observed for SWNTs dispersed with surfactants in water[12,26], when exposed to oxygen under low pH conditions. It was found that both O_2 and H^+ were necessary for quenching to occur. It was suggested that the oxygen reversibly interacts with the walls of the SWNT, covalently bonding across a C_6-hexagon, creating a 1,4-endoperoxide as shown in Figure 6-17 (A)[26]. This covalently bonded endoperoxide ring does not effect the PL emission. However, under acidic conditions, the endoperoxide ring can open and protonate, creating a delocalised hole in the π-band of the SWNT as shown in Figure 6-17 (B) and (C)[26]. The delocalised

hole decreases photoabsorption intensities and quenches luminescence by non-radiative Auger recombination. This effect is greater for larger diameter nanotubes. When the pH is increased, the oxygen deprotonates, reforming the endoperoxide ring, and the NIR-PL returns.

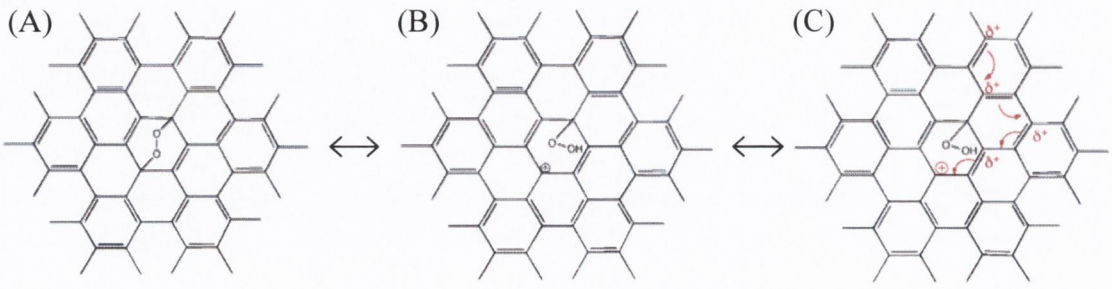


Figure 6-17 Mechanism proposed by Dukovic et. al. [26] for the formation of the SWNT endoperoxide which can be protonated to form the hydroperoxide carbocation.

This mechanism could help explain the effects observed in our solutions. It is possible that the DNA wrapping either removes surface oxides from the nanotube, or prevents their protonation. The SWNTs used throughout our experiments were handled in air. In addition, no effort was made to deoxygenate the water during sonication. Thus it must be expected that the nanotubes will have many surface oxides available for protonation. Water consists of H_2O molecules plus positively charge H^+ ions and negatively charge OH^- ions. It is known that a neutral endoperoxide will protonate if a proton is found in the vicinity of either oxygen atom[26]. The effect is reversible and the endoperoxide can deprotonate again as a result of interaction with an OH^- ion upon increasing the pH. Thus, for uncoated SWNTs dispersed in water, a dynamic equilibrium should exist consisting of the continual protonation and deprotonation of the surface oxides. It was found that just a few ($\leq$10) protonated surface oxides is sufficient to quench the luminescence in a nanotube with a length of 400 nm[26].

One possible mechanism for the restoration of NIR-PL by DNA-wrapping would be that the protons in the vicinity of the DNA-nanotube hybrid tend to interact with the negatively charged phosphate on the DNA backbone, rather than protonating the endoperoxide on the nanotube walls. Thus, when the SWNTs are fully coated with DNA, the endoperoxides are generally deprotonated and the NIR-PL is largely

restored. Consequently, a full monolayer coating of DNA could produce the same effect as increasing the pH of the sample. A more likely possibility is that the surface oxides are displaced from the nanotube walls by some competitive binding mechanism as the DNA progressively covers the nanotube. NIR-PL is restored when the DNA-wrapping is complete and all surface oxides have been removed and trapped by the DNA. The activation energy for the desorption of oxygen was calculated to be ~1 eV[26]. This process would be enhanced in solutions stored at higher temperatures[9]. This would explain the greater PL intensities and the presence of larger diameter emission peaks in the 35 °C sample. Aggregation occurred in the 45 °C and 55 °C samples which would explain the reduction in PL intensities from these samples. As previously mentioned, it was found that the nanotube emission in young samples varied as a result of irradiation with an intense light. This phenomenon could be explained by the photodesorption of surface oxides from the nanotube by the intense light source.

In order to investigate the effect of pH on our DNA-SWNT solutions, three samples were prepared at a concentration of 0.04 mg/mL and then diluted 2-fold with 20 mM phosphate buffers to give three 10mM buffered solutions with concentrations of 0.02 mg/mL and pH of 7, 8 and 8.8 respectively. The PL emission was monitored over the following two weeks. The PL emission on day 0 is shown in Figure 6-18 (A). The photoluminescence was found to grow with increasing pH. The pH 8.8 samples displayed intense emission peaks on day 0, while the pH 7 sample exhibited no detectable photoluminescence at that time. The peak heights of the 1044 nm and 1146 nm peaks are shown as a function of time in Figure 6-18 (B). It was found that the NIR-PL from the pH 7 and pH 8 samples grew steadily over the following two weeks until the PL intensity was almost equal to that of the pH 8.8 sample. Thus, although the PL emission is restored by increasing the pH of the sample, the same effect is observed over time. Interestingly, it was found that the NIR-PL intensities grew much faster in the pH7 sample, than in other samples that are dispersed in water without any buffer. It is possible that this is facilitated by interactions between the buffer and the phosphate groups in the DNA backbone.

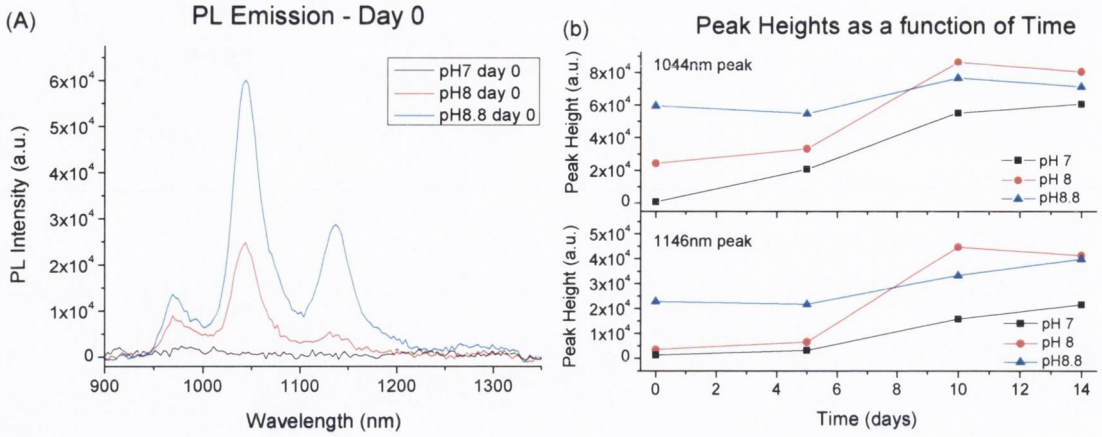


Figure 6-18 (A) PL line spectra, exciting at 655 nm, from three different buffered DNA-SWNT solutions with a pH of 7, 8 and 8.8 respectively. (B) PL peak heights for each sample as a function of time.

Further investigation into the effect of oxygen on the optical properties of the system was carried out. A 6 month old solution with well-defined absorption and PL spectra was split in two. N_2 gas was bubbled through half the sample for 5 min to remove the dissolved oxygen. The other half of the sample was left unmodified. Both samples were then sonicated for five minutes in the sonic bath. The NIR-PL spectra, taken before and after sonication, are shown in Figure 6-19 (A). It was found that the deoxygenated sample had partially retained its NIR-PL emission, while the photoluminescence was completely quenched in the oxygenated sample. A similar effect was observed for the absorption spectrum of the samples. The deoxygenated sample retained its original absorption spectrum, while the oxygenated sample became bleached after sonication (Figure 6-19 (C)). Both samples were stored under nitrogen and the analysed over the following month. The NIR-PL peak heights are shown in Figure 6-19 (B). It was found that both samples regained their original PL intensities over time. However, the oxygenated sample took 35 days before NIR-PL emission was observed again. This is similar to the time taken for the NIR-PL to switch on after initial sample preparation.

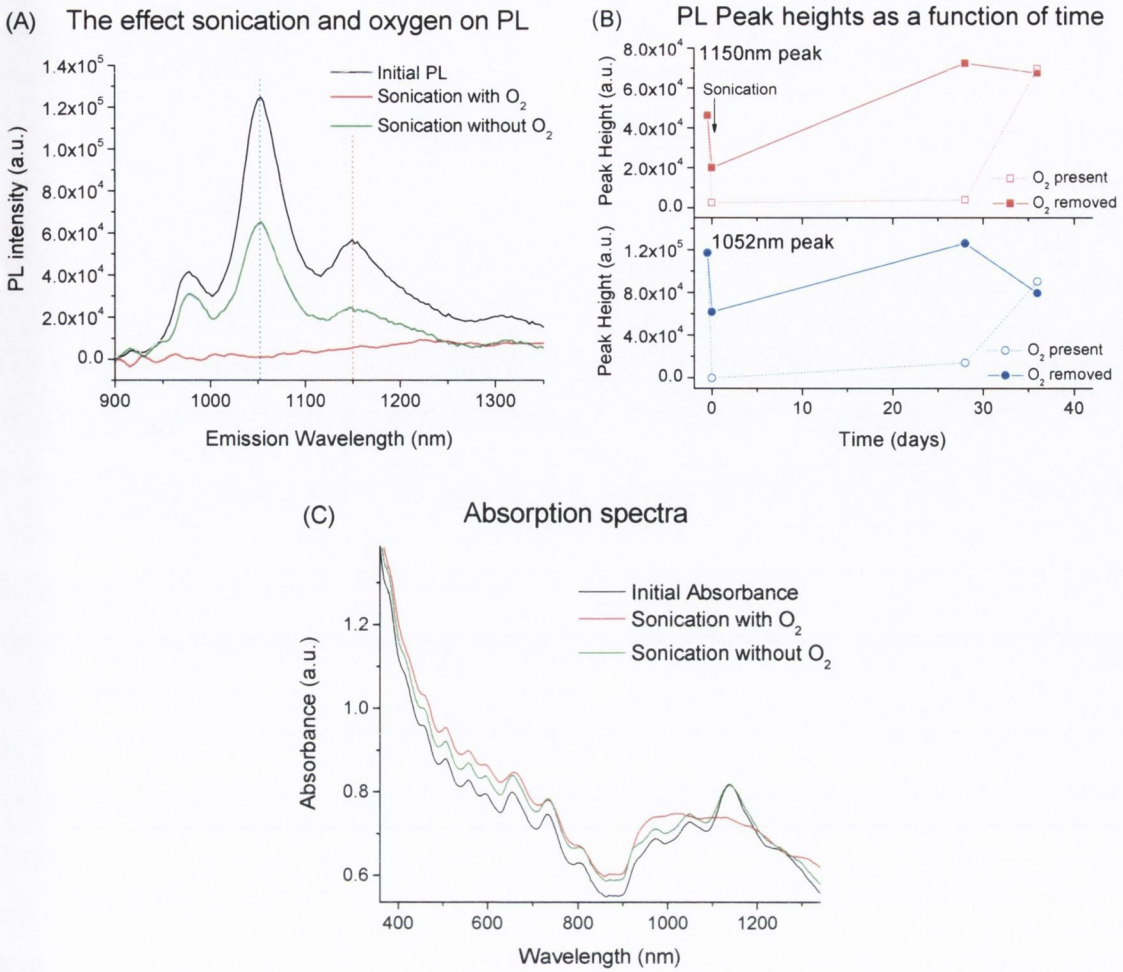


Figure 6-19 (A) NIR-PL line spectra, exciting at 655 nm, for the original sample plus the oxygenated and deoxygenated samples after sonication (B) NIR-PL peaks heights as a function of time for the oxygenated and deoxygenated samples. (C) Absorption spectra for the original sample plus the oxygenated and deoxygenated samples after sonication.

Further analysis of this experiment will be carried out in the future and depends on gaining an understanding of the effects of sonication on the DNA-SWNT hybrid. At present, it is thought that sonication, at least partially, removes the DNA from the nanotube. If this is correct, then it must be assumed that this occurs in both samples. The deoxygenated sample retains its PL spectrum because there is no oxygen available to interact with the SWNT. By this logic, we must assume that there were no surface oxides on the DNA-wrapped nanotube before sonication. Logically, this leads to the

conclusion that the DNA-wrapping facilitates the restoration of NIR-PL emission by the removal of surface oxides from the SWNT, rather than by shielding the nanotube from water or preventing protonation of the surface oxides.

6-3 Conclusion

In conclusion, we have shown that DNA progressively wraps around SWNTs over time. Circular dichroism spectroscopy was utilised to observe the free DNA in solution. The intensity of the CD signal was found to reduce over time as the amount of free DNA in solution decreased as a result of DNA wrapping. HRTEM images showed that DNA wraps helically around the SWNT as suggested in literature. A significant improvement in the NIR-PL and absorption spectra was found to coincide with the completion of a full monolayer coating of DNA on the nanotube. The time taken for the monolayer to form is controlled by some rate limiting process with an activation energy of 0.43 eV. The underlying mechanism for the improvement in the optical properties of the system as a result of DNA wrapping is not yet fully understood. However, it is suggested that the DNA wrapping may facilitate the restoration of the NIR-PL and absorption spectra by the removal of surface oxides from the nanotube sidewalls. Further analysis will need to be carried out before this process is fully understood.

6-4 References

(1) O'Connell, M. J.; Bachilo, S. H.; Huffman, C. B.; Moore, V. C.; Strano, M. S.; Haroz, E. H.; Rialon, K. L.; Boul, P. J.; Noon, W. H.; Kittrell, C.; Ma, J.; Hauge, R. H.; Weisman, R. B.; Smalley, R. E. *Science* **2002**, *297*, 593.

(2) Ryabenko, A. G.; Dorofeeva, T. V.; Zvereva, G. I. *Carbon* **2004**, *42*, 1523.

(3) Landi, B. J.; Ruf, H. J.; Worman, J. J.; Raffaelle, R. P. *Journal of Physical Chemistry B* **2004**, *108*, 17089.

(4) Bachilo, S. M.; Strano, M. S.; Kittrell, C.; Hauge, R. H.; Smalley, R. E.; Weisman, R. B. *Science* **2002**, *298*, 2361.

(5) Tan, Y.; Resasco, D. E. *Journal of Physical Chemistry B* **2005**, *109*, 14454.

(6) Weisman, R. B.; Bachilo, S. M.; Tsyboulski, D. *Applied Physics A (Materials Science Processing)* **2004**, *A78*, 1111.

(7) Hartschuh, A.; Pedrosa, H. N.; Novotny, L.; Krauss, T. D. *Science* **2003**, *301*, 1354.

(8) Cathcart, H.; Quinn, S.; Nicolosi, V.; Kelly, J. M.; Blau, W. J.; Coleman, J. N. *J. Phys. Chem. C* **2007**, *111*, 66.

(9) Nish, A.; Nicholas, R. J. *Physical Chemistry Chemical Physics* **2006**, *8*, 3547.

(10) Heller, D. A.; Jeng, E. S.; Tsun-Kwan, Y.; Martinez, B. M.; Moll, A. E.; Gastala, J. B.; Strano, M. S. *Science* **2006**, *311*, 508.

(11) Choi, J. H.; Strano, M. S. *Applied Physics Letters* **2007**, *90*, 223114.

(12) Strano, M. S.; Huffman, C. B.; Moore, V. C.; O'Connell, M. J.; Haroz, E. H.; Hubbard, J.; Miller, M.; Rialon, K.; Kittrell, C.; Ramesh, S.; Hauge, R. H.; Smalley, R. E. *Journal of Physical Chemistry B* **2003**, *107*, 6979.

(13) Strano, M. S.; Moore, V. C.; Miller, M. K.; Allen, M. J.; Haroz, E. H.; Kittrell, C.; Hauge, R. H.; Smalley, R. E. *Journal of Nanoscience and Nanotechnology* **2003**, *3*, 81.

(14) Heller, D. A.; Baik, S.; Eurell, T. E.; Strano, M. S. *Advanced Materials* **2005**, *17*, 2793.

(15) Hertel, T.; Hagen, A.; Talalaev, V.; Arnold, K.; Hennrich, F.; Kappes, M.; Rosenthal, S.; McBride, J.; Ulbricht, H.; Flahaut, E. *Nano Letters* **2005**, *5*, 511.

(16) Chou, S. G.; Ribeiro, H. B.; Barros, E. B.; Santos, A. P.; Nezich, D.; Samsonidze, G. G.; Fantini, C.; Pimenta, M. A.; Jorio, A.; Filho, F. P.; Dresselhaus, M. S.; Dresselhaus, G.; Saito, R.; Zheng, M.; Onoa, G. B.; Semke, E. D.; Swan, A. K.; Unlu, M. S.; Goldberg, B. B. *Chemical Physics Letters* **2004**, *397*, 296.

(17) Bloomfield, V. A.; Crothers, D. M.; Tinoco, I. *Nucleic Acids: Structures, Properties and Functions*; University Science Books: California, 2000.

(18) Zheng, M.; Jagota, A.; Semke, E. D.; Diner, B. A.; McLean, R. S.; Lustig, S. R.; Richardson, R. E.; Tassi, N. G. *Nature Materials* **2003**, *2*, 338.

(19) Warshaw, M. M.; Cantor, C. R. *Biopolymers* **1970**, *9*, 1079.

(20) Rajendra, J.; Baxendale, M.; Rap, L. G. D.; Rodger, A. *Journal of the American Chemical Society* **2004**, *126*, 11182.

(21) Lustig, S. R.; Jagota, A.; Khripin, C.; Zheng, M. *Journal of Physical Chemistry B* **2005**, *109*, 2559.

(22) Zheng, M.; Jagota, A.; Strano, M. S.; Santos, A. P.; Barone, P.; Chou, S. G.; Diner, B. A.; Dresselhaus, M. S.; McLean, R. S.; Onoa, G. B.; Samsonidze, G. G.; Semke, E. D.; Usrey, M.; Walls, D. J. *Science* **2003**, *302*, 1545.
(23) Gigliotti, B.; Sakizzie, B.; Bethune, D. S.; Shelby, R. M.; Cha, J. N. *Nano Lett.* **2006**, *6*, 159.
(24) Porschke, D.; Eigen, M. *Journal of Molecular Biology* **1971**, *62*, 361.
(25) Wall, A.; Ferreira, M. S. *J. Phys. :Condens Matter* **2007**, *19*, 406227.
(26) Dukovic, G.; White, B. E.; Zhou, Z.; Wang, F.; Jockusch, S.; Steigerwald, M. L.; Heinz, T. F.; Friesner, R. A.; Turro, N. J.; Brus, L. E. *Journal of the American Chemical Society* **2004**, *126*, 15269.

Chapter 7

The dispersion efficiency of oligonucleotides

7-1 Introduction

The aim of this study was to investigate the dispersion efficiency of a number of short, single-stranded oligonucleotides and to clarify the relationship between nanotube concentration and bundle size for each dispersant. It has been shown that short oligonucleotides are effective at dispersing SWNTs in water[1,2]. In fact oligonucleotides are regarded by many as the dispersant of choice for processing SWNTs[3,4]. However, to date, most research on oligonucleotide dispersions has relied on using ultra-centrifugation to remove the nanotube bundles, providing solutions that are rich in individually dispersed nanotubes[1,3,5,6]. Removing this processing step significantly reduces waste and consequently lower preparation costs. It has previously been shown that, for DNA-SWNT solutions prepared with natural salmon testes DNA, the distribution of bundle sizes is dependent on the nanotube concentration, and thus, by reducing the concentration of the sample, one can push the bundle diameters towards lower values, removing the need for ultra-centrifugation[7]. In this work, we aim show that a similar relationship exists between bundle diameter and nanotube concentration for solutions prepared with short, custom-synthesised oligonucleotides. In addition, we hope gain a greater understanding of the effects of different nucleotide bases on the nanotube absorption and NIR-PL spectra.

7-2 Experimental Procedure

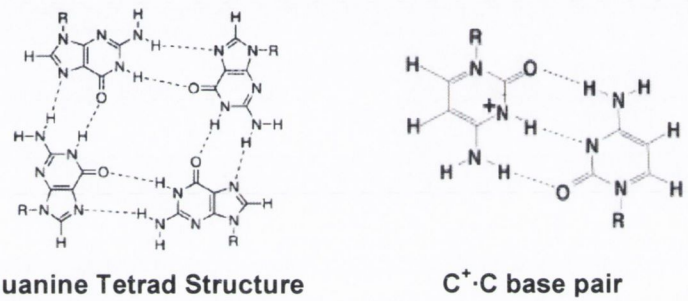
DNA-SWNT stock solutions were prepared using four different oligonucleotides[8] — dA_{15}; dT_{15}; dC_{15} and dG_{15}. For comparison, a fifth stock solution was prepared using poly(rA)[9], a medium length, single-stranded RNA homopolymer, containing adenine as the only nucleotide base.

Each solution was prepared with a concentration of 0.1 mg/mL and a ratio of 5:1 (oligo:SWNT). Initially, ratios of 2:1 (oligo:SWNT) were used, however, excessive levels of nanotube precipitation were observed to occur overnight in these samples and it was decided that larger quantities of DNA were necessary when dispersing nanotubes with oligonucleotides. The solutions were prepared as described in section 4-10. Briefly, the solutions were each sonicated for two hours, before centrifuging at 3,300g for one hour. A full set of serial dilutions, with concentrations ranging from the post-centrifuge stock concentration down to 0.001 mg/mL, were prepared from each stock solution. Each dilution was sonicated for 30 min before preparing the next serial dilution. The samples were analysed using AFM, NIR-PL and absorption spectroscopy, allowing one to make quantitative and qualitative measurements on the dispersion efficiency of each DNA type.

7-3 Results

The concentration of each stock solution after centrifugation was ascertained by comparing the absorption spectra recorded before and after centrifugation. Centrifugation removes the large nanotube bundles from the stock solution, leaving only smaller bundles and individually dispersed SWNTs. Thus, solutions with larger populations of individual SWNTs and small bundles will have higher concentrations after centrifugation, and so the post-centrifuge concentration can be used as a measure of the dispersion efficiency of each DNA type. The concentrations of the stock solutions after centrifugation were found to be 0.073 mg/mL for dT_{15} sample; 0.069 mg/mL for dC_{15} sample; 0.06 mg/mL for dA_{15} sample; 0.059 mg/mL for the poly(rA) sample; and 0.047 mg/mL for the dG_{15} sample. Thus, in agreement with theoretical

predictions[10], it was found that the oligonucleotides containing pyrimidine bases were more efficient at dispersing SWNTs than those containing purine bases, leading to a greater mass of SWNTs remaining in solution after centrifugation. The observation that purine and pyrimidine bases have different stabilising effects is very interesting. However, it is worth noting that this study does not explore the possible role of base:base interactions at the nanotube surface. For instance, it is known that both cytosine-rich and guanine-rich DNA can form non Watson-Crick hydrogen bonding motifs. In the case of guanine these can be in the form of extended chains or tetrad structures[11] based on Hoogsteen binding, while for cytosine, protonation can result in the formation of $C^{+}{\cdot}C$ base pairing through three hydrogen bonds as shown in Figure 6-1.



Guanine Tetrad Structure **$C^{+}{\cdot}C$ base pair**

Figure 6-1 Non Watson-Crick hydrogen bonding motifs for guanine and cytosine

It should be noted that the post-centrifuge concentrations for the poly(rA) and the dA_{15} samples are very similar, suggesting that dispersion efficiency of DNA is more critically dependent on the type of nucleotide bases used, rather than on the length of the DNA.

7-2-1 AFM

AFM images of each sample were recorded in order to measure the bundle diameter distributions for each dilution series*. Unfortunately, in many of the oligonucleotides samples, a dense network of DNA covered much of the mica substrate (Figure 7-2 (left)), preventing one from accurately measuring the bundle diameters. Consequently, although we were able to measure sufficient numbers of

nanotube bundles to obtain diameter distributions for the dG_{15} dilution series, we were unable to acquire enough data to give dependable statistics for the other three oligonucleotide dilution series. It is thought that the observed DNA network only forms when large amounts of very short DNA are used. Visually, the images obtained from the poly(rA) samples were of much better quality and were not covered with excess nucleic acid.

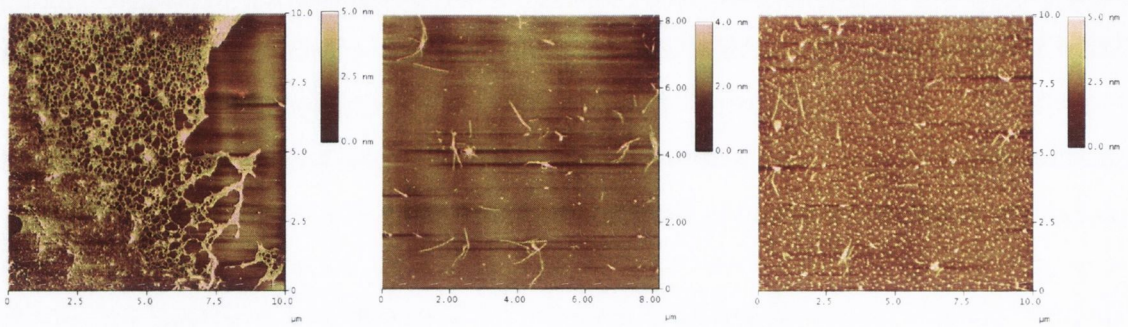


Figure 7-2 AFM images showing: (Left) DNA network observed on many of the oligonucleotide samples (Centre) poly(rA) sample, 0.001 mg/mL (Right) dG_{15} sample, 0.001 mg/mL

AFM images of the 0.001 mg/mL poly(rA) and the dG_{15} samples are shown in Figure 7-2 (centre) and (right) respectively. Both images clearly show nanotubes, however large quantities of very short DNA are adsorbed onto the mica surface in the dG_{15} sample, making the background appear very uneven. Histograms of the bundle diameters are shown in Figure 7-3. In both series it is clear that both the bundle diameters and the distribution width decrease as the concentration is reduced. In addition, a significant population of small bundles and individual SWNTs was observed at all concentrations. It should be noted that even in the most concentrated samples, the range of bundle diameters is extremely small. In the most concentrated dG_{15} solution, the maximum bundle diameter is just 12 nm, while in poly(rA) sample, the maximum observed diameter is just 14 nm. Thus, it must be concluded that both poly(rA) and dG_{15} are extremely efficient at dispersing SWNTs, even at reasonably high concentrations.

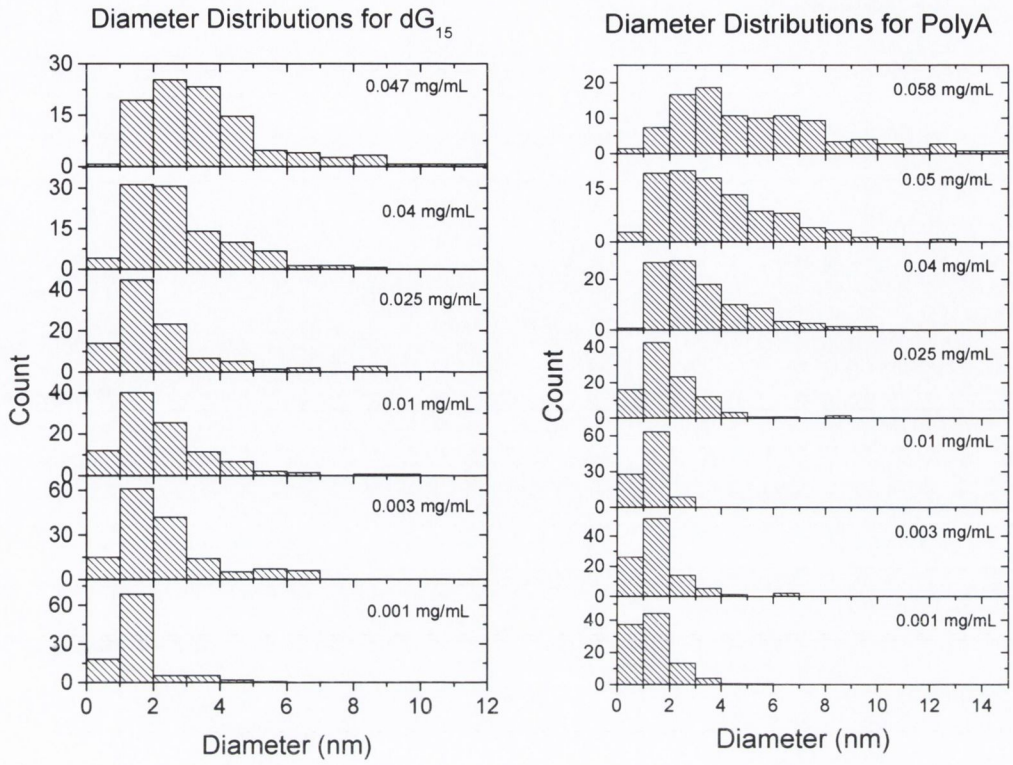


Figure 7-3 Histograms of bundle diameters for all concentrations in the dG_{15} (left) and poly(rA) (right) dilution series.

Both the mean diameters (D_{mean}) and root-mean-squared diameters (D_{rms}) are shown as a function of concentration in the upper panels of Figure 7-4. D_{rms} is more sensitive to the larger bundles in the dispersion. In the dG_{15} dilution series, the mean diameter decreased linearly with concentration, before stabilising at an average minimum value of 2.3 nm (D_{rms} = 2.7 nm) for concentrations of 0.025 mg/mL and below. Similarly, in the poly(rA) dilution series, the mean diameters decreased linearly with concentration, before settling at an average minimum value of just 1.5 nm (D_{rms}=1.65 nm) for concentrations of 0.01 mg/mL and below. It is thought that the difference in mean diameters at low concentrations is the result of differences in the degree of DNA wrapping, rather than because of a greater level of debundling in the poly(rA) samples. The oligonucleotides are extremely short and are expected to cover the walls of the SWNT very quickly. Thus, the measured nanotube diameters should include a contribution from the DNA. However, poly(rA) is much longer, with average

lengths of between 465 and 660 bases, and so wrapping occurs over a greater timescale, giving bundle diameter distributions that are characteristic of unwrapped SWNTs in the early stages of the experiment.

The number fractions of individual SWNTs (N_i/N_t) have been calculated for two separate cut-off values and are shown in the lower panels of Figure 7-4. HiPCO SWNTs have diameters ranging from 0.7 nm to 1.4 nm. Consequently, a cut-off value of $N_i \leq 1.4$ nm gives the fraction of individual nanotubes for uncoated SWNTs, as found in the poly(rA) samples, while a cut-off value of $N_i \leq 2.4$ nm gives approximate number fractions for wrapped nanotubes, allowing for a 1 nm covering of DNA on the walls of the SWNT, as found in the dG_{15} dilution series. In the poly(rA) dilution series, we obtained mean number fractions of 0.63 for concentrations of ≤0.01 mg/mL, while in the dG_{15} dilution series, N_i/N_t was found to stabilise at a mean value of 0.76 when the DNA coating was accounted for. It should be noted that in the dG_{15} samples, number fractions of 0.32 were obtained for cut-off values of 1.4 nm, showing that individual SWNTs are still present in solution, even if the timescale for DNA wrapping is greater than expected and the SWNTs are uncoated at this time.

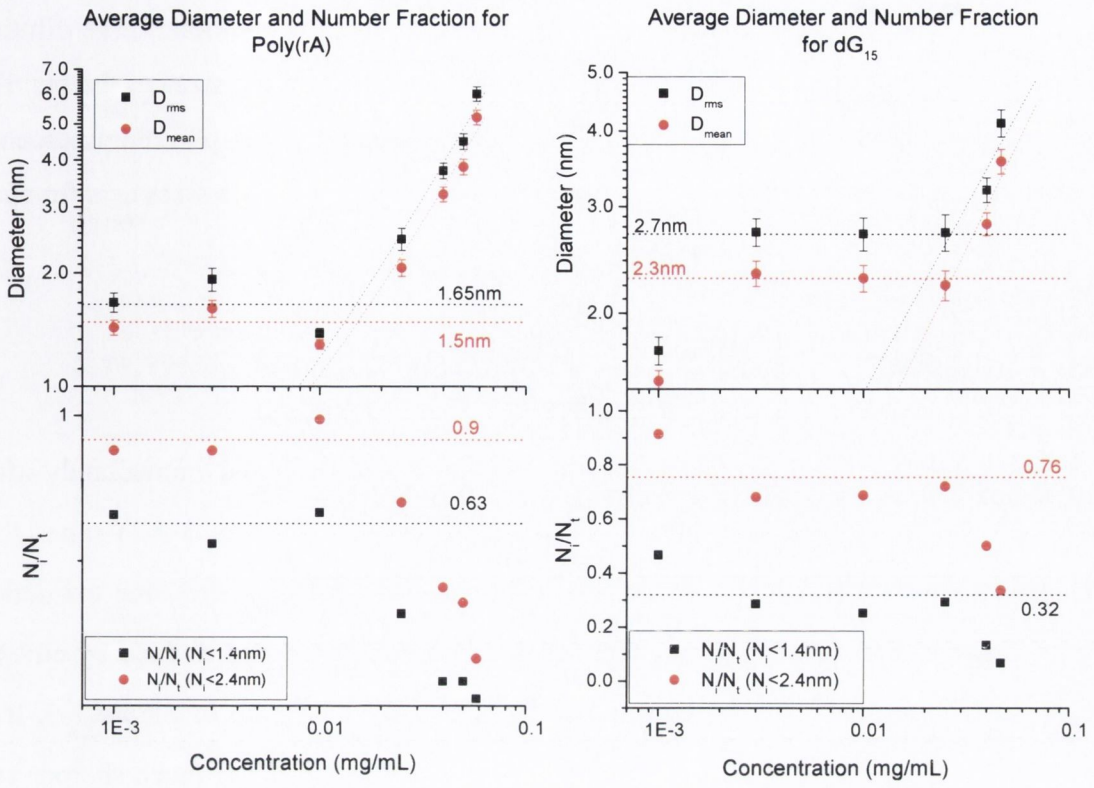


Figure 7-4 (Above) The mean nanotube diameters are plotted as function of concentration, showing them to decrease linearly before stabilising at a minimum diameters of 1.5 nm and 2.3 nm in the poly(rA) and dG_{15} samples respectively. (Below) The number fractions are calculated for cut-off values of 1.4 nm & 2.4 nm.

In conclusion, it was found that both dG_{15} and poly(rA) are efficient at debundling SWNTs in aqueous solutions. The concentration of nanotubes remaining in solution after centrifugation was found to be smaller for dG_{15} and poly(rA) than for the pyrimidine-based dispersions. However, once the nanotubes were dispersed in solution, both dG_{15} and poly(rA) were found to be efficient at debundling the nanotubes, producing dispersions with very small bundle diameters and narrow distribution widths. The mean diameters in the dG_{15} dilution series are slightly greater at lower concentrations than for the poly(rA) dispersions as a result of DNA wrapping. However, when the contribution of the DNA coating was taken into consideration, it was found that the number fraction of individual SWNTs was actually slightly greater in the dG_{15} dilution series.

Unfortunately, in the absence of reliable AFM data for the other three dilution series, an alternative method of analysis must be found to infer the sizes of the bundles in solution. To this end, both absorbance spectroscopy and NIR-photoluminescence spectroscopy have been employed to monitor changes in the bundle sizes as a function of concentration for all dilution series.

7-2-2 Absorption and NIR-PL Spectroscopy

The absorption spectra of each dilution series was recorded immediately after sample preparation and analysed. The Lambert-Beer Law (Section 3-2-1) states that the absorbance (A) is equal to the product of the concentration (C), the extinction coefficient (ε) and the cuvette pathlength (l). Thus, the absorbance divided by cuvette pathlength (εC) for each sample is shown in the left-hand column of Figure 7-5. It is immediately obvious that the dilution series prepared with dC_{15} has much sharper van Hove absorption peaks at all wavelengths and at all concentrations than the other four solutions. S_{22} and M_{11} absorption peaks can be seen in all solutions, however only the solutions prepared with dC_{15} exhibit clear S_{11} transitions. The extinction coefficient (ε) is shown as a function of wavelength in the right-hand column of Figure 7-5. The van Hove peak extinction coefficients were observed to increase upon dilution in all five dilution series. This phenomenon has previously been reported and indicates debundling in the solution[2, 12]. The increase in extinction coefficient was observed for all transitions, but is most remarkable for the S_{11} transition peaks. This phenomenon was not observed previously in samples prepared with natural DNA.

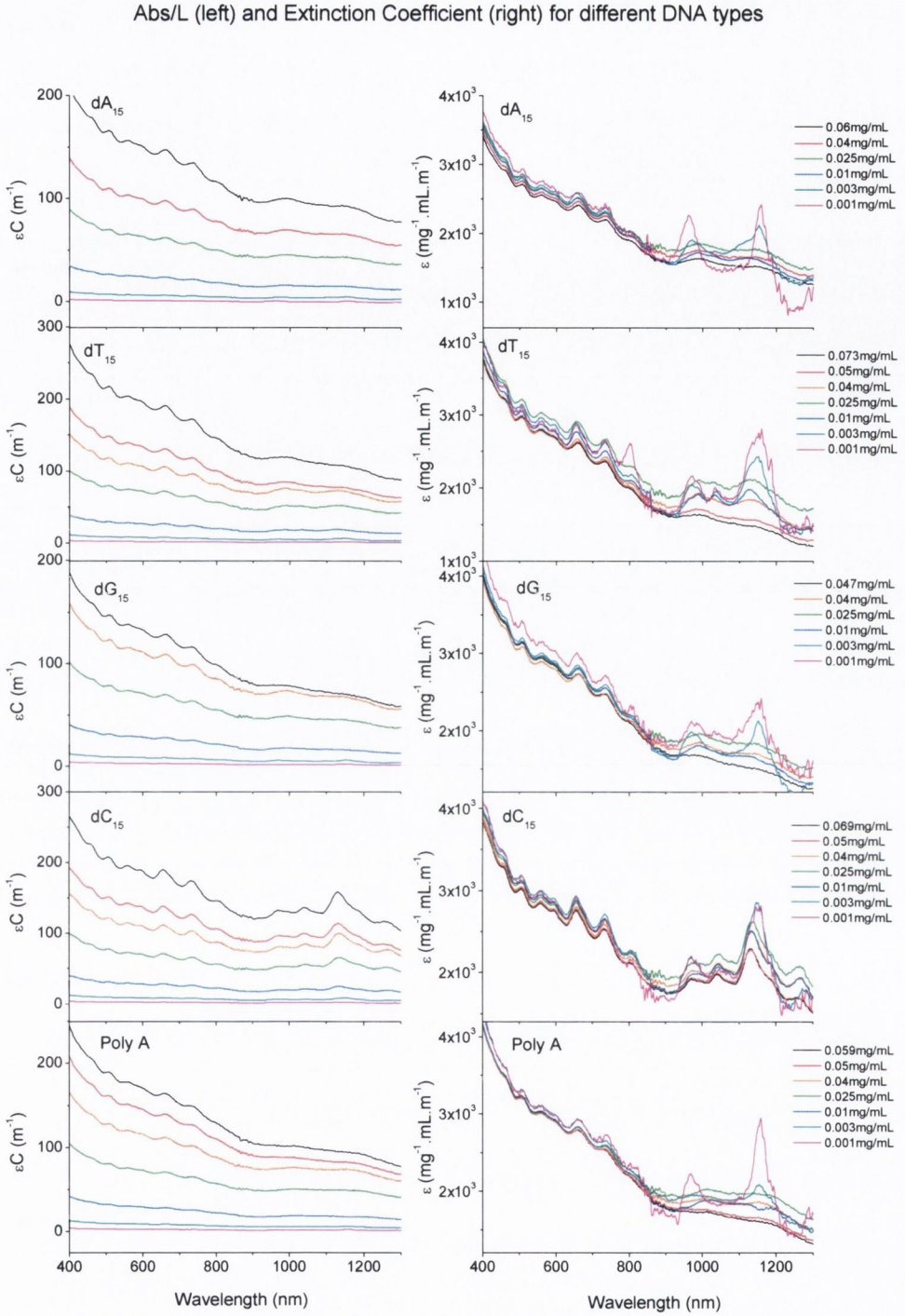


Figure 7-5 (Left) Absorbance divided by cuvette pathlength (εC) for each dilution series. It is clear that the dC_{15} dilution series has significantly sharper van Hove peaks. (Right) Extinction coefficient as a function of wavelength for each dilution series. The van Hove peaks were observed to sharpen upon dilution.

The absorbance divided by pathlength (εC) for the four 0.04 mg/mL oligonucleotide solutions are shown together in Figure 7-6 as a function of wavelength, allowing a clear comparison between the different samples. It was found that the magnitude of the background absorption is similar in all samples, but that the size of the van Hove peaks varies significantly between samples. Again, differences between the pyrimidine-based and purine-based solutions were observed. It was found that the samples prepared with pyrimidine-based DNAs, particularly dC_{15}, had the larger van Hove peaks, especially in the S_{11} region. Close inspection revealed that the van Hove peaks in the samples prepared with pyrimidine bases were blue shifted with respect to those prepared with purine bases by up to 12 nm for the S_{11} peaks and between 4–7 nm for the S_{22} peaks. Shifts in the van Hove peak positions have been reported elsewhere[13-15] and have been attributed differences in the dielectric properties in the environment of the nanotubes. In addition, it is suggested that interaction between the nanotube and the surrounding water plays a key role in the effective dielectric potential seen by the excitons[13] and so differences in the type of DNA used, the degree of wrapping and hence, the shielding of the nanotube from the surrounding water would cause changes in the PL and absorbance peak positions. This effect could be enhanced by non Watson-Crick bonding between bases, which would lead to different degrees of shielding from the surrounding water.

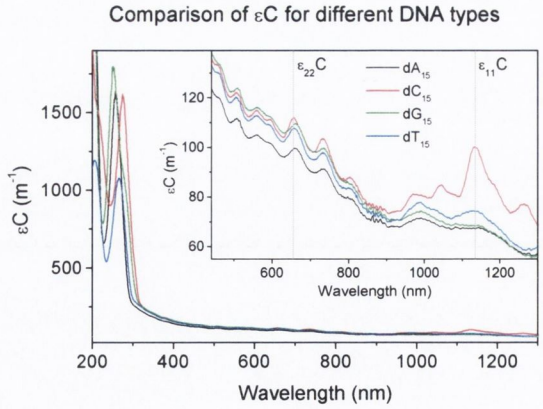


Figure 7-6 Comparing of εC spectra for the four oligonucleotide 0.04 mg/mL solutions.

NIR-PL spectra were recorded immediately after sample preparation using a 2mm × 2mm fluorescence cuvette. As expected, no emission was observed from the poly(rA) samples at this time. It is thought that longer wrapping times, resulting in quenching effects similar to those mentioned in chapter six, are responsible for the lack of NIR-PL in these samples. The NIR-PL spectra from the oligonucleotide samples are shown in Figure 7-7. The upper panels show the spectra from the purine-based dilution series (dA_{15} and dG_{15}), while the lower panels show the spectra from the pyrimidine-based dilution series (dT_{15} and dC_{15}). It should be noted that the intensity scale is 10 times greater for pyrimidine-based dispersions than for the purine-based dispersions. Interestingly, the NIR-PL spectral profile differed considerably between the purine-based and pyrimidine-based dispersions. The samples prepared with dC_{15} and dT_{15} exhibited strong, well-defined PL spectra similar to those observed previously for samples prepared with natural DNA. The emission from the dC_{15} samples is slightly stronger than for the dT_{15} samples. In both dilution series, the NIR-PL emission increased with increasing nanotube concentration, indicating that the absolute number of individual semiconducting SWNTs grows as the concentration increases. The spectral shape is reasonably concentration independent, indicating that the relative populations of individual nanotube types do not change significantly as the overall concentration is changed.

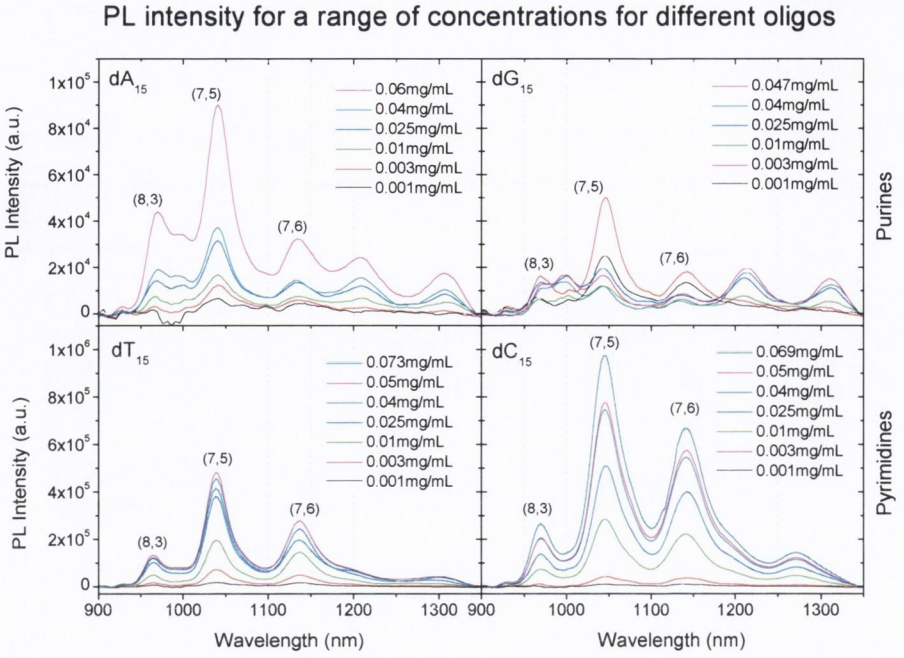


Figure 7-7 PL spectra for all four oligonucleotide dilution series. The purine-based dilution series are shown in the top panels and the pyrimidine based dilution series are shown in the bottom panels. It should be noted that the scale on the bottom graphs is 10× greater than that of the top graphs

The PL emission from the dG_{15} and dA_{15} dilution series was much weaker with a different spectral shape. Two weak peaks were observed at wavelengths of ~1208 nm and ~1310 nm. These peaks do not coincide with any known SWNT emission peaks and are thought to originate from the broadened, red shifted emission from small bundles containing only semiconducting SWNTs. It should be noted that these peaks are also present in the dC_{15} and dT_{15} spectra (Figure 7-8 (A)), but are masked by the other, more intense PL peaks. The PL emission increases with increasing concentration in the dA_{15} dilution series. However, in the dG_{15} dilution series, PL is only observed for the two lowest concentrations as shown by the red and black traces in the top right-hand panel of Figure 7-7. In fact at low concentrations, the PL emission from the dG_{15} sample is similar to that observed for the dT_{15} and dC_{15} solutions as shown in Figure 7-8 (B). The reason for the absence of photoluminescence at higher concentrations is not yet fully understood. AFM analysis confirms that a population of individual SWNTs is present in solution at all concentrations. Thus, one possibility is that dG_{15} preferentially debundles metallic nanotubes, and so at higher concentrations, the observed individual

nanotubes are mostly metallic and do not fluoresce. Individual semiconducting SWNTs are only present at lower concentrations where extensive debundling has occurred. Equally it is possible that another quenching mechanism is at work. The NIR-PL from the dG_{15} dilution series was observed to grow very slightly over time, suggesting that a process similar to that expounded in chapter 6 is the basis of the PL quenching in this sample.

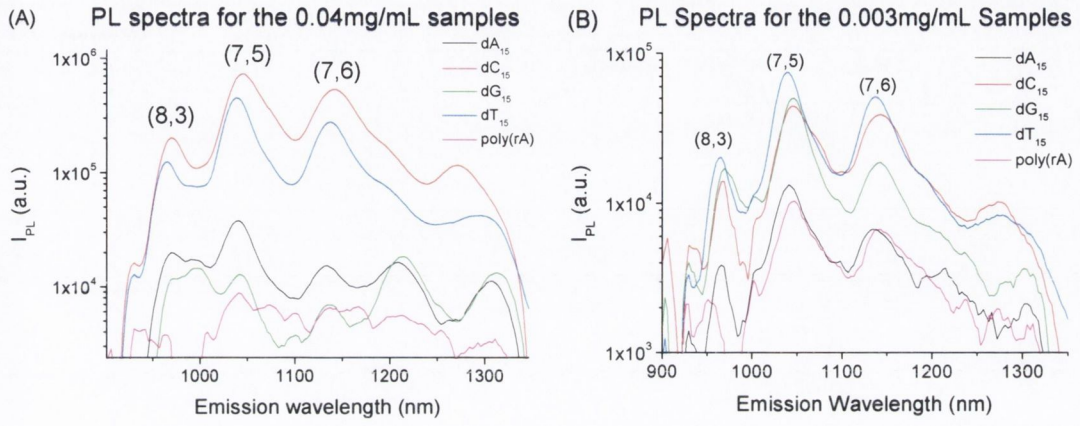


Figure 7-8 (A) PL spectra for all five 0.04 mg/mL samples, clearly showing the difference in magnitude of the purine-based and pyrimidine based solutions. (B) PL spectra for 0.003 mg/mL samples. At this concentration PL emission is observed for all DNA types, however the emission from the dA_{15} and the poly(rA) is extremely weak.

In order to compare the shape and magnitude of the PL spectra, five samples are presented together in Figure 7-8 (A) & (B) at concentrations of 0.04 mg/mL and 0.003 mg/mL respectively. At the higher concentration, the difference in the emission intensity from the five samples is unmistakable, clearly showing the spectra from the dC_{15} and dT_{15} samples to be superior (Figure 7-8 (A)) At the lower concentration, the differences are less pronounced (Figure 7-8 (B)). Weak emission is observed from the dA_{15} and poly(rA) samples, while the PL intensity of the dG_{15} sample is similar to that of the purine-based samples. It should be noted that the PL peaks both red and blue shift slightly, both as the concentration changes and for different dispersants. Table 7-1 shows the peak positions for the main nanotube peaks for all dispersants at two concentrations — 0.04 mg/mL and 0.003 mg/mL. The origin of these peak shifts is not yet fully understood. As mentioned above, the optical transition energies of SWNTs

are influenced by the dielectric properties of their local surroundings[13,15], and thus, the type of DNA used, the degree of wrapping and the level of interaction between the nanotube and the surrounding water are all expected to cause changes in the PL peak positions.

(n,m)	Position									
	dA_{15}		dT_{15}		dG_{15}		dC_{15}		Poly(rA)	
	0.04 mg/mL	0.003 mg/mL	0.04 mg/mL	0.003 mg/mL	0.04 mg/mL	0.003 mg/mL	0.04 mg/mL	0.003 mg/mL	0.04 mg/mL	0.003 mg/mL
(8,3)	969 nm	965 nm	965 nm	964 nm	971 nm	969 nm	970 nm	966 nm	No peaks observed	952 nm
(7,5)	1039 nm	1041 nm	1039 nm	1039 nm	1041 nm	1045 nm	1044 nm	1045 nm		1046 nm
(7,6)	1133 nm	1134 nm	1137 nm	1136 nm	1136 nm	1142 nm	1142 nm	1142 nm		1141 nm

Table 7-1 The main peak positions for all dispersants at concentrations of 0.04mg/mL and 0.003mg/mL.

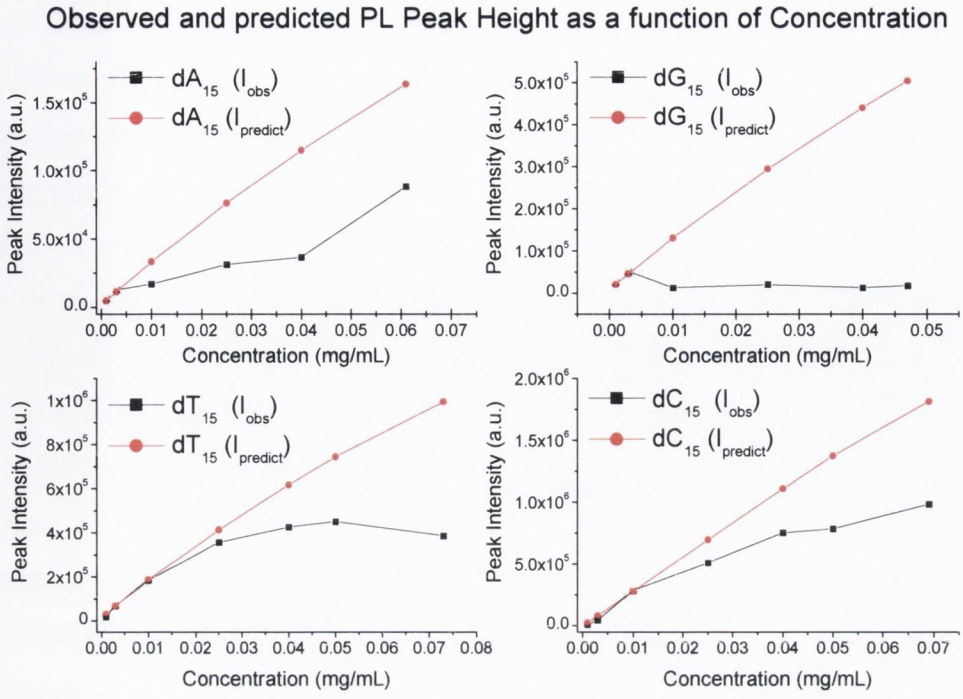


Figure 7-9 The peak heights for the (7,5) peak are shown in black for each oligonucleotide dilution series. Shown in red, are the maximum predicted peak intensities, calculated to account for attenuation of the PL emission due to inner-filter and re-absorption effects. This is the peak heights that are predicted to be observed in the absence of quenching due to nanotube bundling.

We have assumed that, at a given time, the degree of DNA coverage is constant within each dilution series. This is based on the fact that changes in the DNA wrapping occur slowly over time and so are unlikely to affect these samples. Consequently any changes in the NIR-PL emission over the concentration range are indicative of changes in the population of individual semiconducting SWNTs, rather than the result of time-dependent changes in the DNA coating. The heights of the (7,5) emission peaks were measured and are shown as a function of concentration in Figure 7-9. Also shown, is the maximum predicted emission intensity ($I_{predict}$), calculated to allow for a reduction in PL intensity as a result of inner-filter and re-absorption effects[16]. Thus, $I_{predict}$ shows the PL intensity that would be observed if no aggregation occurred in the solution. It should be noted that both re-absorption and inner-filter effects have been minimised by using a 2mm×2mm cuvette, and so, the predicted emission intensities scales almost

linearly with concentration. Consequently, the sub-linearity in the observed PL intensities (I_{obs}) cannot be attributed to re-absorption and inner-filter effects. We therefore suggest that the reduction in intensity must be the result of the progressive formation of nanotube bundles due to the increase in nanotube concentration. When nanotube bundles form, the PL intensity reduces as a result of two separate effects — firstly, the van Hove absorption peaks reduce in intensity[12,17,18] and secondly, the quantum efficiency decreases. When a photon of light is absorbed, an exciton is created in the nanotube. In semiconducting nanotubes, the exciton decays non-radiatively to the lowest energy level and then recombines, emitting a photon with energy equal to that of the band gap. However, bundle formation causes the extinction coefficient to reduce, as seen in Figure 7-5, and so fewer photons are absorbed, creating fewer excitons and consequently reducing the PL emission. Additionally, when bundles form, the excitons that are created can be quenched by non-radiative decay through the metallic nanotubes in the bundles, further reducing the PL emission. Thus, bundle formation also reduces the quantum efficiency of the system.

These two effects are plotted separately in Figure 7-10. Graphs (A) and (B) show the extinction coefficient (ε) of the van Hove absorption peak as a function of concentration for the 655 nm (ε_{22}) and the 1137 nm (ε_{11}) peaks respectively. The extinction coefficients for the absorption peaks are calculated by subtracting the background scattering from each absorption peak (as shown in Figure 4-7) and then dividing by the product of the nanotube concentration and cuvette length. In all solutions, the extinction coefficients were found to increase as the concentration decreased, indicating progressive debundling in all four dilution series. The quantum efficiency of the system is a measure of number of photons that are absorbed and then re-emitted as fluorescence, rather than decaying non-radiatively. Thus, Figure 7-10 (C) shows the fraction of emitted light as a function of the absorbed light, which is related to the quantum efficiency of our DNA-SWNT systems. It shows that the quantum efficiency of the system increases as the concentration decreases as a result of debundling in the solution. Thus, both absorption and NIR-PL spectroscopy show progressive changes in the nanotube spectra that indicate extensive debundling of nanotube bundles as a direct result of decreasing nanotube concentration.

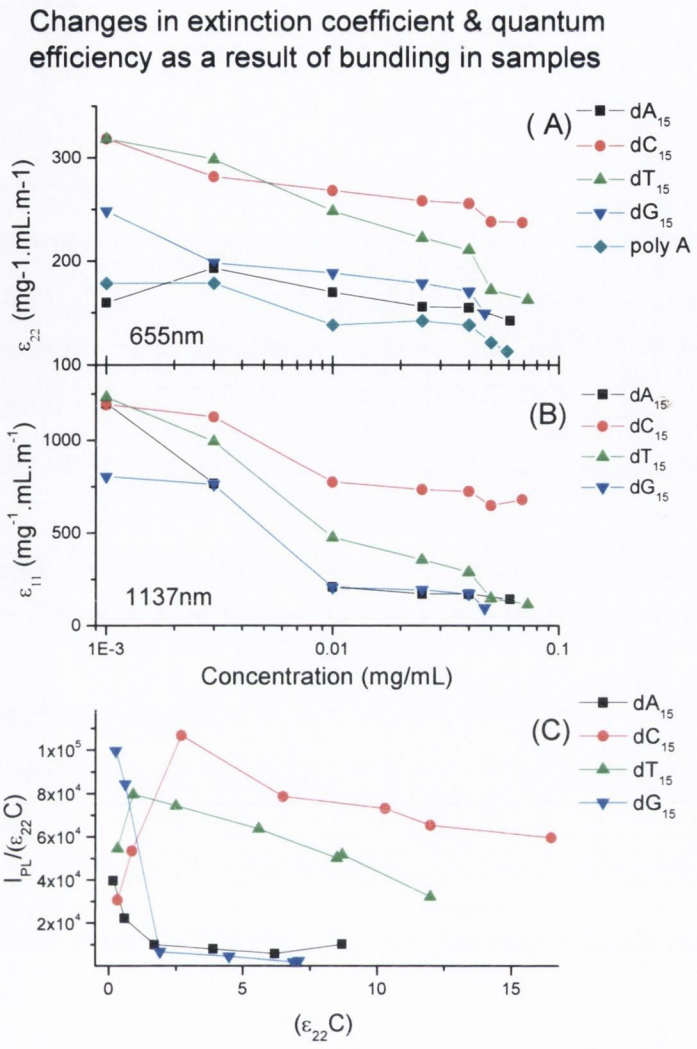


Figure 7-10 (A) & (B) The extinction coefficients of the 655 nm and 1137 nm absorption peaks is shown as a function of concentration respectively. The extinction coefficients increase with decreasing concentration as a result of debundling in the solution. (C) The fraction of emitted light is shown as a function of the absorbed light, showing the quantum efficiency to increase as the concentration decreases as a result of debundling in the solutions.

7-2-3 Time dependent changes in the photoluminescence

Interestingly, it was found that the NIR-PL emission from the oligonucleotide solutions changes with time. Figure 7-11 (left) shows the (7,5) peak height as a function of time for the 0.04 mg/mL samples. No PL emission was observed from the poly(rA) over the 20 day duration of the experiment. The emission from the dA_{15} samples was observed to grow with time, while the emission from the dC_{15} and the dT_{15} samples reduced over time, such that the emission observed from all three samples on day 20 was of similar magnitude. The PL emission from the dG_{15} samples was observed to grow for the first 17 days, before reducing again on day 20, as shown by the dark blue trace in Figure 7-11 (left). The PL spectra from day 20 are shown in Figure 7-11 (right). These effects will be further investigated in future experiments.

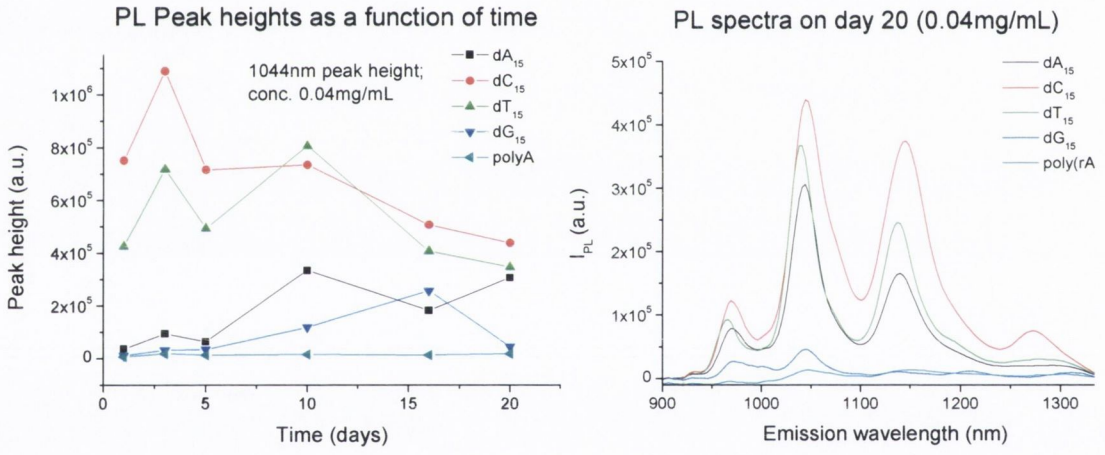


Figure 7-11 (left) Peak heights for the (7,5) peak as a function of time for the 0.04m/mL samples. The dC_{15} and dT_{15} samples were found to initially increase in height and subsequently decrease in height, while the dA_{15} and dG_{15} samples grew with time. (right) PL spectra for the 0.04 mg/mL samples on day 20, showing the dC_{15}, dT_{15} and dA_{15} samples to be similar in spectral shape and magnitude, while the dG_{15} and poly(rA) samples are vary weak at this time.

7-3 Conclusion

In conclusion, SWNTs were dispersed in water using short oligonucleotides and medium-length, single-stranded RNA. We found that, in agreement with literature[10], the pyrimidine bases are more effective at dispersing SWNTs than purine bases. In addition, interactions with different nucleotide bases were observed to have a significant effect on the optical properties of the system.

The nanotube bundle sizes in all five dilution series were found to be dependent on concentration. AFM images were used to attain quantitative data on the bundle diameter distributions for samples prepared with dG_{15} and poly(rA). It was found that the bundle diameters decreased with concentration, stabilising at mean diameters of ~1.5 nm and ~2.3 nm and number fractions of 0.63 and 0.76 at low concentrations for the poly(rA) and dG_{15} dilution series respectively. It is likely that a similar trend would be observed for the other oligonucleotides-SWNT dispersions. Absorption and NIR-PL spectroscopy were employed for the qualitative analysis of the nanotube bundle sizes in all four oligonucleotide solutions. It was found that reducing the nanotube concentration caused both the extinction coefficient and the quantum efficiency of the solutions to increase. Both effects indicate the progressive debundling of nanotubes.

It was observed that the shape and magnitude of both the absorption and PL spectra is dependent on the type of DNA used. Specifically, samples prepared with dC_{15} exhibited well-defined van Hove absorption peaks, and samples prepared with pyrimidine-based DNA displayed strong, well-defined PL spectra. The differences in the magnitudes of the PL spectra were found to reduce over the following 17 days as a result of a decrease in the PL intensity from the dC_{15} and dT_{15} samples, accompanied by an increase in the PL intensity from the dA_{15} and dG_{15} samples. The PL emission from the dG_{15} samples was then observed to reduce again.

7-4 References

1. Zheng, M. et al. DNA-assisted dispersion and separation of carbon nanotubes Nature Materials 2, 338-342 (2003).
2. Arnold, M. S., Stupp, S. I. & Hersam, M. C. Enrichment of single-walled carbon nanotubes by diameter in density gradients Nano Lett. 5, 713-718 (2005).
3. Zheng, M. et al. Structure-based carbon nanotube sorting by sequence-dependent DNA assembly Science 302, 1545-8 (2003).
4. Onoa, B., Zheng, M., Dresselhaus, M. S. & Diner, B. A. Carbon nanotubes and nucleic acids: Tools and targets. Physica Status Solidi (A) Applied Research 203, 1124-1131 (2006).
5. Strano, M. S. et al. Understanding the nature of the DNA-assisted separation of single-walled carbon nanotubes using fluorescence and Raman spectroscopy Nano Letters 4, 543-50 (2004).
6. Chou, S. G. et al. Optical characterization of DNA-wrapped carbon nanotube hybrids Chemical Physics Letters 397, 296-301 (2004).
7. Cathcart, H. et al. Spontaneous Debundling of Single-Walled Carbon Nanotubes in DNA-Based Dispersions. J. Phys. Chem. C 111, 66-74 (2007).
8. Oligonucleotides were all purchased from Sigma Genosys.
9. PolyA, purchased from Amersham Bioscience. Product number: 27-4110-01. Average length 465-660 bases
10. Enyashin, A. N., Gemming, S. & Seifert, G. DNA-wrapped carbon nanotubes. Nanotechnology 18, 245702 (2007).
11. Jin, R. Z., Breslauer, K. J., Jones, R. A. & Gaffney, B. L. Tetraplex formation of a guanine-containing nonameric DNA fragment. Science 250, 543-546 (1990).
12. O'Connell, M. J. et al. Band gap fluorescence from individual single-walled carbon nanotubes Science 297, 593-596 (2002).
13. Hertel, T. et al. Spectroscopy of single- and double-wall carbon nanotubes in different environments. Nano Letters 5, 511-14 (2005).
14. Moore, V. C. et al. Individually Suspended Single-Walled Carbon Nanotubes in Various Surfactants Nano Lett. 3, 1379-1382 (2003).
15. Choi, J. H. & Strano, M. S. Solvatochromism in single-walled carbon nanotubes. Applied Physics Letters 90, 223114 (2007).
16. Rickard, D., Giordani, S., Blau, W. J. & Coleman, J. N. Quantifying the contributions of inner-filter, re-absorption and aggregation effects in the photoluminescence of high-concentration conjugated polymer solutions. Journal of Luminescence In Press, Corrected Proof.
17. Landi, B. J., Ruf, H. J., Worman, J. J. & Raffaelle, R. P. Effects of alkyl amide solvents on the dispersion of single-wall carbon nanotubes Journal of Physical Chemistry B 108, 17089-95 (2004).
18. Tan, Y. & Resasco, D. E. Dispersion of single-walled carbon nanotubes of narrow diameter distribution. Journal of Physical Chemistry B 109, 14454-14460 (2005).

Chapter 8

Conclusions and Further Work

8-1 Conclusions

The aim of this thesis was to investigate the nature of the interaction between DNA and single walled carbon nanotubes and to explore the factors controlling the dispersion efficiency of DNA. To this end, a variety of experiments were performed with a range of different nucleic acids. A systematic study on the optimisation of sample preparation was completed, allowing one to consistently prepare high quality DNA-SWNT dispersions. A full concentration study was then carried out in order to examine the dispersion properties of natural double-stranded DNA and to clarify the relationship between nanotube concentration and bundle size. SWNTs were dispersed in water with salmon testes DNA with a range of nanotube concentrations. AFM images of the samples were recorded to measure the bundle diameters within each sample, allowing one to calculate statistics on the bundle diameter distributions. It was found that the bundle sizes within a sample are critically dependent on nanotube concentration rather than on sonication parameters and the mean bundle diameters tended to decrease as the concentration was reduced. The partial concentration of individual SWNTs was found to be maximised in dispersions with a nanotube concentration of ~0.027 mg/mL. Number fractions of up to 0.83 individual SWNTs, equating to partial concentrations of up to 6.2% were obtained at low concentrations. These values clearly show that dilution could be used as a viable, cost-effective alternative to ultra-centrifugation.

In addition, it was shown that spontaneous debundling occurs when the nanotube concentration is reduced. This suggests that DNA-SWNT hybrids exist in water as a solution rather than as a dispersion. This is a very surprising result as it implies that it is thermodynamically favourable for debundling to occur when the nanotube concentration is reduced. Thus, in young solutions, the DNA must be arranged on the walls of the nanotube in such a way as to disperse the nanotubes in the surrounding water, while still allowing debundling to occur. Therefore the DNA cannot be tightly wrapped around the nanotubes at this stage.

In order to further investigate the nature of the interaction between DNA and SWNTs, a sample was prepared with natural salmon testes DNA and monitored over a 3 month period. It was found that the DNA progressively wraps around SWNTs over time. At first the DNA is loosely associated with the nanotube, slowly wrapping around the nanotube over time to form a thick DNA coating. HRTEM images show that in samples stored at room temperature, it takes between 35 and 49 days for a full monolayer of DNA to cover the walls of the nanotube. In addition, HRTEM images showed helical DNA wrapping around the SWNT at this time, as proposed in literature[1-4]. It was suggested that the double-stranded DNA unzips onto the nanotube walls, mimicking its actions in nature. This allows the two individual strands to interact separately with the nanotube. The strands were observed to phase shift by 180° with respect to each other, thus maximising both the nanotube coverage and the distance between the negatively charged phosphates on the backbone of each strand. A significant improvement in the NIR-PL and absorption spectra was found to coincide with the completion of a monolayer of DNA coverage. A sizeable increase in the height of the van Hove absorption peaks was observed, coinciding with the appearance of a set of intense PL emission peaks. Circular dichroism spectroscopy was utilised to monitor the quantity of free DNA in solution. The intensity of the CD signal was found to reduce continuously over time, tracking the progression from a solution dominated by free DNA to one dominated by bound DNA.

The dependence of the rate of wrapping was investigated with respect to the sample temperature. It was found that the time taken for the monolayer to form is dependent on the sample temperature and is controlled by some rate limiting process

with an activation energy of 0.43 eV. This activation energy is in keeping with the wrapping mechanism suggested above. The underlying mechanism for the improvement in the nanotubes' optical properties upon the completion of DNA wrapping is not yet fully understood. At present, it is suggested that the DNA wrapping may facilitate the restoration of the NIR-PL and absorption spectra by the removal of surface oxides from the nanotube sidewalls. Further analysis will be carried out in the future.

Finally, the dispersion efficiency of a number of different nucleic acids was investigated. A number of short homo-oligonucleotides and a medium-length, single-stranded RNA were studied as dispersants. Initial studies showed that pyrimidine bases are more effective than purine bases at dispersing SWNTs. In addition, interactions with different nucleotide bases were observed to have a significant effect on both the absorption and the PL spectra. It was found that the shape and magnitude of both the absorption and PL spectra were dependent on the type of DNA used. Specifically, samples prepared with dC_{15} exhibited well-defined van Hove absorption peaks, while samples prepared with pyrimidine-based DNA displayed a strong, well-defined PL spectra.

In all five dilution series, the nanotube bundle sizes were shown to be dependent on the nanotube concentration. AFM images were obtained for two dilution series, namely those prepared with dG_{15} and poly(rA). Statistics on the bundle diameter distributions were calculated, showing that bundle diameters to decrease with decreasing nanotube concentration, stabilising at mean diameters of ~1.5 nm and ~2.3 nm and number fractions of 0.63 and 0.76 at low concentrations for the poly(rA) and dG_{15} dilution series respectively. Absorption and NIR-PL spectra were recorded for all four oligonucleotide solutions. It was found that both the extinction coefficient and the quantum efficiency of the solutions increased as the nanotube concentration reduced, indicating the progressive debundling of nanotubes. No luminescence was observed from the poly(rA) samples. Thus it was shown both quantitatively and qualitatively that debundling occurs in all solutions as the nanotube concentration decreases.

In conclusion, the main discoveries of this thesis were that the bundle diameter distribution of DNA-dispersed SWNTs is dependent on the nanotube concentration.

Debundling was found to occur spontaneously when the nanotube concentration was reduced for all types of DNA studied. It was found that DNA progressively wraps around the nanotube over time forming a complete monolayer between days 35 and 49 in samples kept at room temperature. A large increase in the magnitude of the van Hove absorption peaks and the PL emission peaks was observed at this time. In addition, HRTEM images clearly showed DNA wrapping of SWNTs at this time.

8-2 Future Work

There is much future work still to be carried out on DNA-SWNT dispersions. Initially, we will concentrate on investigating the interactions between DNA and SWNTs in order to fully ascertain the mechanism of PL quenching in young solutions. At present, it is thought that oxygen on the walls of the SWNT causes quenching of the PL and absorption spectra[5-7]. It is suggested that as the DNA wraps around the SWNT, it removes this oxygen from the nanotube sidewalls and traps it, thus restoring the PL and absorbance spectra upon the completion of DNA wrapping. It was found that when these older solutions were sonicated, the luminescence disappeared again. However, when the oxygen was removed from the solution prior to sonication, the luminescence remained. We plan to investigate the effects of sonication on older DNA-SWNT samples using HRTEM in order to verify that sonication removes the DNA from the walls of the nanotube. If this is correct, it reinforces the suggestion that the restoration of photoluminescence by DNA-wrapping is facilitated by the removal of oxygen from the SWNT, rather than by shielding the nanotube from water or preventing protonation of the surface oxides as discussed in Section 6-2-6. In addition, HRTEM imaging will be carried out on solutions that are held at higher temperatures to ensure that the rate of DNA coverage does increase at higher temperatures.

In young samples, where DNA wrapping is incomplete, it was found that irradiating the solutions with an intense light source partially restored photoluminescence. These changes were found to be reversible, and had disappeared 16 hrs later. We suggest that the light removes oxygen from the walls of the nanotube by photodesorption. The oxygen left in solution then re-adsorbs onto the walls of the

SWNT over time, and quenches the luminescence again. We plan to carry out a more rigorous study on this effect. We plan to irradiate the solutions with a strong light to photodesorb the oxygen and restore luminescence and then perform a time study to determine the kinetics of oxygen re-adsorption in DNA-SWNT solutions. In addition, we hope to remove the excess oxygen from a second solution immediately after irradiation, in order to determine whether or not the PL remains constant over time when there is no oxygen present in the sample.

In order to investigate the ability of DNA to remove oxygen from aromatic carbon rings, we plan to dissolve 1,4-dimethylnaphthalene-1,4-endoperoxide (DMN-O2), which is a standard source of singlet oxygen [8], with salmon testes DNA in water. It is suggested that the DNA will remove the endoperoxide from the dimethylnapthalene and trap it. The fluorescence of the dimethylnapthalene is quenched by the presence of the endoperoxide, thus, by removing the endoperoxide, the photoluminescence is restored. Time-resolved photoluminescence measurements will be carried out in order to monitor the quantities of singlet oxygen and dimethylnapthalene in solution in order to ascertain whether the DNA removes and traps the oxygen from the aromatic carbon rings.

Further studies will be carried out on the spontaneous debundling of nanotubes in order to ascertain the timescales over which debundling occurs. The study in Chapter 5 showed that, while debundling occurred in the absence of sonication, the bundle diameters were smaller in those samples that had been sonicated. We will investigate whether similar diameter distributions are achieved in unsonicated samples when left to equilibrate over time. This will be investigated with a variety of DNA types.

We plan to repeat the nanotube concentration study using oligonucleotides, with the aim of obtaining high-quality AFM images for all dispersants. This would enable us to calculate statistical data on the bundle diameter distributions as a function of concentration for each dilution series, allowing a direct comparison of the dispersion properties of different DNA types. To this end, we will investigate a range of different DNA:SWNT ratios with the aim of preparing stable dispersions, while minimising the excess DNA in the AFM images. During this study we plan to further

study the effects of different nucleotide bases on the absorption and PL spectra of the DNA-SWNT samples, with the aim of increasing our understanding of the interactions between DNA and nucleic acids.

Additionally, we plan to investigate the effect DNA length on the bundle diameter distributions and dispersion quality of the solutions. Initial studies suggest that while the length of the DNA is not critical to its dispersion efficiency of the DNA, it has a significant effect on the rate of DNA wrapping and hence on the optical properties of the system. Thus, samples will be prepared with a range of nucleotides with different lengths, and analysed using absorption spectroscopy, photoluminescence spectroscopy and AFM.

Further research into the toxicological effects of SWNTs will be carried out in conjunction with the School of Pharmacy and Pharmaceutical Sciences in Trinity College Dublin. SWNTs have many properties which make them very attractive for use within medical diagnostic and biological fields[9, 10]. However, while much research is being carried out in order to exploit the desirable properties of SWNTs, it is imperative that we also evaluate and reduce any potential undesirable effects of nanotubes. To this end, we aim to evaluate the effects of introducing both individual SWNTs and bundles of nanotubes into the blood stream. It has previously been shown that MWNTs and SWNTs induce platelet aggregation and accelerate the rate of vascular thrombosis in the carotid arteries of rats[11,12]. We plan to carry out further study in order to evaluate the effects of both DNA-dispersed nanotube bundles and individual SWNTs on platelet aggregation.

Finally, we plan to carry out an extensive study on a range of different dispersants such as surfactants, amide solvents, peptides and nucleic acids. AFM analysis, in conjunction with NIR-PL spectroscopy and absorption spectroscopy will be used to compare the dispersion efficiency of these dispersants, such that in future, one can make an informed choice and the pros and cons of using different dispersants.

8-3 References

1. Gigliotti, B., Sakizzie, B., Bethune, D. S., Shelby, R. M. & Cha, J. N. Sequence-Independent Helical Wrapping of Single-Walled Carbon Nanotubes by Long Genomic DNA Nano Lett. 6, 159-164 (2006).
2. Lustig, S. R., Jagota, A., Khripin, C. & Zheng, M. Theory of structure-based carbon nanotube separations by Ion-exchange chromatography of DNA/CNT hybrids Journal of Physical Chemistry B 109, 2559-2566 (2005).
3. Zheng, M. et al. DNA-assisted dispersion and separation of carbon nanotubes Nature Materials 2, 338-342 (2003).
4. Zheng, M. et al. Structure-based carbon nanotube sorting by sequence-dependent DNA assembly Science 302, 1545-8 (2003).
5. Dukovic, G. et al. Reversible surface oxidation and efficient luminescence quenching in semiconductor single-wall carbon nanotubes. Journal of the American Chemical Society 126, 15269-15276 (2004).
6. Nish, A. & Nicholas, R. J. Temperature induced restoration of fluorescence from oxidised single-walled carbon nanotubes in aqueous sodium dodecylsulfate solution. Physical Chemistry Chemical Physics 8, 3547-51 (2006).
7. Strano, M. S. et al. Reversible, band-gap-selective protonation of single-walled carbon nanotubes in solution. Journal of Physical Chemistry B 107, 6979-6985 (2003).
8. Gunther S, G., Lemp M, E. & Zanocco, A. L. Determination of chemical rate constants in singlet molecular oxygen reactions by using 1,4-dimethylnaphthalene endoperoxide. Journal of Photochemistry and Photobiology A: Chemistry 151, 1-5 (2002).
9. Heller, D. A., Baik, S., Eurell, T. E. & Strano, M. S. Single-walled carbon nanotube spectroscopy in live cells: Towards long-term labels and optical sensors. Advanced Materials 17, 2793-2799 (2005).
10. Karachevtsev, V. A., Glamazda, A. Y., Leontiev, V. S., Lytvyn, O. S. & Dettlaff-Weglikowska, U. Glucose sensing based on NIR fluorescence of DNA-wrapped single-walled carbon nanotubes. Chemical Physics Letters 435, 104-108 (2007).
11. Medina, C., Santos-Martinez, M., Radomski, A., Corrigan, O. & Radomski, M. REVIEW: Nanoparticles: pharmacological and toxicological significance. British Journal of Pharmacology 150, 552-558 (2007).
12. Radomski, A. et al. Nanoparticle-induced platelet aggregation and vascular thrombosis. Br J Pharmacol 146, 882-893 (2005).

Appendix: Publication List

- **Cathcart H.,** Quinn S., Nicolosi V., Kelly J. M., Blau W. J., and Coleman J. N., *"Spontaneous Debundling of Single-Walled Carbon Nanotubes in DNA-Based Dispersions"*, J. Phys. Chem. C., **2007,** Vol. 111, Page 66

- Nicolosi V., **Cathcart H.**, Dalton A. B., Ahern D., Kelly J. M., Dieckmann G. R. and Coleman J. N. *"Spontaneous Exfoliation of Single Walled Carbon Nanotubes Dispersed Using a Designed Amphiphilic Peptide"*, Biomacromolecules, **2008**, Vol 9, Page 598

- Bergin S.D., Nicolosi V., **Cathcart H.**, Lotya M., Rickard D., Sun Z., Blau W.J., Coleman J.N. *"Large populations of individual SWNT in surfactant based dispersions without the need for ultracentrifugation"*. Phys. Chem. C., **2008**, Vol 112, Page 972

- **Cathcart H.,** Nicolosi V., Hughes M, Quinn S., Kelly J. M., Blau W. J., and Coleman J. N., *"DNA-wrapping switches on luminescence in SWNT dispersions"*, Submitted.